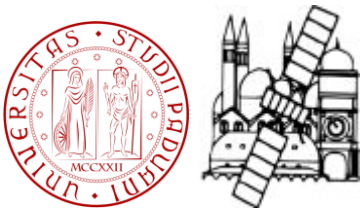

UNIVERSITÁ DEGLI STUDI DI PADOVA

CISAS "G. Colombo"

(Center of Studies and Activities for Space)

Ph.D. School STMS

Science Technologies and Measures for Space

Curriculum: Mechanical Measures for Engineering and Space (MMIS)

Ph.D. Thesis

Analysis Of Variable Thrust Hybrid Propulsion For Formation Flight Satellites

Head of the Ph.D. School

Prof. Naletto Giampiero

Tutors

Ing. Pavarin Daniele

Ing. De Cecco Mariolino

Ph.D. Student

Bellomo Nicolas

CYCLE XXIV — 2012

Abstract

Hybrid motors are a promising brand of space propulsion. Many benefits have been demonstrated, like the fact that they can be "green", low cost safe. In this optics, with this thesis we want to characterize throttle-able hybrid motor for collision avoidance in formation flight.

The purpose is to enhance the performance of a "state of the art" motor, in particular mitigating the effect of some drawbacks like low regression rate and combustion efficiency. The propellant choice has been pressurized nitrous oxide as oxidizer and paraffin wax as fuel.

The work started with a preliminary design of the motor with a 0-D transient analytical code. Objective was to define the main dimensions like nozzle, grain, combustion chamber and oxidizer mass flow, and to help in the sensors choice for the full scale level.

A 3D steady state CFD analysis have been performed, to have a full comprehension of the phenomenon involving vortex flow field inside the combustion chamber. It has been discovered that the most important parameter is the temperature gradient produced by the combustion process, that increase the axial velocity straightening the fluid lines.

This numerical analysis has been used also to characterize the motor performance, simulating different chamber configurations: a) different grain port diameter, to study the combustion at different burning time, b) variation in oxidizer mass flow, involving throttling effects and c) different combustion chamber configuration, using mixer-like devices and pre/post-combustion chambers.

An analytical tool has been developed, using steady state Navier-Stokes in cylindrical coordinates: results showed a forced vortex behaviour of the velocity profile of the fluid field. Moreover, a pressure gradient in radial direction has been discovered. This knowledge helped in the selection of the correct pick-up point of the pressure in combustion chamber, in a position (near the nozzle) where this effect is negligible.

Throttling device selection has devised the use of a needle valve. The selected model, prior to its use in burning test, has been characterized with water (in a preliminary phase) and nitrous oxide in cold test.

The experimental campaign has taken the majority of this work: first cold test have been performed to evaluate the oxidizer mass flow with both axial and vortex injection, discovering that they have the same discharge coefficient; measured mass flow was 350g/s.

Burning test involved all previous investigated field: studying axial and vortex injection have been discovered that the second technique gives an increase in combustion efficiency from 73% to 91%, and an increase in regression rate of 41% with the a coefficient going from 0.19mm/s in the axial case to 0.31mm/s in the vortex case. Pressure oscillations in combustion chamber were reduced from 7.5% to 3.8%.

Throttling has been performed in two levels: 75% and 50%. In both cases pressure oscillations remained the same, while combustion efficiency dropped to a value of 85% for the first case and 82% for last. Regression rate has not changed appreciably.

Last part regarded combustion chamber configuration: we found out that the use of mixer-like devices enhances the regression rate of 6% and raise the combustion efficiency up to 96%. Use of a longer pre-combustion chamber (from 10mm to 17mm) has similar but lower effect: combustion efficiency has an increment of 3%. In both cases, pressure chamber oscillation drop to a level lower than 2%.

Sommario

I motori ibridi fanno parte di un promettente ramo della propulsione aerospaziale. Sono giá stati dimostrati diversi benefici, quali il fatto che siano "green", a basso costo e con una elevata sicurezza nelle operazioni. In quest'ottica, con questa tesi si vuole caratterizzare un motore ibrido a spinta variabile da utilizzarsi per collision avoidance in formation flight.

Lo scopo é di incrementare un motore giá esistente con le tecnologie allo stato dell'arte, ed in particolare cercare di mitigare gli effetti negativi classici degli ibridi come il basso regression rate ed efficienza di combustione. La scelta dei propellenti é ricaduta su N_2O pressurizzato come ossidante e paraffina come propellente.

La prima fase del progetto ha visto la creazione di un modello transient 0-D analitico per il design preliminare del motore. In particolare, si sono ricavate le dimensioni di grano, ugello e camera di combustione e la portata di massa obiettivo.

Successivamente, é stato analizzato il campo di moto fluido interno alla camera di combustione tramite un codice stazionario 3-D CFD. Il risultato emerso é che il parametro fondamentale per la fluidodinamica interna é il gradiente di temperatura prodotto dalla combustione, che accelera la componente assiale di velocitá raddrizzando le linee fluide.

Questo stesso strumento é stato impiegato anche per caratterizzare in via numerica le configurazioni di motore che sono state poi testate. Tre gruppi di analisi sono state effettuate: a) differente portata di ossidante, per studiare il fenomeno del throttling dal punto di vista fluidodinamico, b) diverso diametro di porta del grano, per studiare il comportamento del motore in diversi istanti temporali e c) differenti configurazioni di camera di combustione, con l'impiego di componenti tipo mixer o pre/post-camere.

Un tool analitico che utilizza le equazioni di Navier-Stokes in coordinate cilindriche é stato sviluppato con lo scopo di aumentare la conoscenza del campo di moto. In particolare, é stato scoperto che il profilo di velocitÃ del flusso segue un vortice forzato, ed é presente un gradiente di pressione in senso radiale. Questa

informazione ha permesso un piú accurato posizionamento dei sensori, in modo da avere un minore effetto gradiente nella misura del segnale di pressione.

Il throttling ha richiesto una selezione di dispositivi regolatori di flusso: la scelta é caduta su una valvola a spillo. Questa é stata caratterizzata dal punto di vista sperimentale mediante test a freddo sia con acqua che con l'ossidante reale utilizzato nei successivi test a fuoco.

La campagna sperimentale é iniziata con dei test a freddo per caratterizzare i due iniettori, assiale e vortex; il risultato é che hanno la stessa portata (350g/s) a paritá di salto di pressione, e quindi lo stesso coefficiente di scarica.

Successivamente sono state studiate le performance con dei burn test: con la metodologia di iniezione vortex si ottengono incrementi sia di regression rate(+41%) che di efficienza di combustione (si passa da 73% a 91%). Le oscillazioni di pressione in camera scendono da un valore sulla media di pressione di 7.5% al 3.8%.

Il throttling é stato studiato in due livelli: 75% e 50% della portata di massa di ossidante. La riduzione di portata é stata accompagnata da una riduzione di efficienza di combustione (85% per il primo caso, 82% per il secondo), mentre le oscillazioni di pressione sono rimaste le stesse.

L'ultima parte ha visto lo studio di diverse configurazioni della camera di combustione. In particolare, si é visto che dispositivi tipo mixer permettono un incremento di efficienza fino al 96%, ed un aumento del regression rate del 6%. Anche l'impiego di pre-camere piú lunghe (da 10mm a 17mm) fornisce prestazioni simili ma con incrementi minori: l'efficienza é innalzata del 3%. In entrambi i casi vi é un effetto positivo nella riduzione delle oscillazioni di pressione, che si attestano ad un valore inferiore al 2%.

Contents

List of Figures

List of Tables

Glossary

cc	Combustion Chamber
$CISAS$	Center for Studies and Activity for Space "G. Colombo", at University of Padua
O/F	oxidizer to fuel mass ratio
$a,\ n$	multiplication and exponential coefficient for regression rate
ρ_f, rho_{ox}	density of fuel-oxidizer
ρ	density
r, θ, z	cylindrical coordinates (radial, tangential and axial)
$u_r\ u_\theta,\ u_z$	radial, tangential and axial velocity
$\phi_i,\ \phi_e,\ \phi_m$	initial, final and mean diameter of the grain
μ	dynamic viscosity
M_f	mass of burned fuel
G_{ox}	mass flux in combustion chamber
L_g	grain length
ω	vortex angular velocity
T	temperature
t	time
M_m	molar mass
R_u	Universal gas constant
p,p_c	pressure, mean chamber pressure
A_t	nozzle throat area
$\dot{m}_f, \dot{m}_{ox}$	mean fuel-oxidizer mass flow
η_c	combustion efficiency
S	Swirl number
S_g	Geometrical swirl number

Chapter 1

Introduction

1.1 Formation Flight

Satellite Formation Flight by definition is a cooperation between two ore more satellites to achieve a global objective. Instead of flying one monolithic satellite that is in charge to perform every operation, many tasks can be divided between single or groups of usually smaller ones.

There are many advantages [22]:

- concurrent design: many sub-systems design strategy can be shared (e.g. thermal control, attitude...);
- lower cost: design is shared in many parts between satellites, as much as manufacturing an off-the-shelves parts;
- redundancy: a mission can be accomplished, eventually with an objective reduction, also if some of the satellites suffer of performance degradation; the others can cover the missing functions;
- reconfiguration: many different missions can be accomplished.

A particular point that must be respected is that the dynamic states must be coupled through a common law [27].

Depending on the application, there are three formations possible:

- trailing;
- cluster;
- constellation.

Trailing formations are groups of satellites placed in a same path. The distance between each other can produce many interesting features, like changing the viewing angle of the same scene at the same time, or viewing the same place at different time steps. These are intensively used for meteorology and Earth Science studies (formation - diffusion of clouds, fire detection). An example of this kind of mission is the Terra and Aqua (and many more) satellites, being part of the EOS (Earth Observing System) NASA program [5].

Figure 1.1: Formation flight example

Other examples can contain the LISA (Laser Interferometer Space Antenna) ESA-NASA mission [9], where three satellites are placed in the *L1* lagrangian point of Earth-Sun system at fixed distance between each other. The purpose is to detect gravitational wave effects by measuring relative distance of three reference masses.

Cluster satellites, instead, operate in a tight formation, and usually relative distance are close. Main uses are Space or Earth observation and interferometry, developing bigger telescopes in which every satellite is a a small part. An example is the Tandem-X formation flight mission [23].

The main difference between cluster and trailing formation flight mission is the control law that links the satellites, that usually must be more robust and strict in terms of accuracy.

In all cases, attitude control requires an authority of very low ΔV, in the order of 10^{-1} and lower, depending on the mass of the satellites [25], resulting in thrust levels of maximum 1N.

1.2 Hybrid motors

A hybrid motor, by definition, is a chemical propulsive system that combine fuel and oxidizer in a different state [4]; the most common is liquid or gaseous

oxidizer and solid fuel.

With this kind of propulsion, it has already been demonstrated that there could be a strong killing in cost, due to the simple subsystems needed and green propellants that avoid difficult procedures to test the engines. More over, hybrid propulsion permits better performances than liquid, maintaining safety, reliability and re-ignition capability: the oxidizer flux can be stopped in every moment just with a valve.

The main advantages for a hybrid propulsion system are:

- cost
- reliability
- throttability
- re-ignition

Hybrid rockets can be divided in 4 main parts (see fig.1.2):

- an oxidizer tank (can be pressurized or not);
- an injection system, composed by a valve (on/off or regulated, depending on the application) that permits the oxidizer to enter in the combustion chamber and an injection plate, that diffuse the oxidizer towards the grain;
- a combustion chamber, usually composed by the fuel itself; it can have different shapes (hollow cylinder, wagon wheel...);
- nozzle section, common to all propulsive systems.

The choice of the propellant is pressurized N_2O as oxidizer, and paraffin wax as fuel. This selection of materials permits to reduce the cost of the tests because it's a green and safe propellant combination. One of the main reasons is the reduced safety measures respect to other oxidisers as H_2O_2.

Although nitrous oxide is a low energetic oxidizer, it has a number of advantageous features:

- it is safe to handle, thus it permits safe and low-cost extensive ground-tests;
- it allows for high regression rate, enabling a compact and simple grain design;
- it's a not an energetic material, therefore it requires small safety issues and allows for low-cost manufacturing, handling and testing;

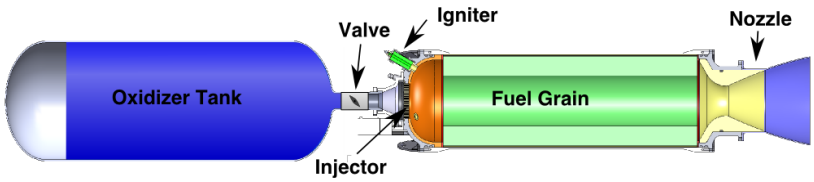

Figure 1.2: Hybrid motor scheme

- it is easy to manufacture.

Hybrid motors have also some disadvantage, particularly low regression rate and efficiency. These drawbacks have limited the widespread use of hybrids. The low regression rate is related to the blocking effect in the grain surface that limit the heat transfer to the fuel wall. The low efficiency is due to the typical features of hybrid combustion. In fact the oxidizer and the fuel enter in the combustion chamber from different path and they burns within a characteristic boundary layer diffusion flame. In this way the efficiency is limited by the amount of mixing in the turbulent boundary layer.

In this thesis one possible solution to main hybrid drawbacks has been proposed, that is vortex injection. Vortex injection increases the wall heat flux and the turbulent mixing. In this way it is possible to achieve high values of regression rate and efficiency. Several researchers tested various type of swirl injection, among which [21] and [34].

Most of this work is about gaseous injection. However, in almost all applications the oxidizer has to be stored in liquid phase in order to achieve a good density impulse. Few experiments have been performed with liquid vortex injection. Some of them have been discussed in [19] with liquid oxygen (LOX), and in [26] and [33] that used nitrous oxide. The results of these works seem to indicate that nitrous oxide gives better results, probably because it decomposes exothermically while LOX is much more difficult to vaporize.

In this work a vortex injector is used to enhance the performance of an hybrid rocket motor with paraffin as fuel and nitrous oxide as oxidizer. At least in the author knowledge this is the first time that liquid vortex injection is used with a liquefying propellant. Paraffin wax permits very high regression rates due to entrainment of liquid droplets. In this work a further increase in the regression rate has been achieved with the combination of entrainment and vortex flow. An increase of more than 10% in combustion efficiency has been demonstrated.

Meanwhile the fluid flow inside the vortex hybrid has been studied analytically and numerically, particularly by means of CFD simulations. These simulations

revealed some interesting features like the presence of a forced vortex flow field and highlighted the mechanism of swirl decay, the main cause being the axial acceleration of the fluid due to combustion.

First the numerical analysis will be presented, followed by the descriptions of the experimental results.

1.3 Scope of this work

This project has the intent to characterize a variable thrust hybrid motor.

With this in mind, we have developed a propulsive system with the aims of achieve a throttle level of 50% in mass flow.

The research program is developed towards new injection system configurations, with the aim of optimizing performance in combustion chambers and avoid the previous mentioned drawback in hybrid propulsion like low regression rate and combustion efficiency.

The work has been divided as follow:

1. a design of the motor has been performed, starting from a mission scenario with requirements definition, followed by a preliminary design and a final configuration;

2. a numerical analysis of the motor has seen the use of both analytical considerations and CFD investigation; a study on basic configurations explained the performance increase; this tool is used also to characterize numerically various configurations of the combustion chambers, the throttling behaviour and different time steps during burn;

3. in the second part, the main part, an experimental characterization of the performance of the motor have been performed; data analysis followed the test campaign and results have been compared with numerical simulations.

Throttling has played a significant role in all this work: in particular, a needle valve has been selected to achieve the mass flow variation. A specific test campaign has been conducted to analyse its performance and to obtain flow coefficients charts. Its use has been extended to burn test on the hybrid motor to reduce oxidizer mass flow up to the throttling level desired (75% and 50%).

Chapter 2

Motor design

The design process of an hybrid rocket follows classical steps:

- requirements identification;
- preliminary design: a low sophisticated analysis is conducted, usually via analytical formulas; a raw size of the object comes out from blank paper;
- detailed design: all ideas come to an end and a single object is the output of this process;
- experimental campaign, to validate performance data.

In our case, all these phases have been part of our design flow, with the following tools:

1. a 0-D analytical transient code has been developed in Matlab
2. 3-D commercial software for CFD study has been used for steady state analysis to give a detailed view of "what happens" inside the combustion chamber;
3. a final prototype (lab-scale motor) has been manufactured and tested; data have been analysed.

The main feature of this process is the 2-way arrow that connect each step: like a wheel in a mechanism can affect and is affected by all others, also here there is a connection between all phases, taking for example data from the last part, the experimental, to tune all mathematical tools previously used.

In this chapter the motor design will be developed, starting from a mission scenario followed by a preliminary design, while in the last part we discuss the detailed design.

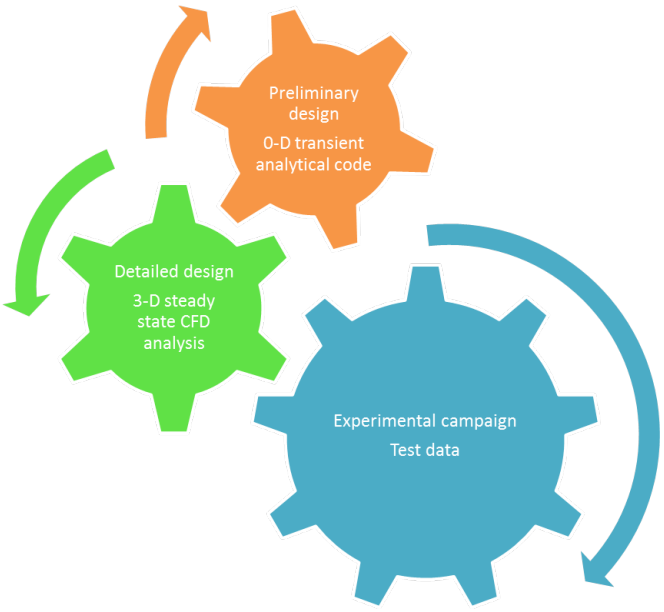

Figure 2.1: Design process scheme

2.1 Mission requirements

Hybrid motors, up to now, have not been developed for low thrust profile (less than 10N). Many alternatives, more efficient, are electric propulsion and mono-propellant motors. For this reason the orbit correction or attitude control is outside the operative range of this kind of thrusters.

The intended use in this thesis is to avoid collision with other satellites or debris and to change in a substantial way the configuration of the formation. In this cases, higher thrust is needed, with a specific requirements or re-ignition.

A mission analysis has been performed with a numerical dynamic model. Details are reported in [29] and [30].

The model suppose a formation flight group composed of two satellites, one called *chief* that present an off-nominal trajectory and one called *duty* that must perform the corrections.

The strategy is splitted in 2 moments: first the spacecraft elaborate and act a strategy exit from the nominal region (Separation Guidance), then it plan and reach a "parking" trajectory (Nominal Guidance) that must remain inside a safe region but outside the nominal boundary.

In this analysis the boundary conditions of the algorithm are:

- simulation step: 0.5s
- initial relative position: [300, 200, -120] m (x, y, z in fig.2.2)

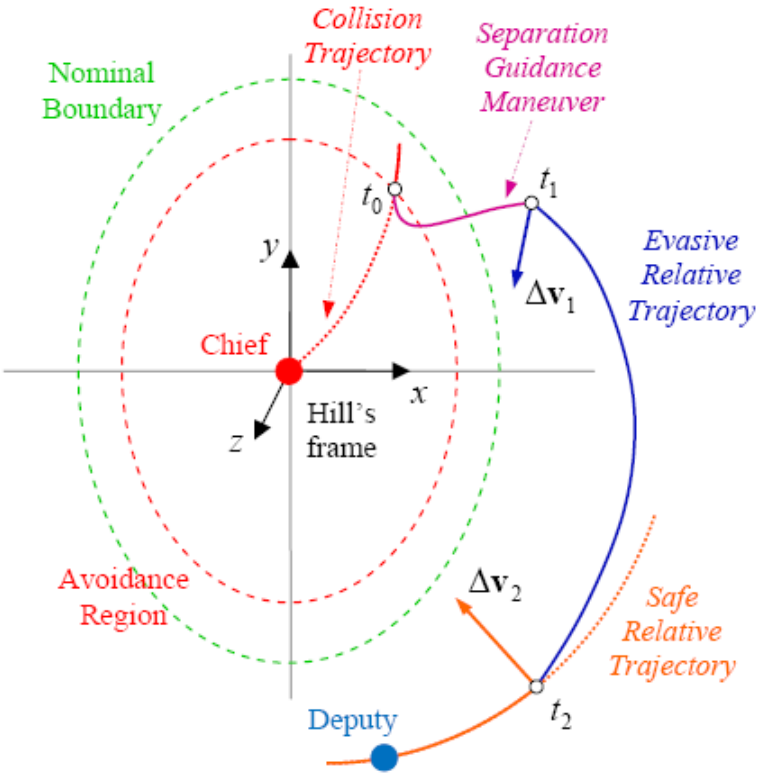

Figure 2.2: Collision avoidance strategy - courtesy of [30]

- collision time: 1 min
- Avoidance region minor semiaxis: 300m
- Nominal region minor semiaxis: 700m
- time to escape from nominal region: 10 min
- duty satellite mass: 1000kg

Results (see fig.2.3 and 2.4) showed that with this data a motor of 500N of nominal thrust is adequate to complete the task with a throttle ratio up to 1:2 (50%).

It has to be said that the maximum thrust level is highly dependent on collision time and satellite mass. For this reason the requirements previously defined is a lower boundary.

The easiest way to achieve throttling in hybrid motors is the mass flow reduction. A continuous thrust level profile is intended in the algorithm. In our work, however, the throttling will be performed in 3 different experiments to understand

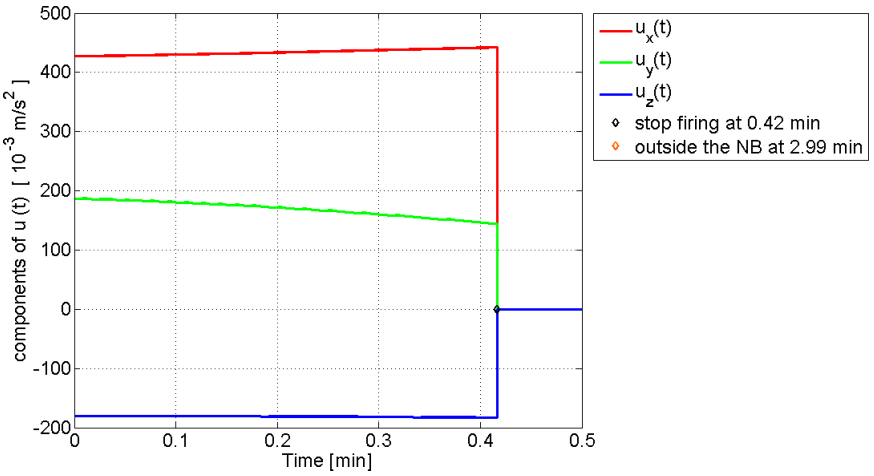

Figure 2.3: Thrust profile of duty spacecraft in collision avoidance algorithm

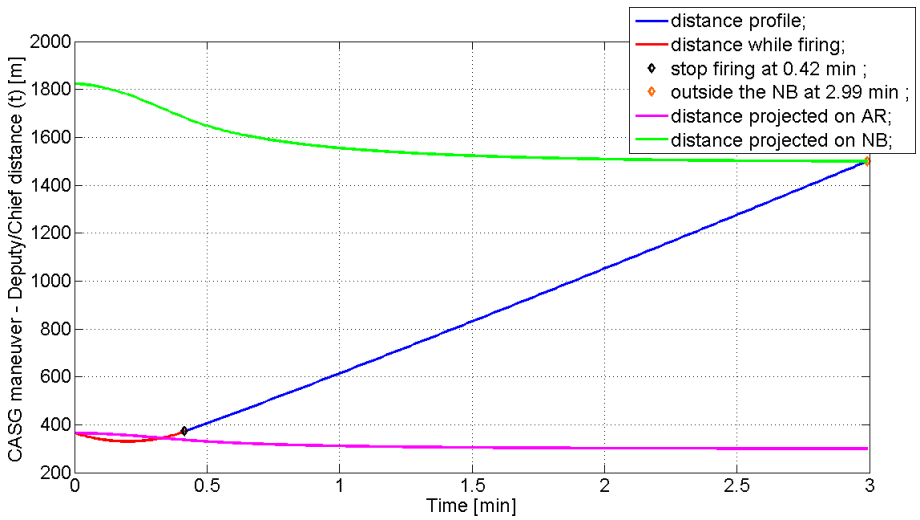

Figure 2.4: Time profile of mutual distance between spacecraft for collision avoidance strategy

the peculiarities that characterize each step. In future works, the transient behaviour will be analyzed.

2.2 Preliminary Design

A Matlab algorithm has been written to predict the performance of an hybrid motor.

The script evaluate transient algebraic equations, and is linked to a thermochemical calculator (CProPep) for the internal combustion process.

This program is the beginning step in the design process of an hybrid rocket, and its use is intended only to have a raw geometry of the motor in terms of combustion chamber and nozzle dimensions and mass flow rates.

One advantage of such an algorithm is the possibility to insert it inside an optimization process to achieve a certain goal like max specific impulse, max thrust...

In our case, the design requirements come from the mission scenario described in 2.1 and the necessity to accomodate the experimental motor in a facility already developed. For these reasons, we achieved the following boundaries:

- nominal thrust: 500÷1000 N;
- maximum grain length: 200 mm;
- maximum oxidizer discharged mass: 4 lit;
- throttling levels: 75% and 50%.

Input parameters are the following:

- grain data: length, inner and outer diameter, density;
- oxidizer data: tank pressure and temperature;
- nozzle data: exit and throat diameter, exit pressure;
- injection data: 3 possible injector models have been implemented, Bernoulli equation, chocked flow, fixed mass flow;
- combustion data: combustion efficiency (imposed) and regression rate coefficients.

As previously reported, the algorithm (see fig.2.5) proceed in transient calculations, with fixed timesteps. In the following we are goint to illustrate the mechanism of the code. The index *i* indicate the actual iteration, while *i-1* indicates data from the preceding timestep.
All equations can be found in [15] and [28]. Only the combustion process product calculation is treated externally, with a call to an external thermochemistry program.

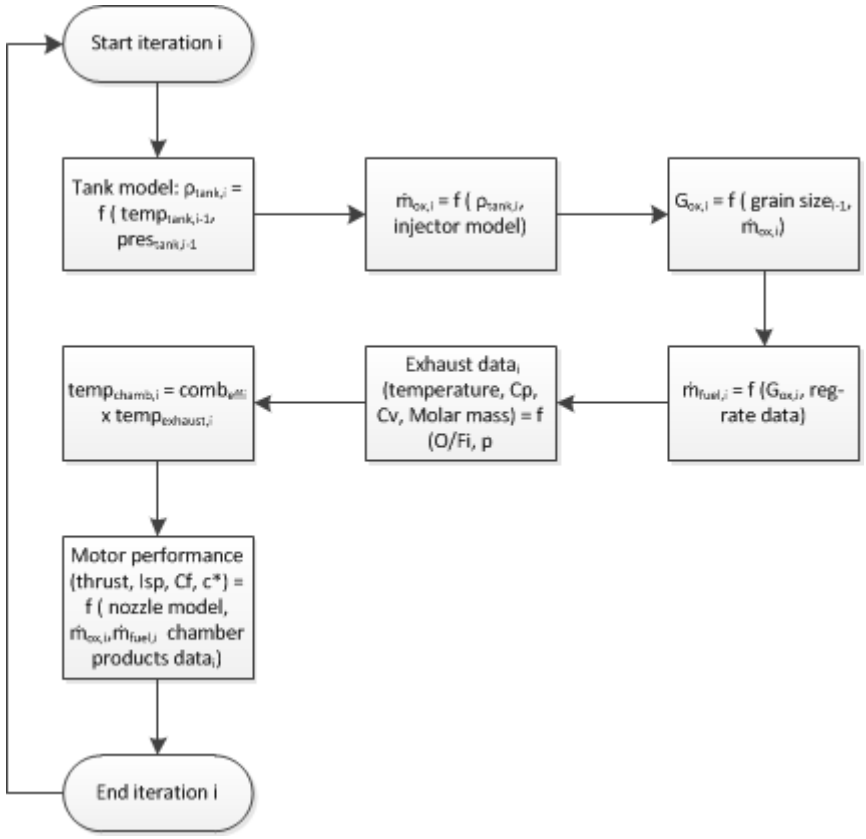

Figure 2.5: 0-D transient analytical code scheme

One of the main constraints that a code for an initial phase of a project must fulfil it that it has to be fast, because many models need to be evaluated and the program has to be run many (hundred) times. In this view, the running time of this code in a Intel Core2Duo 2.00GHz and 4GB of RAM, using a timestep of 10^{-4}s and a total burning time of 4s is in the order of a few (3 - 5) seconds, excluded the plotting time that depends on graphic card.

This program permits to know the evolution of the performance parameters:

- grain size and regression rate;
- oxidizer and fuel mass flow and flux, O/F ratio;

- chamber and nozzle pressure and temperature;
- combustion products parameters: temperature, Cv and Cp (specific heats), molar mass;
- rocket performance parameters: thrust, Isp, Cf, c*.

As an example, the following is the text output of the code for the experimental geometry described later in these pages:

```
Initial internal diameter = 25.0mm
Final diameter = 58.6mm
External diameter = 70.0mm
Grain length = 145.0mm

Nozzle data
Throat diameter = 16.0mm
Exit diameter = 29.0mm
Throat area = 201.1mm2
Exit area = 660.5mm2
Expansion ratio (Ae / At) = 3.3
Outlet pressure = 1.00bar

Tank data
Tank in pressure regulated mode
Oxidizer pressure = 80.00bar
Oxidizer temperature = 298.15K
Oxidizer temperature = 25.00°C

Injector data
Showerhead - bernoulli equation
Number of holes = 6.00bar
Diameter of single holes = 1.20mm
Total injection area = 6.79mm2
Discharge coefficient (Cd) = 0.60

Total burning time = 3.0s
```

```
Efficiency = 95.0%

Total impulse = 2627.5N*s

Burned fuel mass = 0.296kg
Burned oxidizer mass = 1.050kg
Burned oxidizer volume = 1.412lit
Final diameter = 58.6mm

Performance data
|      |  O/F  |    T    |   Isp   |   c*    |   Cf    |
|      |       |   [N]   |   [s]   | [m/s]   |         |
| Max  |  3.6  |   875.5 |  199.1  | 1351.5  |   1.44  |
| Mean |  3.6  |   875.5 |  199.0  | 1351.5  |   1.44  |
| Min  |  3.5  |   875.5 |  199.0  | 1351.4  |   1.44  |

Various data
|      |    Gox    | mdot_ox | r_rate | mdot_fuel | mdot_tot  |
|      | [kg/s*m2] |  [kg/s] | [mm/s] |   [kg/s]  |   [kg/s]  |
| Max  |   713.0   |  0.350  |    9.3 |   0.099   |   0.449   |
| Mean |   270.6   |  0.350  |    5.6 |   0.099   |   0.449   |
| Min  |   130.0   |  0.350  |    4.0 |   0.099   |   0.449   |

Pressure data [bar]
|      | Tank    | Chamber | Throat | Exit   | Inj Dp |
| Max  | 80.00   | 30.15   | 16.49  |  1.48  | 49.85  |
| Mean | 80.00   | 30.15   | 16.49  |  1.48  | 49.85  |
| Min  | 80.00   | 30.15   | 16.49  |  1.48  | 48.57  |
```

First thing that comes out is the nozzle expansion, not adapted to ambient pressure. The reason is that this nozzle, as the title of this thesis says, must work in different condition due to mass flow throttling, so it has been decided to use it under-expanded (expansion waves outside the nozzle) in nominal conditions, and slightly over-expanded in low (up to 50%) mass flow tests.

In fig.2.6-2.10 transient data results are plotted. Again, the not adapted nozzle shows its effects in a low Isp values.

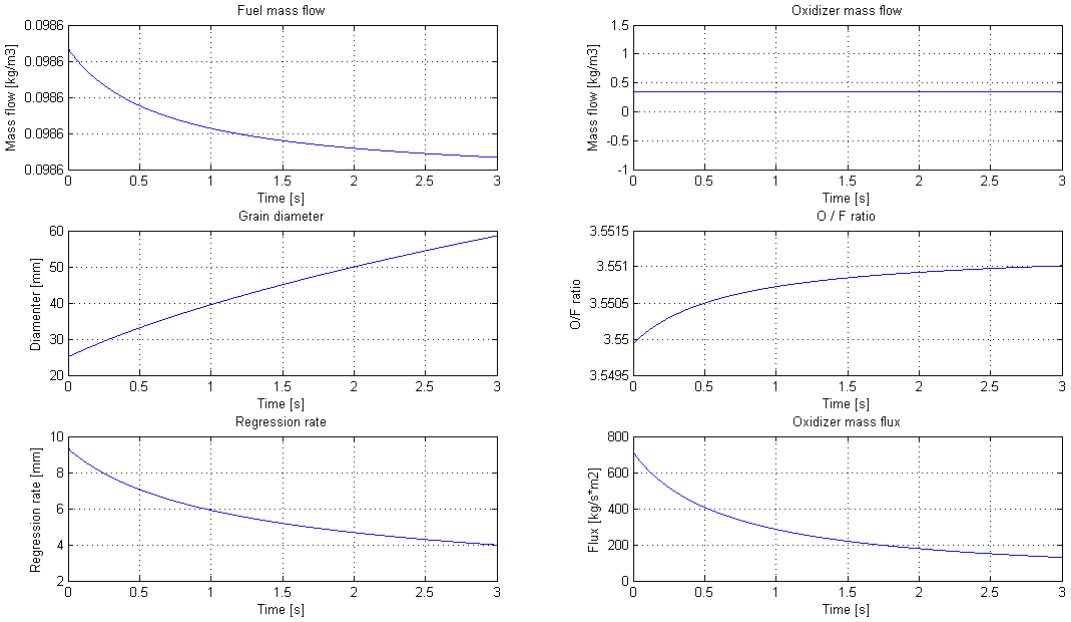

Figure 2.6: 0-D transient analytical code results: mass flow data

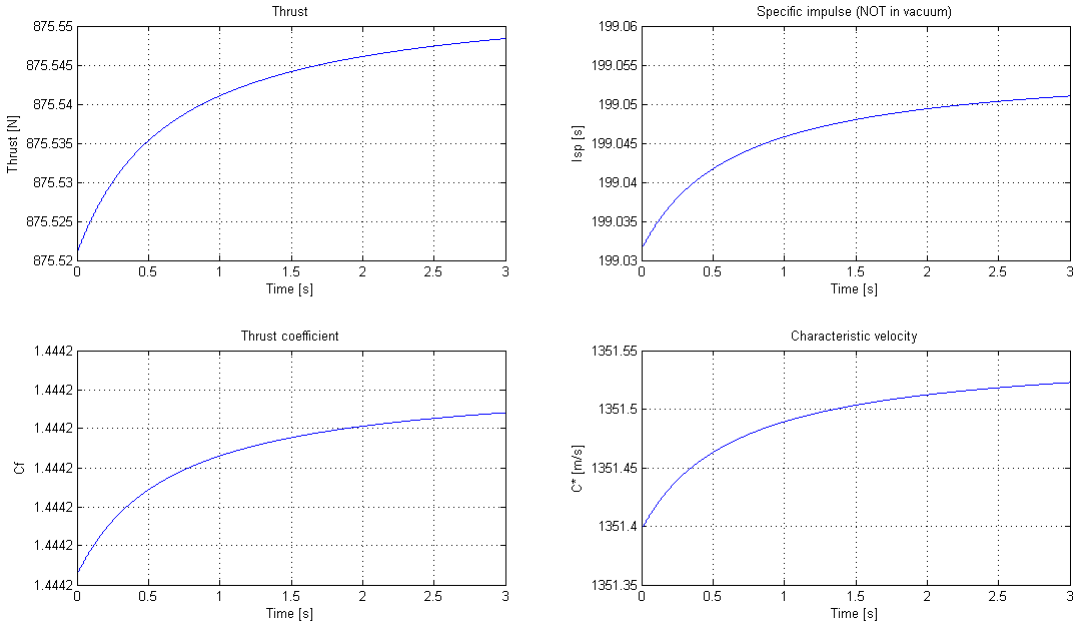

Figure 2.7: 0-D transient analytical code results: rocket performance data

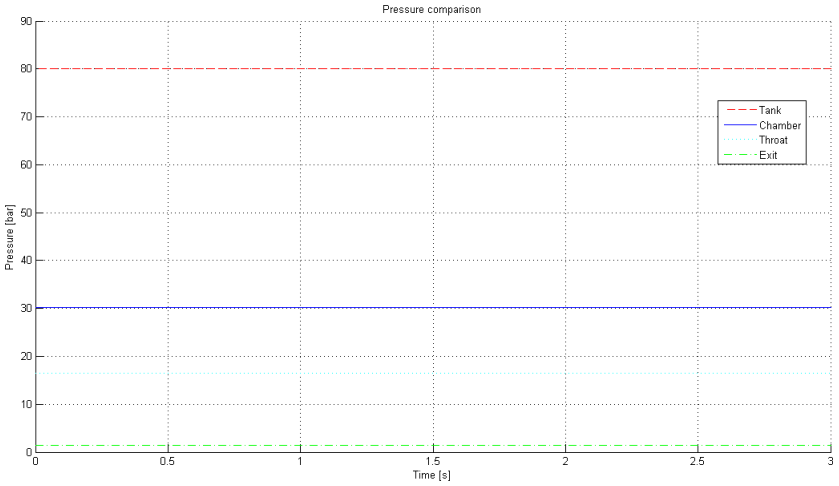

Figure 2.8: 0-D transient analytical code results: pressure review

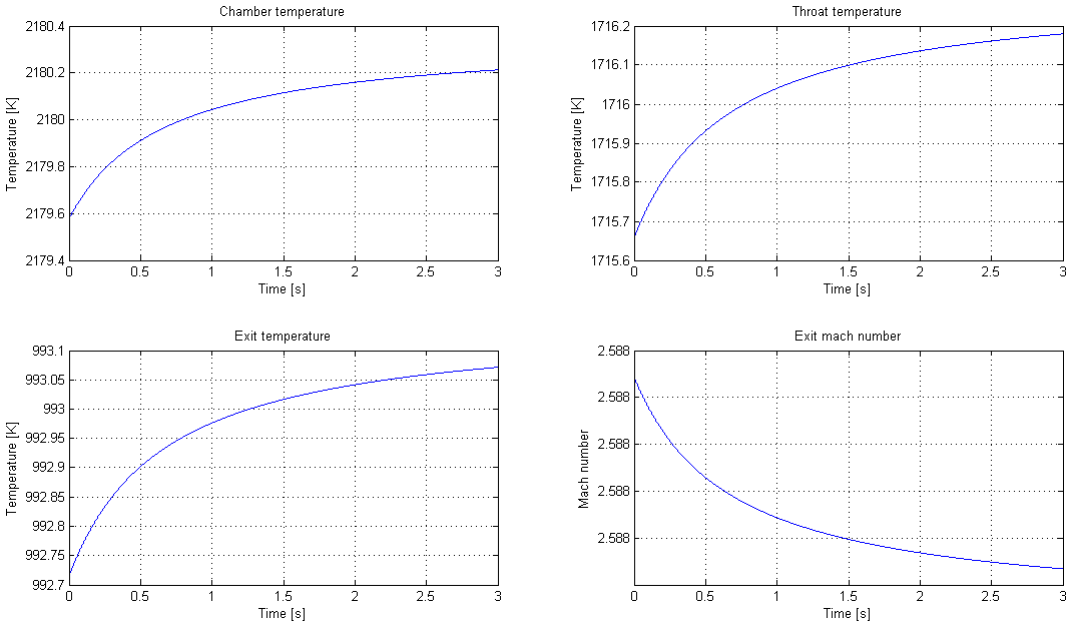

Figure 2.9: 0-D transient analytical code results: temperatures data in chamber and nozzle and mach number at nozzle exit

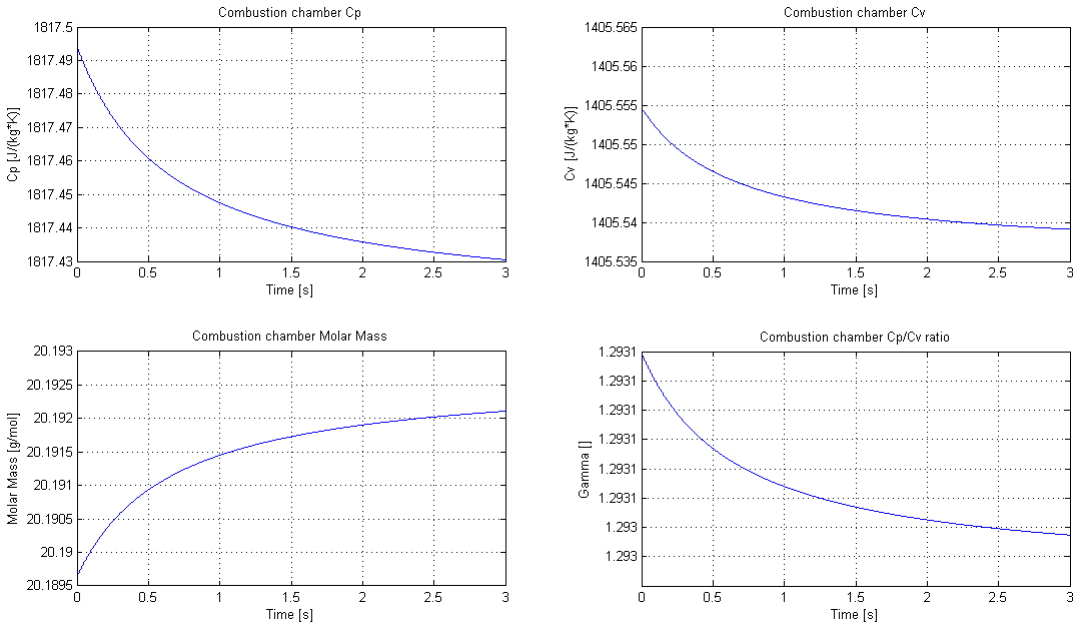

Figure 2.10: 0-D transient analytical code results: combustion products properties

Chamber (and all the others) pressure are obviously constant, due to the fixed mass flow and tank pressure conditions imposed by the models: this comes out from experimental data and a $n = 0.5$ exponential coefficient for regression rate.

Also chamber temperature is very low, due to a low O/F ratio (3.6 mean).

2.3 Final configuration

The design of the motor has begun from the given requirements coming from the mission scenario and preliminary design.

In particular, fixed parameters were:

- oxidizer mass flow - nominal (0.35kg/s) and throttled (75% - 50%);
- injection: number (6) and diameter (1.2mm) of holes;
- grain length (145mm) and inner diameter (25mm);
- nozzle throat (16mm) and exit (29mm) diameter.

The design had some constrains (total length and maximum diameter) due to the fact that the combustion chamber casing has been refurbished from other previous experiments in our laboratory.

The rocket consists in the following parts, reported in fig.2.11:

1. nozzle;

2. pressure pick-up point;

3. pressure sensor adapter;

4. nozzle closure system;

5. paraffin grain;

6. injector system;

7. ignition zone;

8. oxidizer inlet.

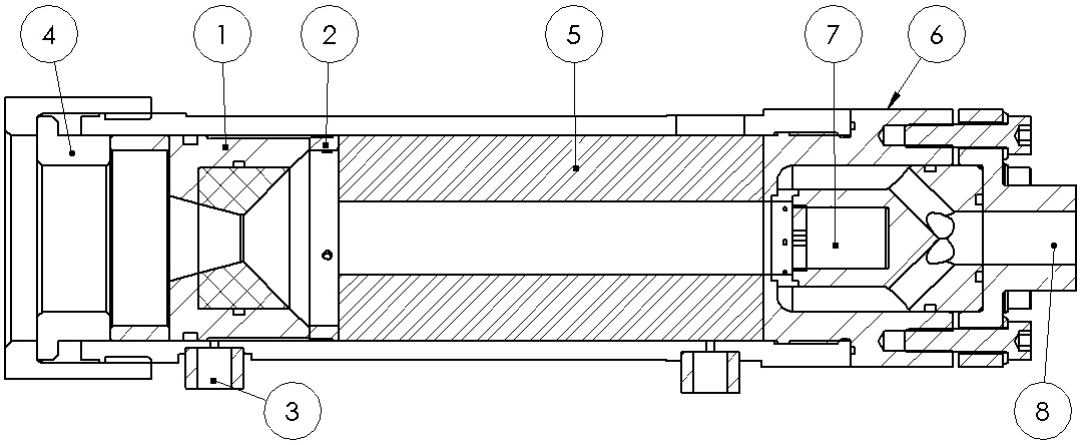

Figure 2.11: Hybrid motor scheme

Between 8) and the oxidizer tank is placed an electro-pneumatic ball valve and the needle valve to reduce the mass flow.

All manufactured components have been designed from a structural point to withstand a pressure of 80bar with a minimum safety factor of 4 (it's a battleship motor, it doesn't have to fly). Parker silicone rubber (a material compatible with nitrous oxide) o-rings assured the needed sealing, without being corrupted by the oxidizer.

The motor is ignited with a solid charge and the ignition starts thanks to an electric resistance that with an over-voltage takes fire. After 3.5s the igniter is started and the oxidizer valve is opened. The time delay between the valve-starting signal and the pressure rise in the chamber has been evaluated in 0.2s in opening and 0.1 in closing. However, this data is not important because it is not used during data analysis.

2.3.1 Injection

Injection design covered two type of injectors, one axial and one vortex. A common driver design was the L/D ratio (orifices length over diameter), which value was fixed at 4.6. The selected material for these components was stainless steel AISI 316.

The total injection area is $6.79mm^2$. This value is derived from the preliminary analysis (see chap.2.2) to obtain the desired mass flow (350g/s).

Axial injector is composed of three parts (see fig.2.12):

1. motor head;
2. axial injector plate;
3. feed line to motor interface;
4. oxidizer inlet.

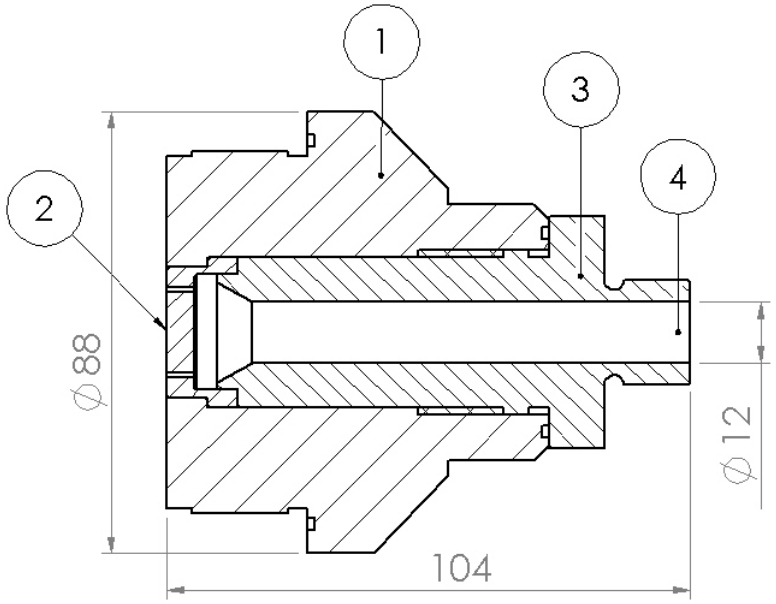

Figure 2.12: Axial injector assembly (dimensions in mm)

Injection plate is showed in fig.2.14. As can be seen, there are 6 drilled holes with a diameter of 1.2mm that lie in a circumference of 17mm of diameter.

Oxidizer comes from a hole in the interface of 12mm of diameter (see fig.2.13(b)). All feed line has size of 1/2".

Vortex injection assembly is depicted in fig.2.15. Components are the following:

1. flux diverging;

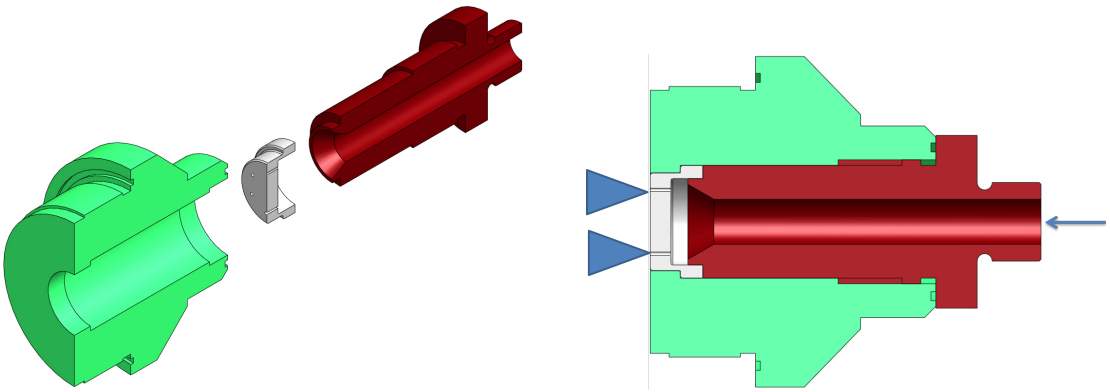

(a) Exploded view (b) Flow path

Figure 2.13: Axial injection view

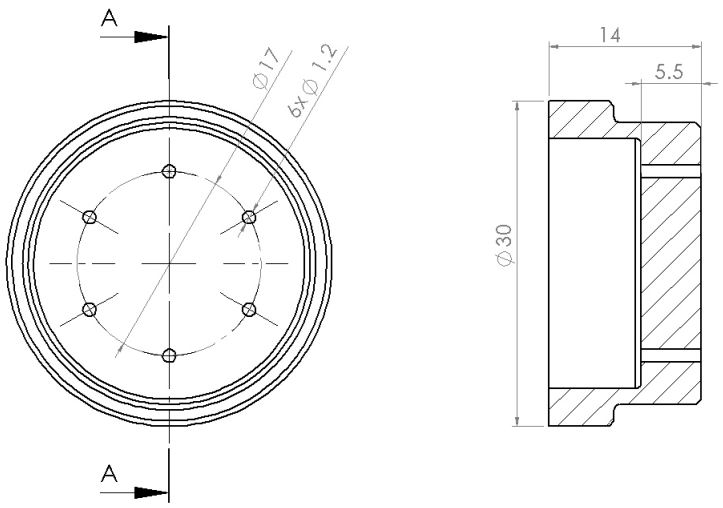

Figure 2.14: Axial injector plate (dimensions in mm)

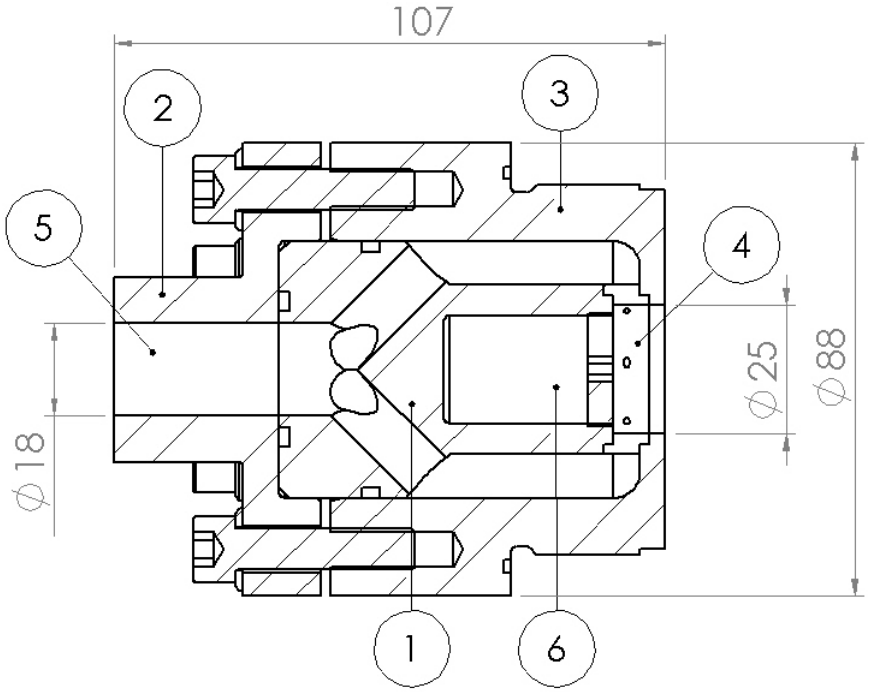

Figure 2.15: Vortex injector assembly (dimensions in mm)

2. feed line interface;

3. motor head;

4. injector plate;

5. oxidizer inlet;

6. igniter chamber.

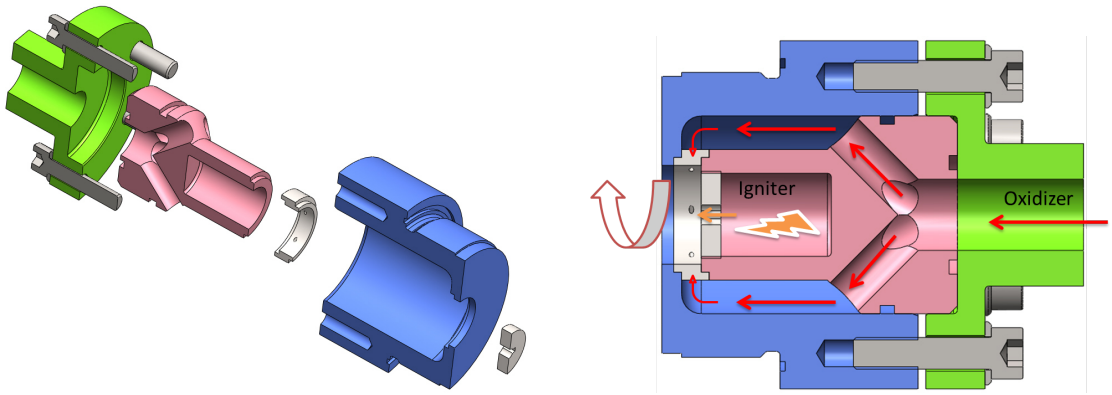

(a) Exploded view (b) Flow path

Figure 2.16: CFD Geometry

The vortex injector assembly (see fig.2.16(a)) is used for both injection and ignition: it hosts a small chamber (33mm length, 21mm diameter) in which pyrotechnical igniter are accomodated.

Flow comes from the feed line trough an 18mm diameter hole, then is splitted in 6 channels of 10mm of diameters, needed to deliver the fluid on the outer section where it encounters the injection plate that impress the tangential velocity.

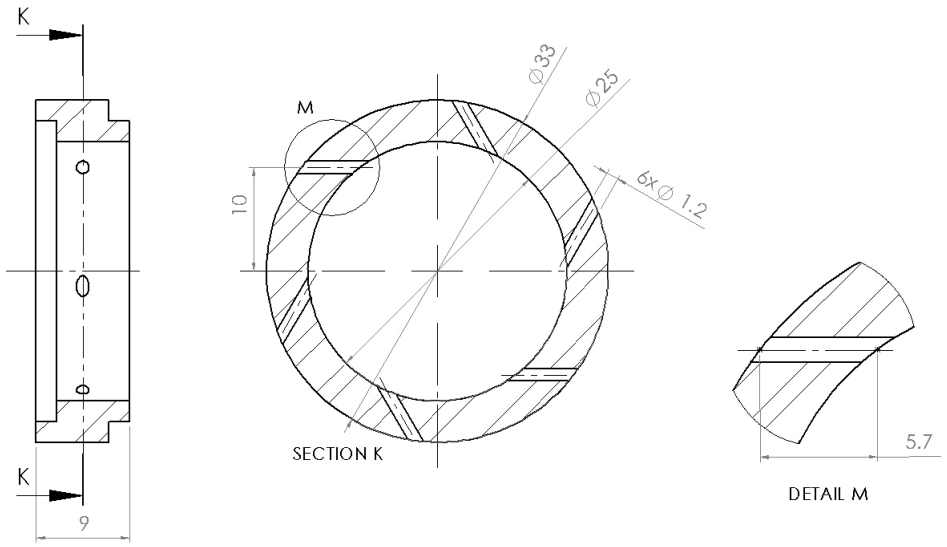

Figure 2.17: Vortex injector plate (dimensions in mm)

Injector plate can be seen in fig.2.17. It takes the oxidizer from a diameter of 33m down to 25mm, with 6 tilted holes of 1.2mm in diameter. As previously reported, a pre-requisite was to have a L/D ratio of 4.6: channels are drilled in a cylinder, and so to define their length we take the mean length (5.7mm) showed in the detailed view of fig.2.17. It has to be clear that dimensions where driven not only by the L/D ratio parameter; to accommodate many constraints and reach a "good enough" design, a final value of L/D of 4.7 was achieved.

2.3.2 Combustion chamber

Combustion chamber casing is a steel tube of 70mm inner diameter. Inside, all possible devices (pre-chamber, post-chamber, mixer) take place together with the paraffin grain and the nozzle.

Paraffin grain is manufactured using Parasur wax and carbon black powder, casted in a cylindrical mold. After cooling in air, it is extracted and finished in a turning machine to achieve the correct dimensions: 145mm length, 25mm inner diameter and 70mm outer diameter.

Pre-chamber and post-chamber are simple AISI 316 stainless steel cylinder, with inner diameter of 60mm, outer diameter of 70mm (to accomodate inside the casing), and length of 10mm and 20mm (depending on the test choice).

Mixer is a device similar to a drilled diaphragm; an analogous geometry is reported in [8] (see fig.4.20).

The idea behind a such long casing (233mm of available length) respect to the grain (145mm length) and nozzle (58mm with the spacer) is to accommodate different possible motor configuration. In particular:

- *basic*: only the grain and the nozzle (fig.2.18(a));
- *pre*: a pre-chamber of 20mm length before grain (fig.2.18(b));
- *post*: a post-chamber of 20mm between nozzle and grain (fig.**??**);
- *mixer*: a mixer between grain and nozzle;

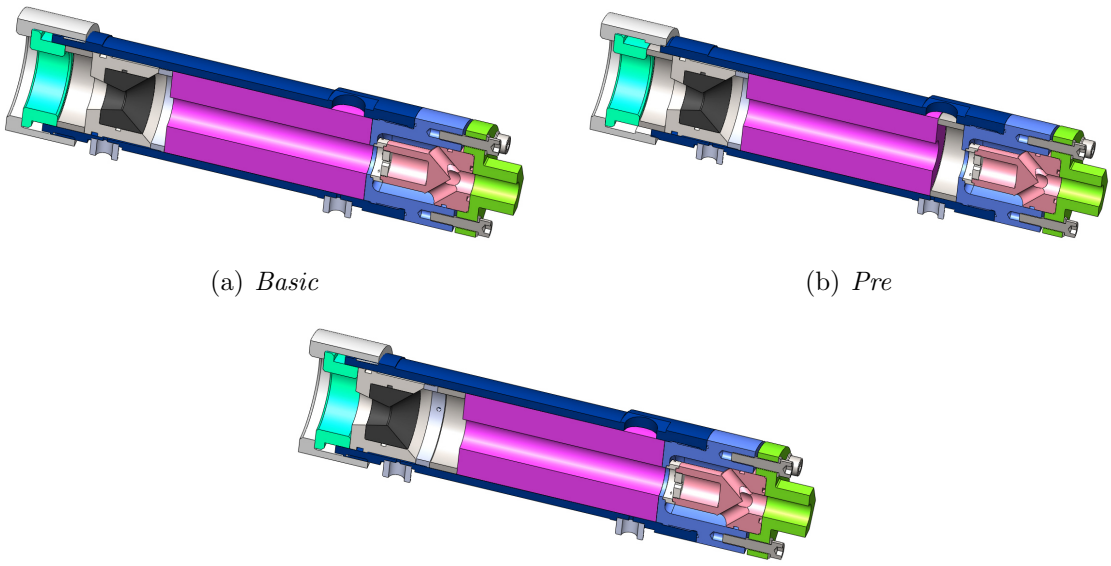

(a) *Basic* (b) *Pre*

(c) *Post*

Figure 2.18: Possible motor configurations

2.3.3 Nozzle

To design the nozzle the 0-D transient code has been used (see 2.2).
Constraints were:

- outlet pressure = 1bar;

- chamber pressure with vortex injection and 100% mass flow = 30bar;
- no internal shock waves at low oxidizer mass flow

In particular, the last requirements involved the fact that at full oxidizer mass flow (0.35kg/s) the nozzle will be under-expanded with an exit pressure of 1.48bar. On the other side, when a reduction with the needle valve is performed, pressure at nozzle exit will drop at 0.73bar, becoming over-expanded.

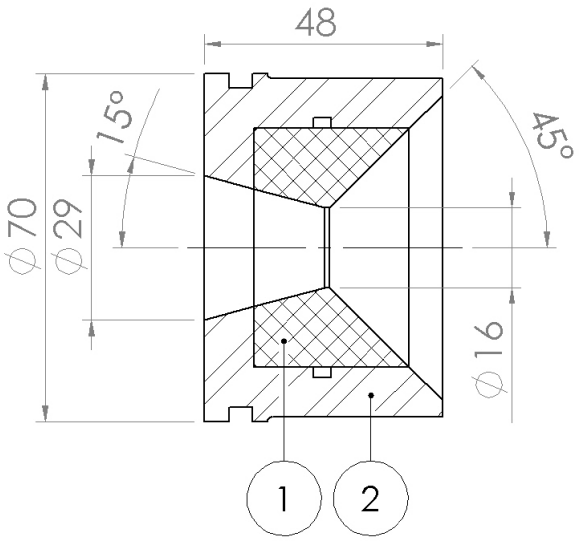

Figure 2.19: Nozzle (dimensions in mm)

It has been manufactured in two pieces, as reported in fig.2.19: the outer (2) in AISI 316 stainless steel, while the inner (1) in graphite.

The reason is that the outer parts must withstand impulsive forces in ignition and pressure difference in the contact zone with the other components, and steel is more ductile. On the contrary, in the throat section the most important parameter is the high temperature, and graphite can withstant those values (from 2000K to 3000K).

Experience on other components, the low test duration and small dimensions showed that there are no problem for material expansion due to heating. From an engineering point of view, table 2.1 summarize most significant properties (all are referred at ambient temperature).

It can be seen that both materials have similar tensile strength. Graphite has a higher thermal conductivity that gives rise to lower thermal gradients. Furthermore, heat from exhausts pass quickly through it toward steel. It has a higher coefficient of thermal expansion (C.T.E, 1 order of magnitude greater) and a lower (again, 1 order of magnitude) specific heat, that means that given the same amount

Table 2.1: Graphite vs. stainless steel properties

	Graphite	**Stainless steel**
Specific heat [J/(kg K)]	2.5	16
C.T.E. [μm/(m K)]	115	16
Conductivity [W/(m K)]	790	500
Tensile strength [Mpa]	260	290

of heat it will reach sooner the steady state temperature. Both these last values would require a proper thermal design. Experience on previous nozzle design told us that a clearance of 0.1mm on the graphite external diameter would be safe enough.

2.4 Performance parameters

In this section a schematic overview of the performance parameters will be described.

It is important to understand which are the main source of influence in a hybrid motor, to define a strategy to optimize them.

What follows is a qualitatively overview of these parameters, that are described more in detail in chap.6.2.

In this thesis the aim is:

- obtain a nominal thrust between $500 \div 1000N$;
- increase the regression rate, raising the a coefficient up to 0.3 mm/s;
- increase the combustion efficiency up to 90% without the use of special devices inside the combustion chamber but only using a different injection method (vortex instead of axial);
- reduce chamber pressure oscillation, with a value less that 4%.

These value are not part of the design process, but need to be validated with an appropriate experimental campaign.

Chamber Pressure

This is the most important information to know about a hybrid motor. It is divided in two parts:

- mean value;

- oscilations.

The first information is important to understand the behaviour of the motor, and is used to derive other fundamental values like combustion efficiency. The knowledge about its trend is needed to validate and measure the regression rate parameters.

Oscillations are an important parameter to reduce variations in the operative parameters of the thruster. A typical value that divide a stable from an unstable motor is that the oscillations must stay within the 5% of the mean pressure value.

Combustion efficiency

In a rocket there are basically two types of energy conversions: one involving chemical processes in the combustion chamber and one involving the transformation of energy in a "temperature" form into a more convenient (for thrust purposes) "velocity" form in the nozzle section.

Combustion efficiency is, in word, a parameter to measure the effectiveness of the combustion process in chamber, compared to a theoretical value dependent only on chemical properties of species involved and chamber and exit pressure.

In chemical rockets, a correct definition is the following: the ratio of the actual and the ideal heat of reaction per unit of propellant and is a measure of the source efficiency for creating energy.

Typical values of combustion efficiency goes from 68% for simple axial injection motors up to $95\% \div 99\%$ for well designed combustion chambers, with particular devices inside and/or different injection type.

The combustion efficiency is evaluated from the characteristic velocity, a parameter defined as:

$$c^* = \frac{p_c A_t}{\dot{m}_t ot} \tag{2.1}$$

This value is both measured experimentally and calculated with a thermochemical software to give the optimal theoretical value. The ratio between these two results gives the combustion efficiency.

Regression rate

Regression rate is a measure of how much fuel has been burned during a test.

In the design is imposed by the use of specific formulations derived from experimental data.

When some changes are performed in the motor configuration, like a different injection o some devices inside combustion chamber, a specific experimental campaign must be performed to analyze the new grain behaviour.

With the use of paraffin the regression rate has a particular behaviour, because there is not only the erosion and ablation of the burning surface like in classical solid motors theory, or like other material (e.g. HTPB), but presents a melted layer of liquid wax, and there is the presence of the entrainment of liquid droplets from this film [6].

Thrust

Thrust is the initial parameter that drives the design of the motor. It is given by a mix of other design choice (nozzle dimensions, mass flow, injection), and can be measured in a direct way by the use of load cells.

Chapter 3

Flow field analysis

CFD (Computational Fluid Dynamics) is a powerful tool that helps the comprehension of the phenomena behind what is measured experimentally.

In this thesis the use of CFD has played multiple role:

1. to help in the comprehension of the basic phenomena that influence the flow field inside combustion chamber;

2. to characterize the measurement system, helping the data analysis in sensor choice and positioning, with both a 3D CFD commercial software and a 0-D analytical tool.

It has to be noted, that the software used has already been validated with hybrid motors. Further details can be found in [8].

It is important, indeed, to discover why the vortex injector perform an higher regression rate and combustion efficiency. The CFD 3-D code has been useful in this purpose.

In this chapter will be discussed and explained what experimental data has seen and measured, reported in chap.6.

Moreover, an analytical formulation for vortex flow field have been developed to express pressure gradients in combustion chamber, helping in the choice of sensors position.

3.1 CFD Model

In this section, a schematic view on hot to set up a simulation using commercial software is explained. In CFD is important to notice that every simulation could have its own issues, problems and solutions to them.

As an example, an important parameter that must be checked out to achieve convergence is the relaxation parameter, that needs to be tuned if the default value do not satisfy the solution.

Both axial and tangential injection have been studied, with two deeply coupled aims on this investigation:

1. find and define the main difference between vortex and axial injection;

2. understand the behaviour of the vortex flow field inside the combustion chamber.

The correct simulation of injection is a crucial point: the speed of fluid that enters the combustion chamber can change radically the solution, leading to an incorrect understanding of the problem. In this case, there are two distinct situations, the case with vortex injection and with axial injection.

3.1.1 Geometry and mesh

A model of the internal fluid volume of the combustion chamber has been simulated. The geometry consists in a cylindrical grain, a conical nozzle and an injector section. Some simulations have been conducted without nozzle, to evaluate the effect of this component in the straightening of the flow line due to the acceleration of the fluid. It will be shown later that the pitch of the helical fluid flow is not constant but can vary depending on geometry, presence of combustion or a nozzle after the combustion chamber. Other groups on simulations are needed to demonstrate the utility of special devices like mixers or post/pre-chamber, or to explain the different (or not) behaviour during throttling, changing the size of the internal grain diameter.

Basically, the geometry can be divided in three sections (see 3.1(a)):

1. injection: it can be axial or vortex, and from here the oxidizer enters the combustion chamber;

2. combustion: this is the grain part, where oxidizer and fuel (injected in this zone) react;

3. expansion.

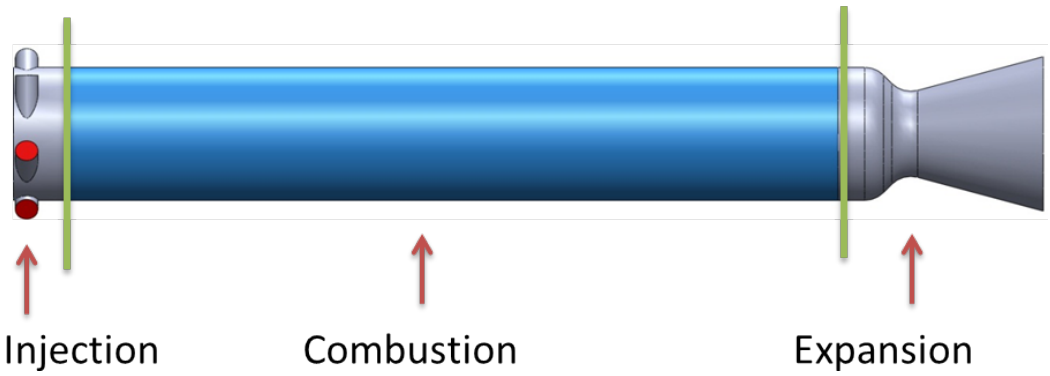

(a) Model geometry

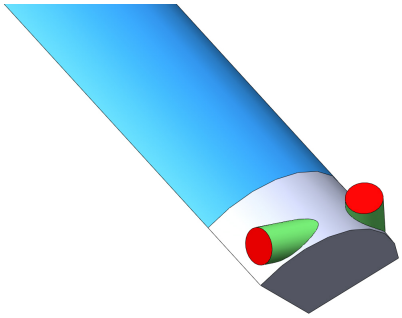

(b) Vortex injection

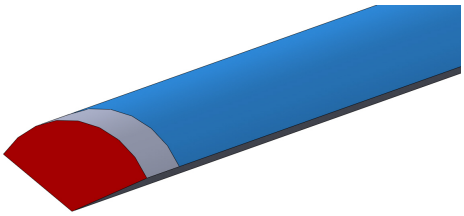

(c) Axial injection

Figure 3.1: CFD Geometry

In fig.3.1(a) can be seen in blue where fuel is injected in combustion chamber, while in red are presented the oxidizer injection channels.

All tested geometries have predominant planes of symmetry, thus this function has been used in analyses; the geometry tested in this work has 6 injection channels, so a first trial was a split of a 1/6 section. Results showed that the solutions weren't the same (difference of more than 20%) with the same mesh. At the end of this process, it has been clear that the correct section is 1/3, because interaction between fluxes that exit each channels are not negligible and must be simulated in a more precise way (see fig.3.1(c) and fig.3.1(b)). The use of symmetry enables a great reduction in element numbers and thus in computational cost. This permitted the use of a finer mesh, given the same (no more that 2 millions) number of elements.

Details of the mesh are the following (see 3.2):

- unstructured tetrahedrical mesh;
- maximum element size: 1mm;
- maximum face size: 1mm;

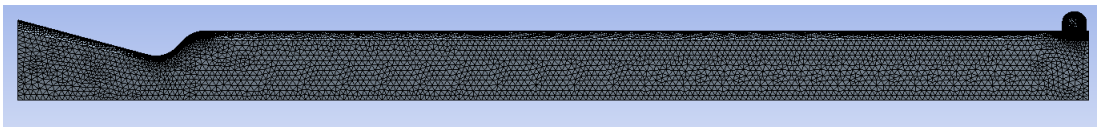

(a) Mesh - general

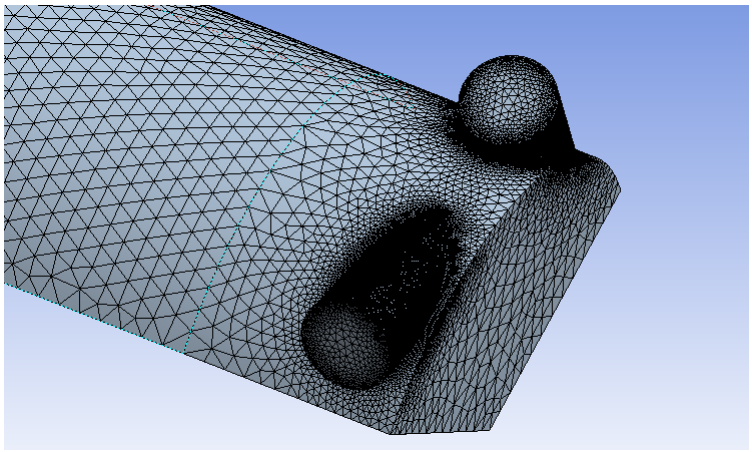

(b) Mesh - injection detail

Figure 3.2: CFD Mesh

- mesh refinement on external surface of nozzle throat, element size of 0.5mm;
- mesh refinement on external surface of injection channels (green in 3.1(b)), element size of 0.1mm;
- number of elements: $\approx 1.5 \div 2 * 10^6$.

Mesh definition has been obtained with an iterative process reaching a stable condition: difference in solution, evaluated as chamber pressure, temperature and fluid speed, between two meshes have to be under 4%.

3.1.2 Setup

The oxidizer is N_2O injected at 25°C, while the fuel is paraffin, injected at 725K already decomposed in the following reaction:

$$C_nH_{2n+2} \rightarrow H_2 + (n/2)C_2H_4$$

Boundary conditions are:

- inlet with fixed mass flow on surfaces where fuel and oxidizer are injected;

- outlet at exit nozzle, with fixed pressure at 1bar;
- wall with no slip condition in the other surfaces;
- when no nozzle is in the geometry, opening condition at fixed pressure where the flow exits.

The turbulence model used is $k-\omega$ with scalable wall functions. Choice on the model have been performed between classical ones, like $k-\varepsilon$. After some test simulations, it has been clear that with axial injection no problems arise in any case both pointing to convergence and solution accuracy [8], while with vortex injection the convergence is very difficult, and proper turbulence scheme and model is a fundamental choice to get a stable result.

Main simplifications are:

- ideal gas equation for all substances;
- oxidizer injected in gaseous state;
- fuel injected already decomposed and in gaseous state, and without the effect of droplets;
- simplified chemical reaction: only one reaction, no backward reactions, no homogeneous decomposition due to temperature effects;
- no kinetic effect in reaction.

The chemistry of the flame is treated with the eddy dissipation model. The reaction formula is the following:

$$151N_2O + H_2 + 25C_2H_4 \rightarrow$$
$$148N_2 + 23CO_2 + 27CO + 40H_2O + 10O_2 + 6NO + 10OH + 2O + 5H_2 + 2H$$

Products are in decreasing order of mass concentration. The selection of the products comes from an analysis of the combustion with a thermochemical software (Cpropep), choosing only those chemical species that have a molar fraction more that 10^{-3}. A comparison between the formula applied in these simulations and Cpropep calculation is shown in fig. 3.3.

Kinetic effects have not been included in the simulation since the combustion regime is driven by diffusion. This solution has already been validated in previous

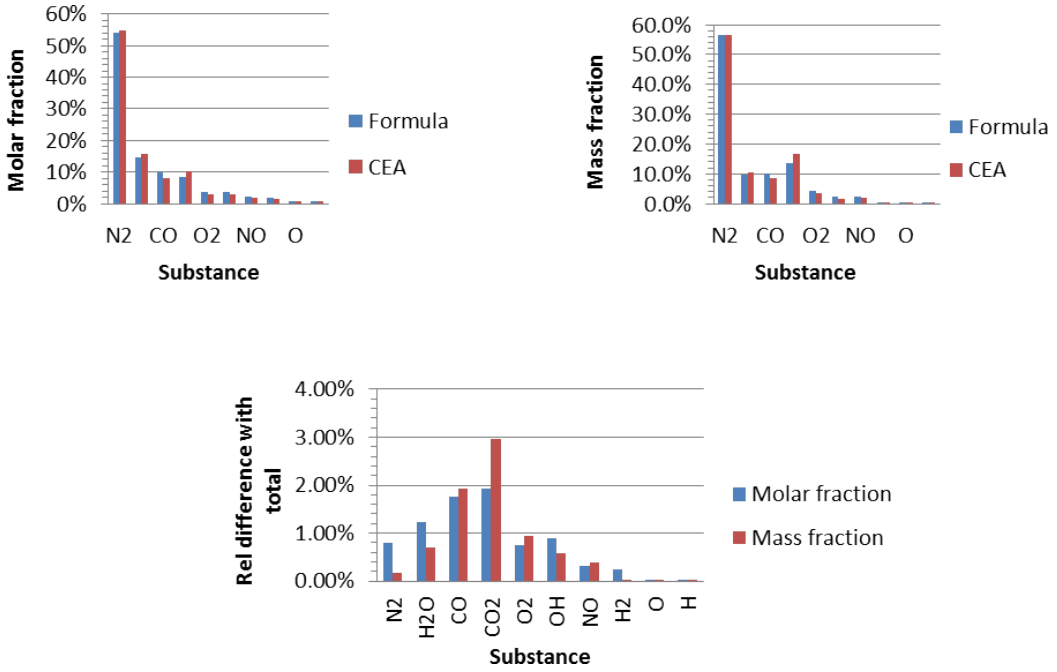

Figure 3.3: Comparison between CFD chemistry formula and thermochemical calculations from CEA

works [8] in hybrid rockets CFD simulations and is justified by the high Damköhler number.

Injection is a special topic: in axial case, all the back surface (in red in fig. 3.1(c)) has been defined as inlet. This has been proved to be valid and more accurate than (like in vortex case) simulate every orifice. The reason is the too high turbulence that would be created due to a too high injection speed. Actually, when oxidizer is injected in combustion chamber is in liquid state, and then evaporate in a certain length; the effect of evaporation is a slow down of the fluid. Specific mixed liquid-gaseous simulations [24] showed this phenomenon. In vortex case, however, there is the difference that the injection channels do not aim directly in the combustion chamber, so this effect is far more effective.

The injection channels are oversized respect to the true ones, because the simplification of gaseous oxidizer would have led to a too high injection velocity. A similitude with liquid injection have been calculated with the following scheme:

- from experiments, the mass flow has been extrapolated;
- given temperature and pressure, density has been calculated with isentropic equations;
- real hole dimension and mass flow permit to evaluate velocity;

- new hole diameter have been estimated, using the same mass flow and velocity of the liquid case, but with density given from the CFD input.

As an example, 6 holes of actual 1.2mm in diameter grow to 4.3mm with a mean chamber pressure of 30bar.

A significant value in vortex flows is the swirl number (S). It is defined as [18] the axial flux of the swirl momentum divided by the axial flux of the axial momentum times the equivalent nozzle radius:

$$S = \frac{G_\theta}{G_z \frac{d}{2}} \tag{3.1}$$

where:

$$G_\theta = \int_0^R \rho u_z u_\theta + \rho \overline{u_z' u_\theta'} r^2 dr \tag{3.2}$$

$$G_z = \int_0^R (\rho u_z'^2 + \rho \overline{u_z'^2} + (p - p_\infty)) r dr \tag{3.3}$$

After some semplifications, equation 3.1 becomes:

$$S = \frac{\int_{R_i}^{R_o} \rho u_z u_\theta 2\pi r^2 dr}{\int_{R_i}^{R_o} \rho (u_z^2 - \frac{u_\theta^2}{2}) 2\pi R_0 r dr} \tag{3.4}$$

These formulations are not easy to use in design, because the fluid field is not well known, thus another parameter has been developed, the geometrical swirl number (S_g) [10]:

$$S_g = \frac{(R_{inj} - R_{port}) R_{inj}}{N R_{port}^2} \tag{3.5}$$

where R_{inj} is the radius of the injector that face the combustion chamber, R_{port} is the radius of the injector channels and N is the number of them (see fig. 3.4).

For technological reasons, in our tests the injector wasn't fully tangential (as in fig. 3.4(a)) but was slightly inside the injector port. In this case, we applied a correction on the formula, taking for R_{inj} the maximum distance between the axis of the injector and the injection channels (see fig. 3.4(b)).

Another correction regards the fact that the fluid is in liquid state, while these formulas are usually used for gas. The difference is in the higher density of the liquid oxidizer, and the fact that higher velocities are permitted before chocking conditions. In this case, the ratio between gaseous and liquid density at same temperature and pressure is used as a multiplication coefficient (eq.3.6).

$$S_{g,gas} = S_g \frac{\rho_{gas}}{\rho_{liquid}} \tag{3.6}$$

In our case, the fluid is N_2O, so liquid properties are extrapolated by NIST data [2] while the gas phase is treated by ideal gas equation.

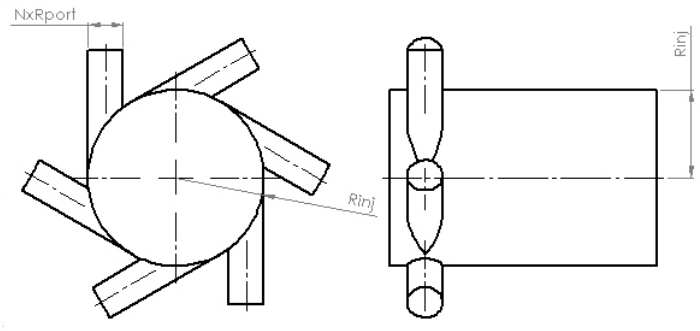

(a) Tangential channels

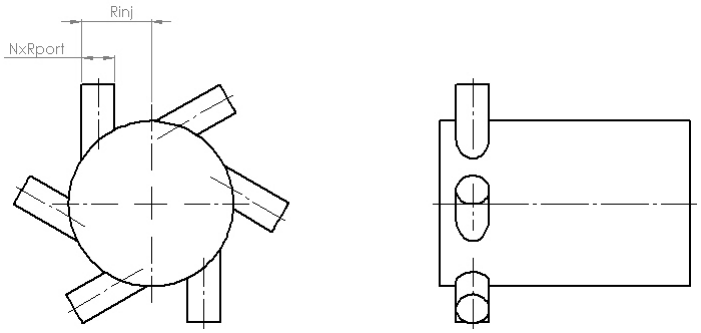

(b) Inner channels

Figure 3.4: Swirl geometry

Table 3.1: Geometrical swirl number data

Number of channels		6
Injection channels diameter [mm]		1.2
Injector diameter to grain [mm]		25
Actual ϕ_{inj} [mm]		21.2
S_g	**Tangential**	**Real**
Classical	68.9	43.5
Gaseous correction	5.4	3.8

3.1.3 Test matrix

First purpose of this CFD work is to understand which are the main parameters influencing the swirl fluid field. With this in mind, a set of simulation has been solved and analyzed adding one "ingredient" after each other to achieve a complete burning:

1. cold: only oxidizer is injected in chamber;

2. blowing: both fuel and oxidizer are injected, but no chemical reactions are given;

3. hot: complete combustion;

4. nozzle: complete combustion, nozzle expand the gas after the chamber

5. axial: comparative case, same as before but change the injection.

In the first 3 cases, geometry is without nozzle (expansion zone in fig.3.1.1), which is present in case 4 and 5. In place of nozzle, an opening condition with fixed pressure permits the fluid to exit the motor chamber.

As a preview of the results further explained, this helped us to understand that there is a straightening of the vortex lines due mostly to the combustion process that according to continuity equation accelerate the fluid in the axial direction. This point is very important to understand: the velocity vector is not turned by an external force (same magnitude, change only in angle), but there is only one component growth that straighten the trajectory of the fluid particles.

Other further works (see chap.4.1) consists in understanding what happen if:

1. mass flow is reduced (throttling);

2. grain diameter is larger (different time during burn);

3. particular devices are inside the combustion chamber (use of mixer, post/pre-chambers).

All base dimensions are derived from experimental data and are summarized in tab.3.2.

Table 3.2: CFD setup basic data

Variable	Unit	Value
Oxidizer mass flow	kg/s	0.35
Oxidizer inlet temperature	K	298
O / F ratio	-	3.9
Fuel mass flow	kg/s	0.09
Fuel inlet temperature	K	725
Grain length	mm	145
Grain port diameter	mm	25
N. holes	-	6
Holes diameter	mm	1.2
Injection to fuel port	mm	25
Nozzle throat	mm	16
Nozzle exit	mm	29
Outlet pressure	bar	1
Opening pressure	bar	30

3.2 Vortex behaviour

In this part we want to give a physical description of the main important parameters inside combustion chamber that influence the fluid field.

Five simulations will be discussed (described in 3.1.3):

1. cold;
2. blowing;
3. hot;
4. nozzle;
5. axial.

In summary, cases from 1 to 3 are without the nozzle. In its place, a continuation of the grain with wall condition for 30mm is comprised in the geometry.

First, let's have a qualitative description of the flow field in the combustion chamber, looking at fig.3.5. The fluid is injected in the chamber with a fully tangential direction respect to the motor main axis. As it goes on, tends to straighten,

due to an acceleration in the axial direction imposed by the temperature rise due to combustion.

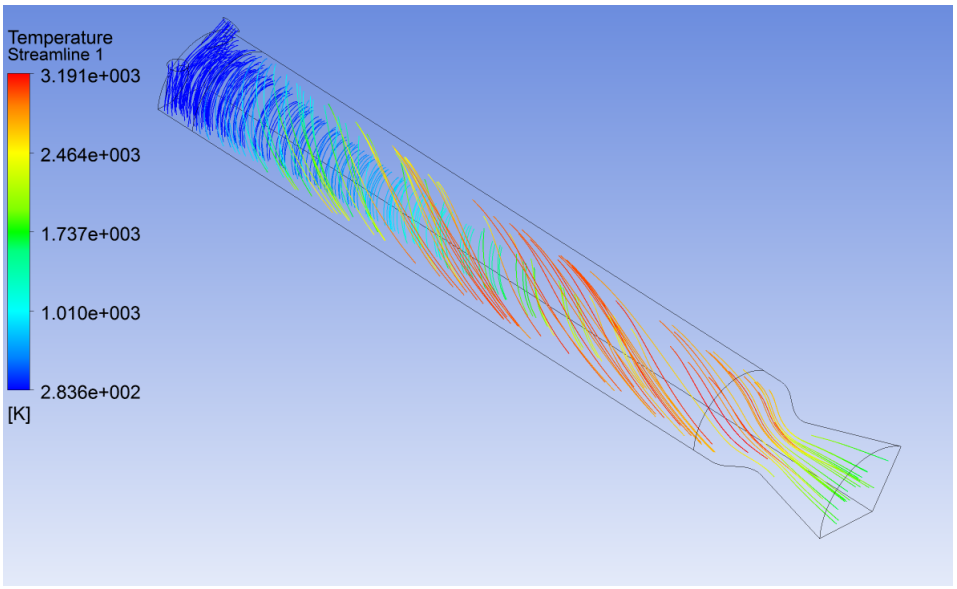

Figure 3.5: Fluid streamlines inside combustion chamber with vortex injection

The vortex flow field can be divided in three distinct parts (see fig.3.6):

1. impingement: near the injection the flow is not fully stabilized, the oxidizer is ejected from the holes and strikes the chamber surfaces; then it is bended and follows the curvature of the grain; backflow is present;

2. vortex: in the grain zone, the motion is stabilized, the fluid follows an helical path; the swirl angle tends to be straightened by various forces (discussed later);

3. nozzle:near the exit (nozzle or opening) the swirl angle sharply decreases.

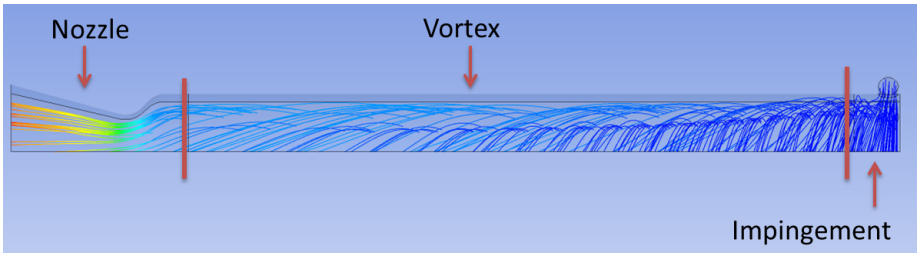

Figure 3.6: Vortex flowfield description

Will be clear later that the fact that the vortex tends to straighten is not due to the nozzle, but mainly to the combustion process that accelerate the axial

component of the flow due to continuity equation to be respected.
In the first region the flow is not fully developed and tumble within itself; in case (like this) of fully tangential injection this region is very narrow, but when an axial component is added to the flow it is more clear and can induce to phenomenon like greater erosion of the grain respect to the combustion chamber [7].

On the contrary, in classical showerhead injection (axial), the streamlines are straight in all the fluid field (see fig.3.7).

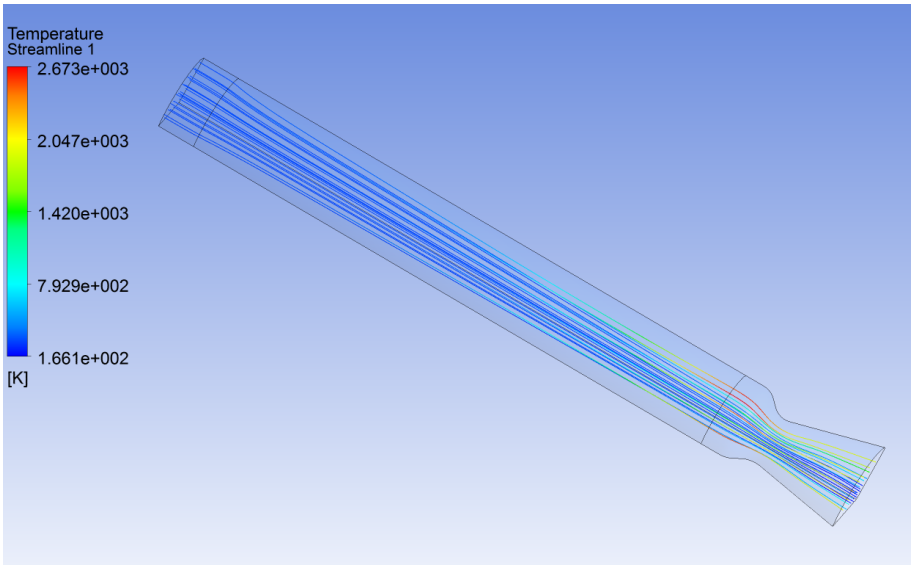

Figure 3.7: Axial injection streamlines

Another comparison regarding streamlines is the undesired but still present tangential and axial component of velocity after the nozzle throat. In both (axial and vortex) cases, with a conical shape nozzle, the phenomenon is evident, but with different peculiarities: while in axial injection only the radial component affect the thrust, in vortex case there is also a tangential component (fig.3.8). The reduction of thrust, however, is evaluated in no more that 2% in both cases.

From experiments it is clear that the regression rate with vortex injection is higher (depending on geometry, from 86% [8] and more). One possible explanation is in fig.3.9. In this picture are plotted temperature and N_2O mass fraction in both case of injection (take care that scales are not the same). In axial injection the combustion process happens in a very narrow region, while in vortex case the flame is more diffuse. The reason is the higher turbulence in combustion chamber generated by the vortex flow field.
The vortex injection enables a more diffuse flame, enhancing the mixing of the reactants in the combustion chamber. As a consequence, the burn process is more

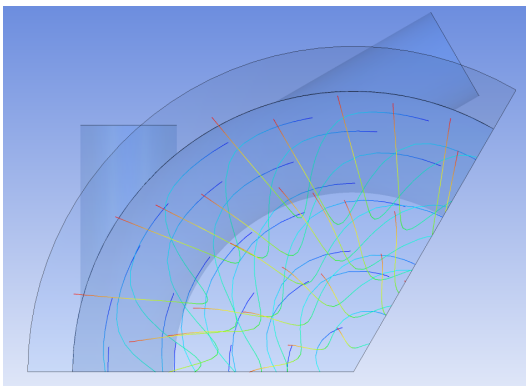

(a) Nozzle streamlines in vortex injection - back view

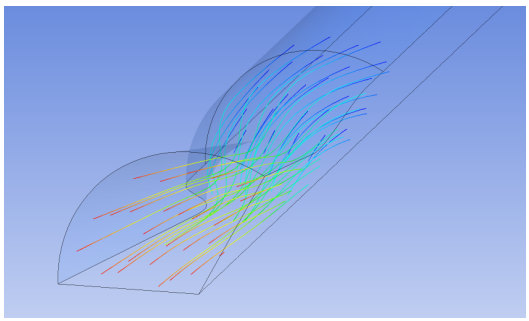

(b) Nozzle streamlines in vortex injection - side view

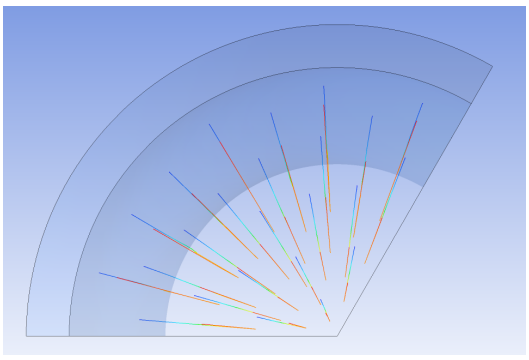

(c) Nozzle streamlines in axial injection - back view

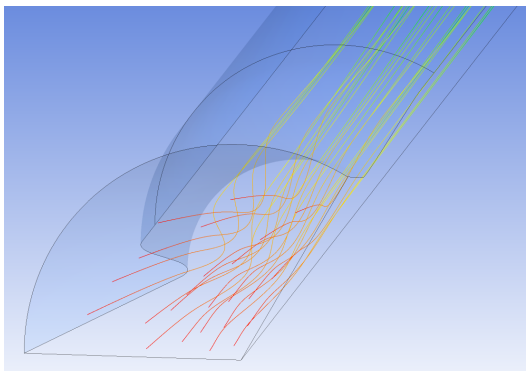

(d) Nozzle streamlines in axial injection - side view

Figure 3.8: Residual velocity (radial and tangential) after nozzle throat - fluid field streamlines

effective, increasing the efficiency of the rocket. It is important to remark that in this thesis the term flame refers to the region where hot combustion products are present. The zone where the combustion takes place is on the contrary very thin and located near the walls.
The faster is the fluid entering the chamber (high speed means low orifice diameter), the more this effect is enhanced. It has to be noticed, however, that this simulation has the simplification of gaseous injection, and doesn't take into account phenomena like cavitation and evaporation, typical of nitrous oxide.

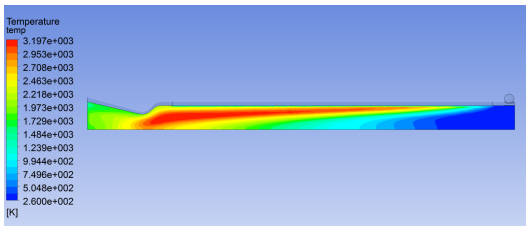

(a) Temperature plot, vortex injection

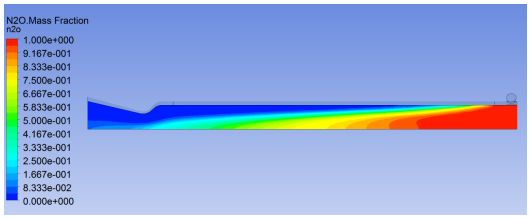

(b) N_2O mass fraction plot, vortex injection

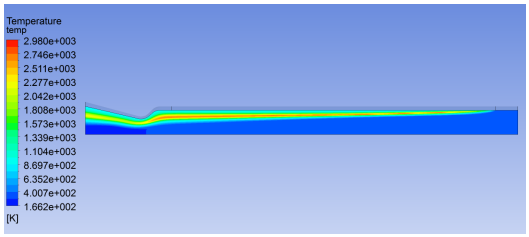

(c) Temperature plot, axial injection

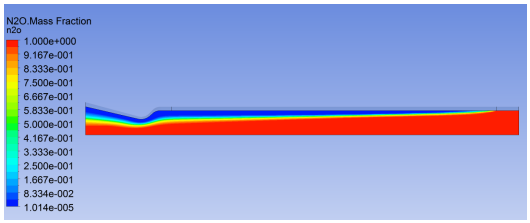

(d) N_2O mass fraction plot, axial injection

Figure 3.9: Flame diffusion in axial and vortex injection

The velocity (see fig.3.10), furthermore, enhance not only the combustion process, but also the entrainment of the paraffin wax liquid droplets, a particular effect that only this kind of fuel exhibit [17] with an oxidizer injected in turbulent regime. This is an important thing to take into account when throttling down the motor reducing mass flow (and then oxidizer speed). In those plots, speed is upper-limited to 500m/s to have a clear view of what happens inside the combustion chamber.

In fig.3.10(c) there is a peak in the nozzle throat because the regime is that of forced vortex flow (see chap.3.3). It can be seen that the axial velocity profile in both cases follows the temperature profile, leading to higher speed in vortex case.

To continue in our analysis, lines in the fluid geometry must be placed, in order to analyse the fluid behaviour in the combustion chamber. In particular (see fig.3.11) 7 axial lines (with distance from motor axis from 0mm to 12mm at step

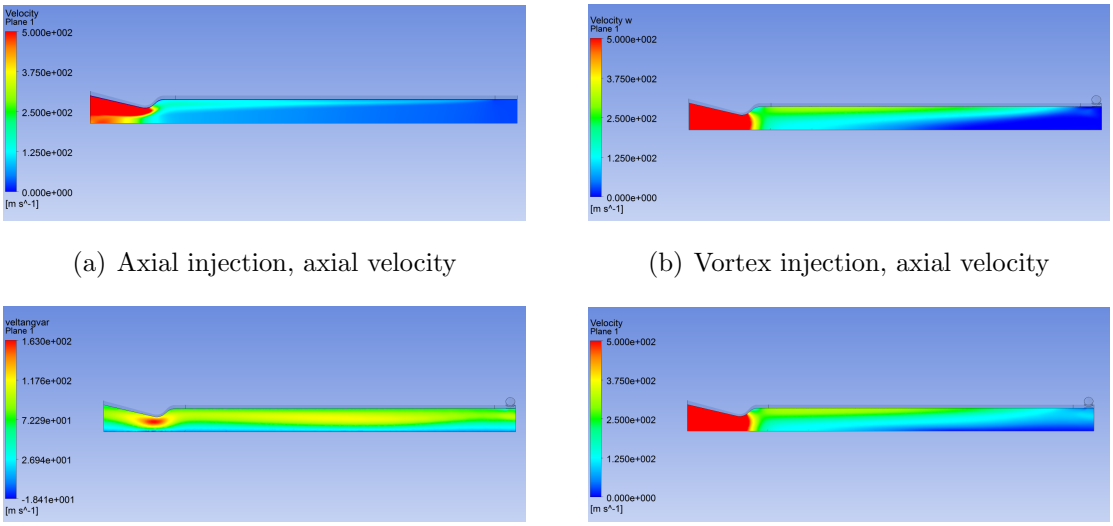

(a) Axial injection, axial velocity

(b) Vortex injection, axial velocity

(c) Vortex injection, tangential velocity

(d) Vortex injection, total velocity

Figure 3.10: Axial and vortex velocities comparison

of 2mm) and 5 radial lines (with distance from grain start from 30mm to 150mm) have been defined.

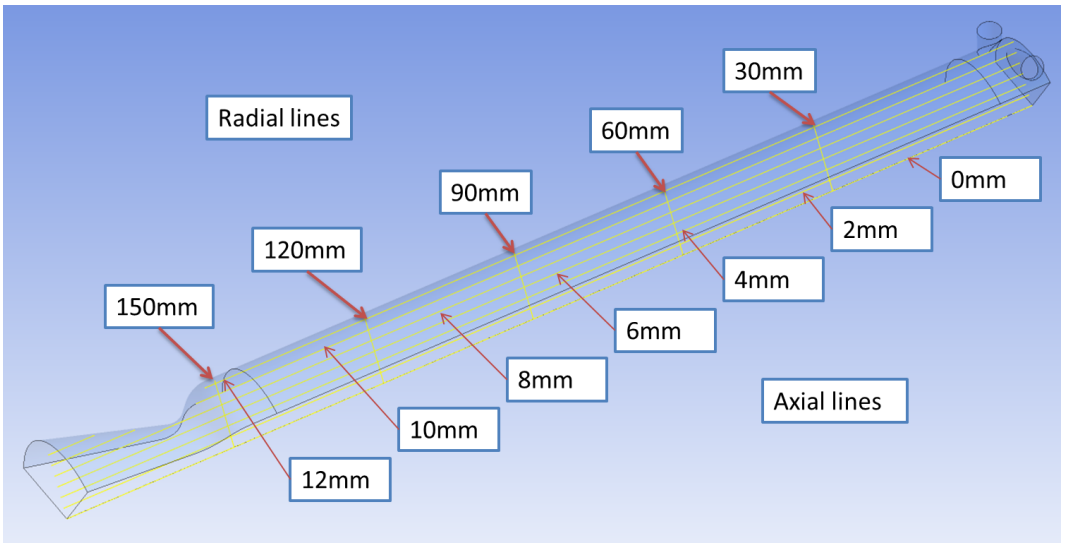

Figure 3.11: Plot lines definition in fluid geometry

Axial line at 0mm is not very useful and not often used, because it is in a boundary zone (axis of symmetry). A similar thing happens at axial line placed at 12mm from the axis of the motor (remember that the grain internal diameter is 25mm). Radial line at 150mm from the grain, instead, is influenced from nozzle (it's outside the grain, which length is 145mm) and here too variable differ from inside combustion chamber, especially velocities.

In the following (fig.3.17), the Z coordinate is the distance from the beginning (near injection) of the grain, while R is the radial coordinate, with origin in the axis of the motor. Geometry is depicted in fig. 3.11, simulated with combustion.

The flame diffusion can be observed watching at fig.3.12, where temperature profiles are plotted in radial lines, comparing both injection types.

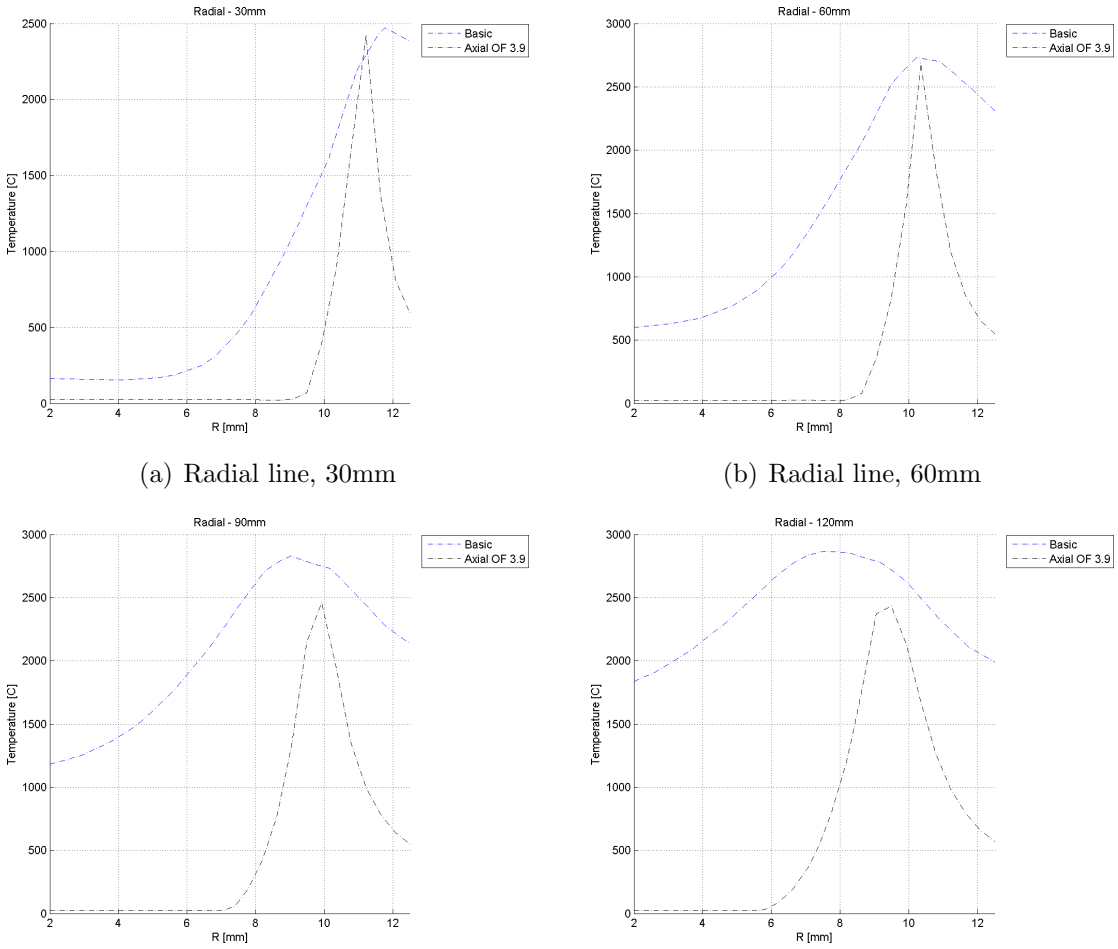

(a) Radial line, 30mm

(b) Radial line, 60mm

(c) Radial line, 90mm

(d) Radial line, 120mm

Figure 3.12: Axial and vortex velocities comparison

In axial injection, temperature gradient is very sharp, while in vortex the higher temperature zone is wider.

A typical effect of vortex injection is a backflow in the impingement region [8] (fig.3.13).

As can be seen, there is a pressure gradient (lower pressure near the motor axis, fig.3.13(d)) near the injection, due to the high angular velocity of the fluid imposed by this kind of injection. This gradient is both radial and axial, so fluid from the middle of combustion chamber is drawn to the injection zone (see fig.3.19(c) and

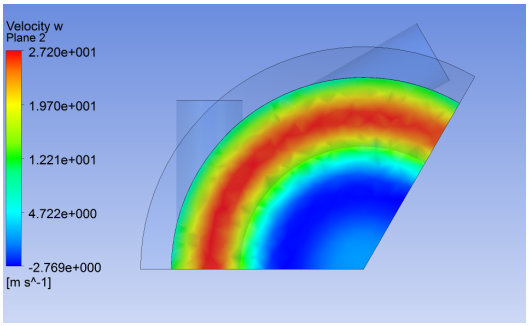

(a) Axial velocity contour plot

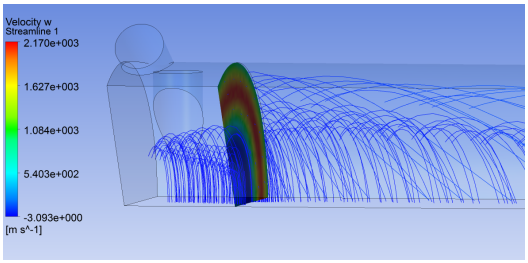

(b) Streamlines (only forword) from reference plane

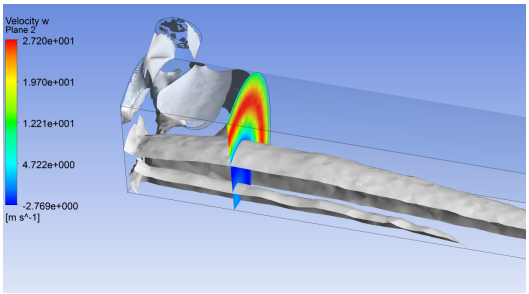

(c) Isosurface of null axial velocity: detail on injection region

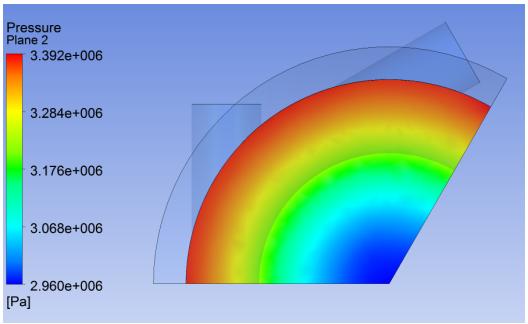

(d) Pressure profile contour plot

Figure 3.13: Vortex injection backflow - reference plane is at 1cm from injection

3.19(d)).

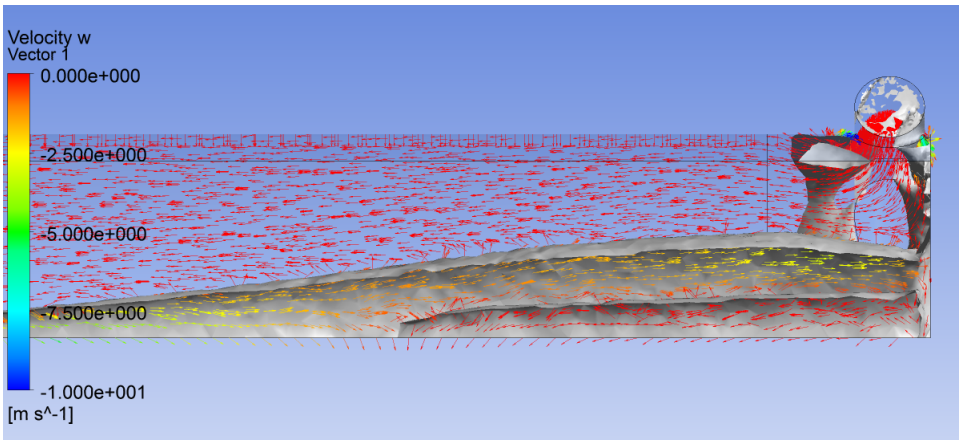

Figure 3.14: Vector plot of velocities (color is axial velocity)

The phenomenon is more evident in fig.3.14 where velocity vectors are plotted in a mid-plane, together with an isosurface of null axial velocity.

It can be seen that in all combustion chamber (remember, chamber ends at 145mm) radial velocity (fig.3.21(a) and 3.21(b)) is negligible respect to axial (fig.3.17(c) and 3.17(d)) and tangential (fig.3.17(a) and 3.17(b)). This will be used later in analytical consideration in chap.3.3.

From 3.17(a) (radial lines) it can be noticed that tangential velocity from center to outside is linear (meaning a forced vortex) in the first part, then reduce its value to adapt to the boundary condition imposed by the fuel mass flux and wall with no slip.

In fig.3.19(c) and 3.19(d), pressure has a higher variation from center (motor axis) to outer (grain surface) near the injection that near the nozzle. The explanation is in the temperature and composition of the interested section.
As will be explained in chap.3.3, pressure gradient, given the same angular velocity, is higher when the fluid is cooler (where oxidizer in injected) because of higher density or when the molar mass is higher, because of inertial forces. This is of extreme interest when measuring pressure in combustion chamber, to help in the choice of the pick-up point. If one choose the post-chamber, pressure will be more homogeneous and the error committed will be lower.

In fig.3.18 this effect can be observed: going from injection to nozzle the mean temperature is higher, and the pressure gradient is calmed down.

Fig.3.19 further improve what already said about pressure gradient. At the beginning of the grain, the main element is nitrous oxide, with molar mass of

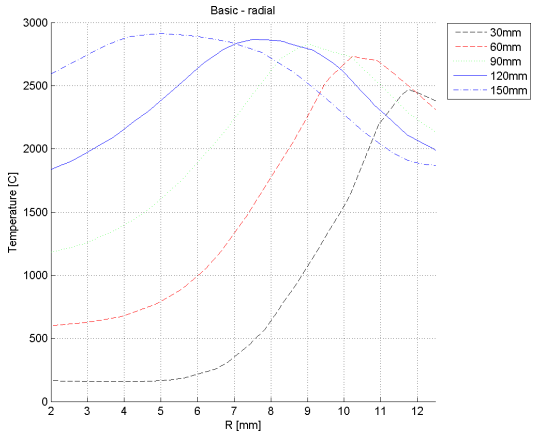

(a) Temperature profile - radial lines

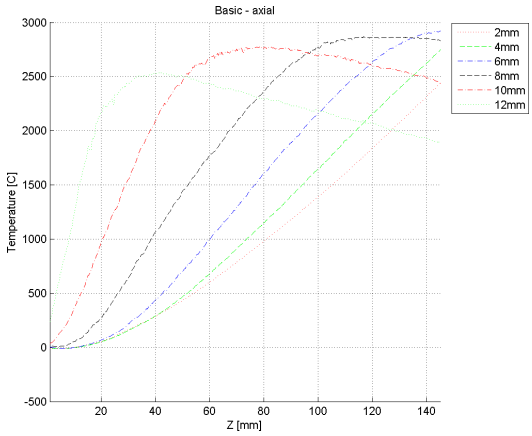

(b) Temperature profile - axial lines

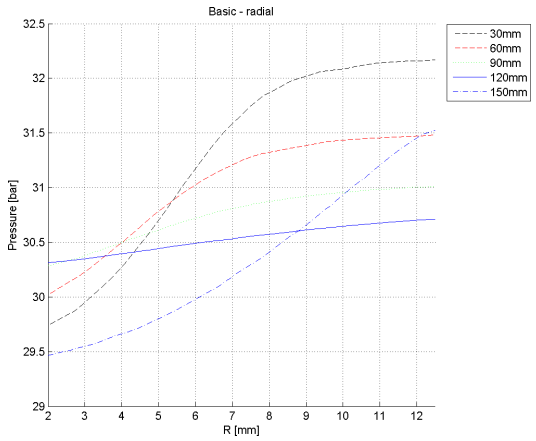

(c) Pressure profile - radial lines

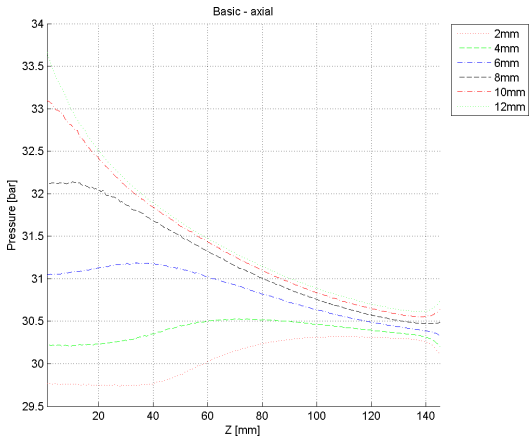

(d) Pressure profile - axial lines

Figure 3.15: Temperature, pressure and swirl angle (90° means axial) in CFD analysis

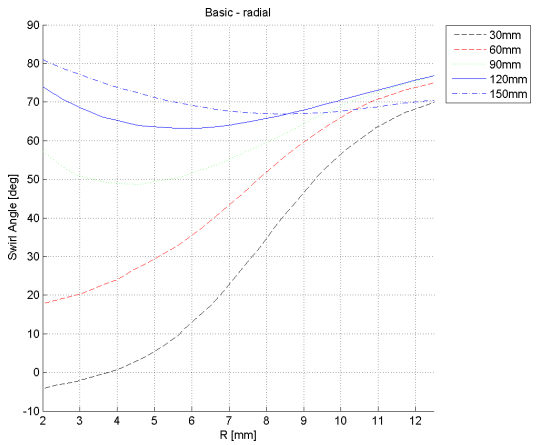

(a) Swirl angle - radial lines

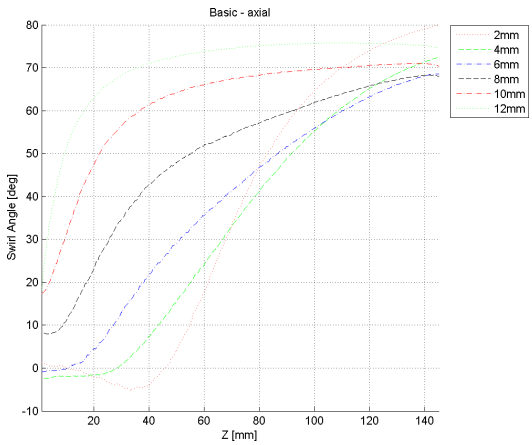

(b) Swirl angle - axial lines

Figure 3.16: Temperature, pressure and swirl angle (90° means axial) in CFD analysis

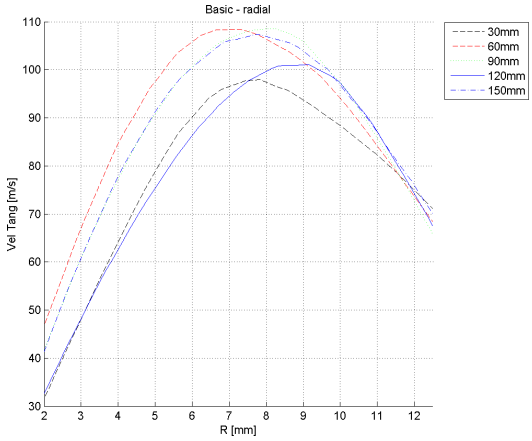

(a) Tangential velocity - radial lines

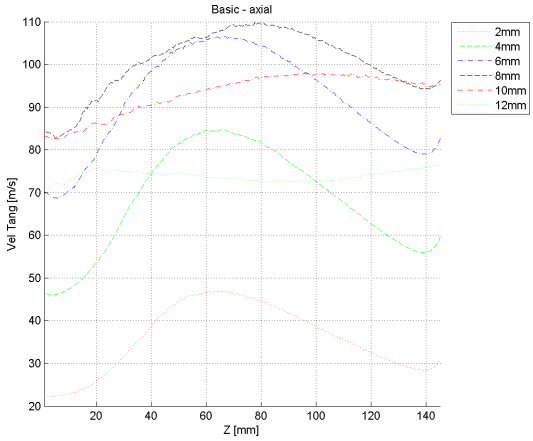

(b) Tangential velocity - axial lines

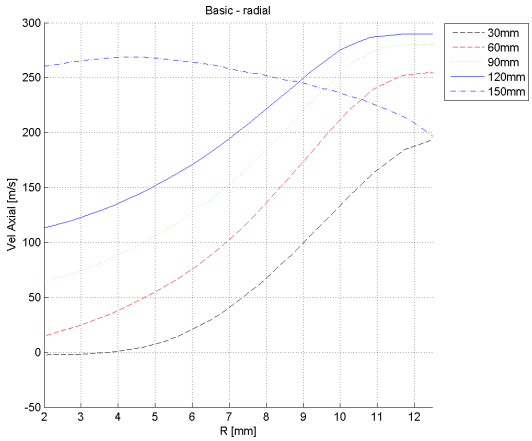

(c) Axial velocity - radial lines

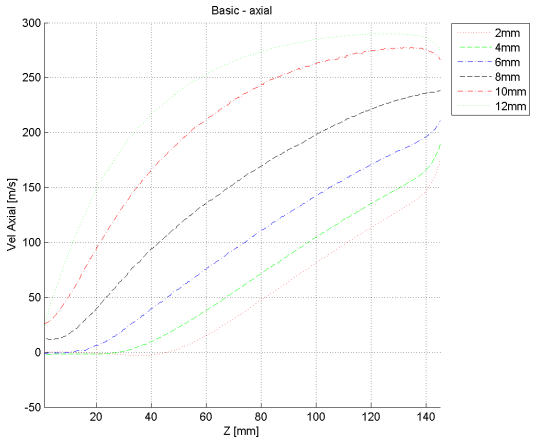

(d) Axial velocity - axial lines

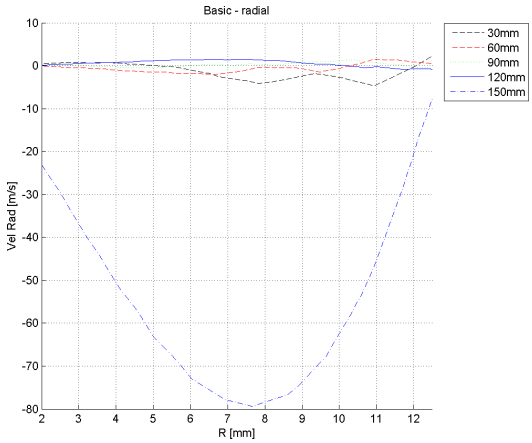

(e) Radial velocity - radial lines

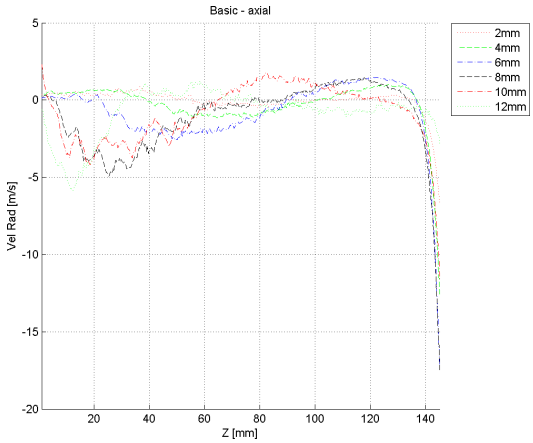

(f) Radial velocity - axial lines

Figure 3.17: Velocity profiles in CFD analysis

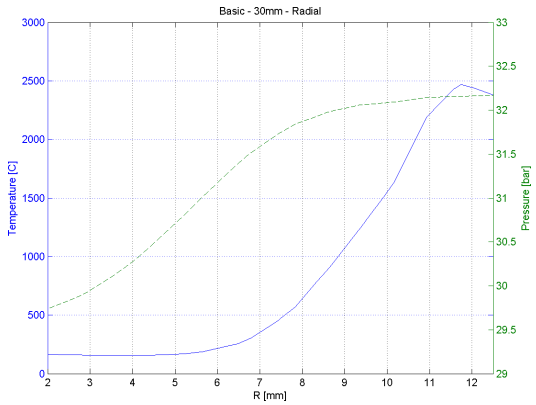

(a) Radial 30mm

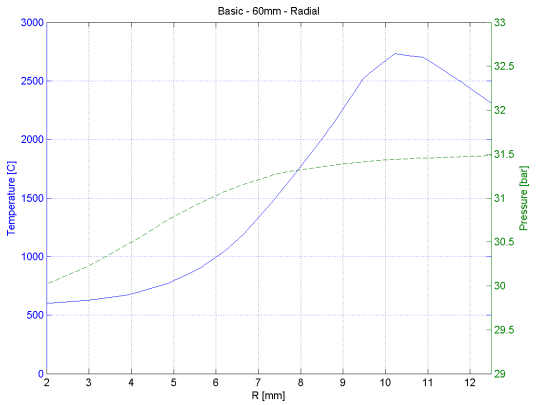

(b) Radial 60mm

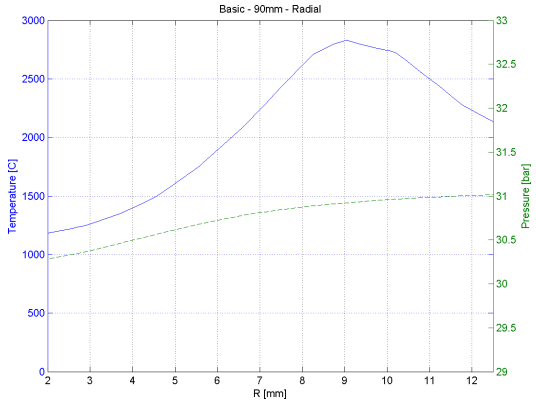

(c) Radial 90mm

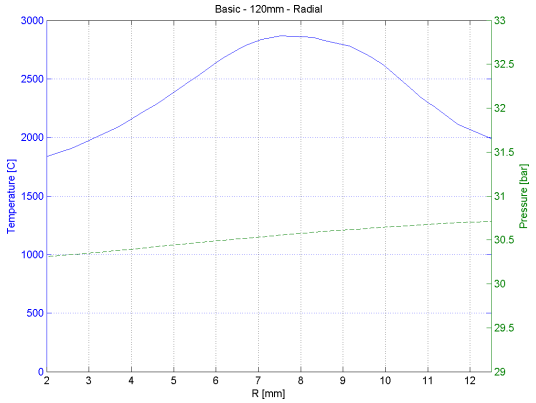

(d) Radial 120mm

Figure 3.18: Comparison of pressure and temperature in radial lines

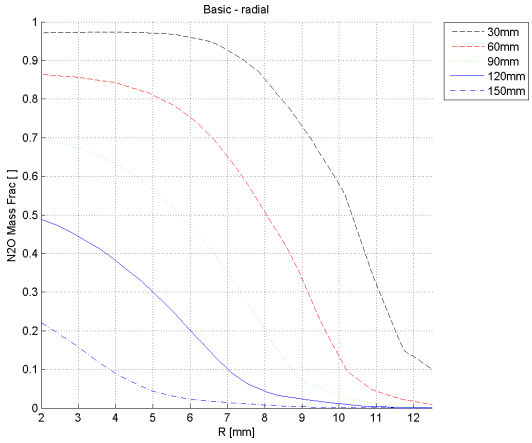

(a) N_2O profile - radial lines

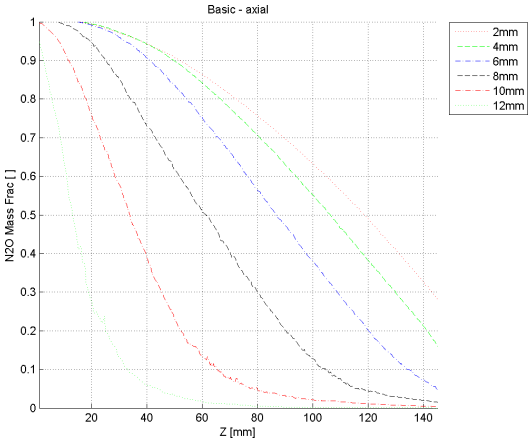

(b) N_2O profile - axial lines

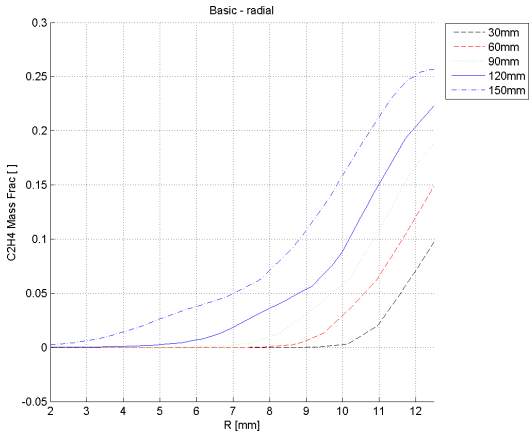

(c) C_2H_4 profile - radial lines

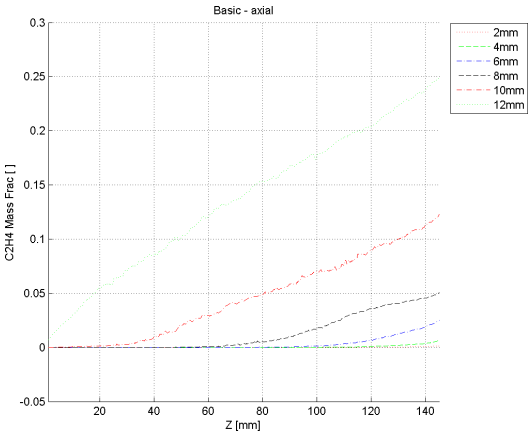

(d) C_2H_4 profile - axial lines

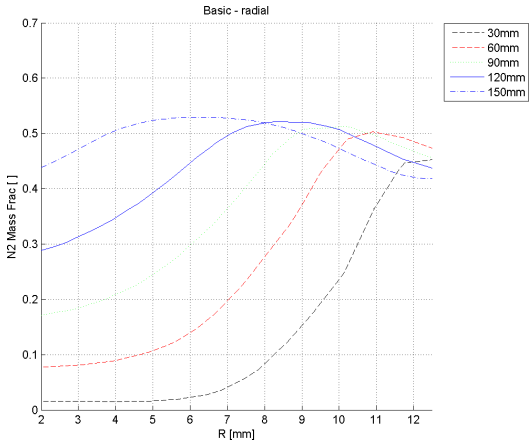

(e) N_2 profile - radial lines

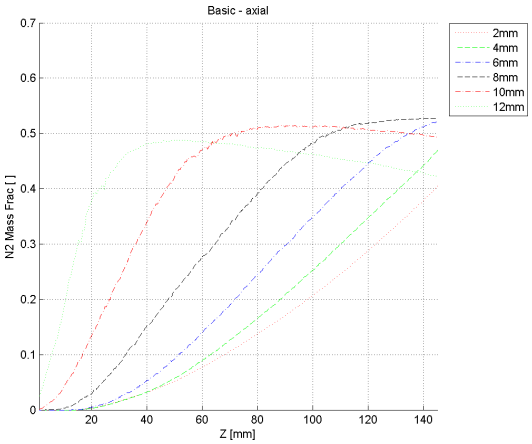

(f) N_2 profile - axial lines

Figure 3.19: Combustion reactants (N_2O - C_2H_4) and products (N_2) in CFD analysis

44g/mol. At the end there is a much higher quantity of product of the reaction (N_2 is representative for all of them, see fig.3.3), with a mean molar mass of 28g/mol.

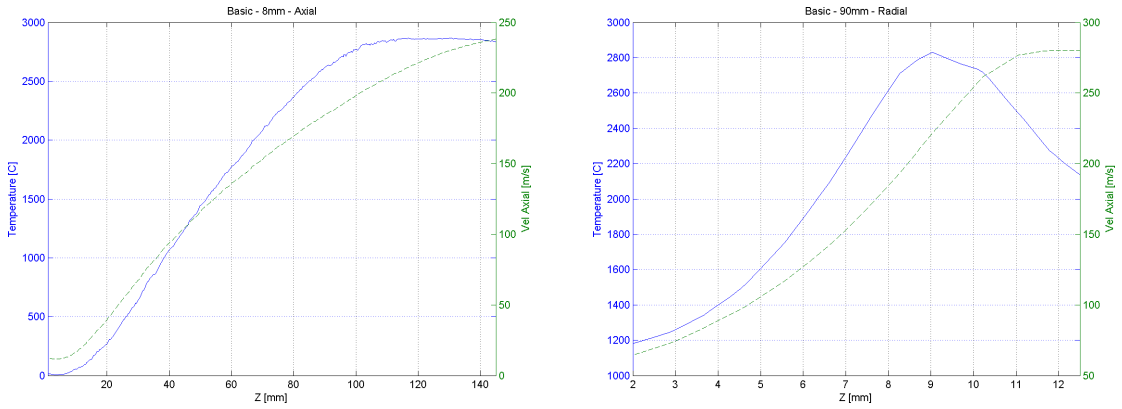

(a) Axial line - 8mm from axis (b) Radial line - 90mm from grain start

Figure 3.20: Comparison of temperature and axial velocity in CFD analysis

Looking at axial velocity in radial coordinates, and taking in mind the temperature profile in fig.3.9(a), we can see that there is a linear link between the two variables. This appear evident looking at fig.3.20, where temperature and axial velocity are compared in radial (90mm from grain start) and axial (8mm from motor axis) lines. The higher the temperature in a point, the higher the axial velocity. This is due to the continuity equation: higher temperature means lower density (at constant pressure), so axial velocity must increase to maintain the same mass flow. This do not happen for tangential velocity (fig.3.21).

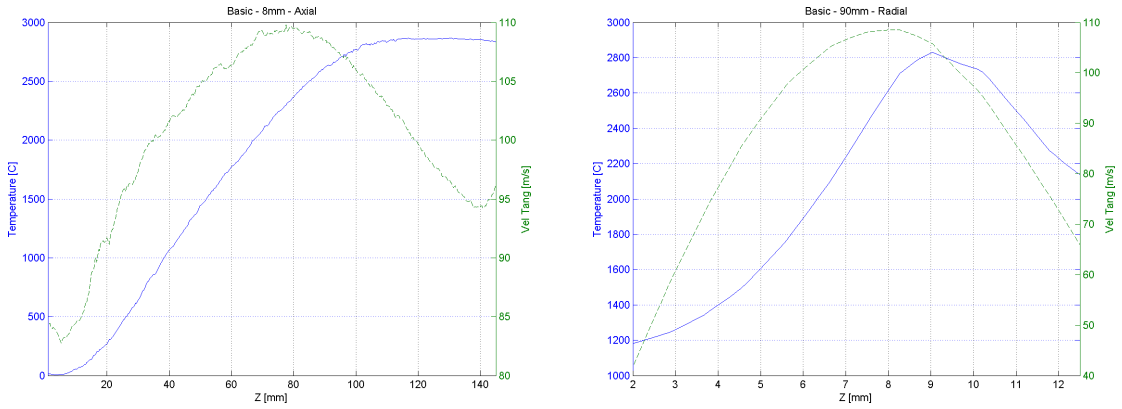

(a) Axial line - 8mm from axis (b) Radial line - 90mm from grain start

Figure 3.21: Comparison of temperature and tangential velocity in CFD analysis

But which are the main parameters that influence the fluid field? First of all, we have to split every possible causes; to do so, as previously said, 4 simulations

have been conducted, "adding an ingredient every time": first, only N_2O have been injected in chamber (*cold* case), then also paraffin fuel (*blowing* case) but without combustion. Both these simulation have been conducted in a geometry without nozzle. Last two simulations have been performet with all species injected, and chemical reactions activated. The first (*hot* case) is again without nozzle, while the last (*nozzle* or *basic* case) is the one seen and described up to now.
First, we'll compare streamlines in fig.3.22. It can be observed that *cold* and *blowing* cases are qualitatively similar; same thing can be said for *hot* and *nozzle* cases. The main difference between these two groups is that when combustion is active, there is a straightening in fluid lines in combustion chamber.

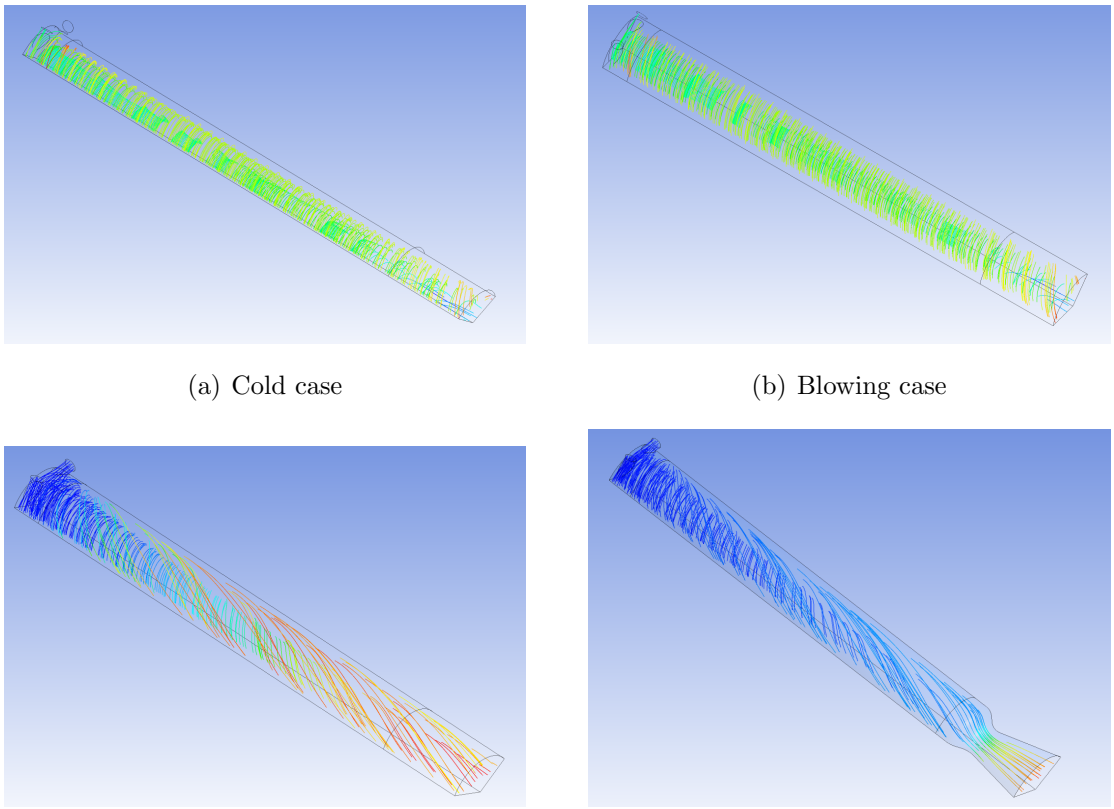

(a) Cold case

(b) Blowing case

(c) Hot case

(d) Nozzle case

Figure 3.22: Streamlines in combustion chamber, vortex injection

From fig.3.25 to fig.3.28 all four cases are compared. Two lines have been taken as reference, the axial at 8mm from motor axis and the radial at 90mm from grain start.
Results show quantitatively what streamlines announced: there is a clear difference in case with and without combustion. Axial velocity is almost constant for no combustion cases, while in the others there is a net acceleration. The result is

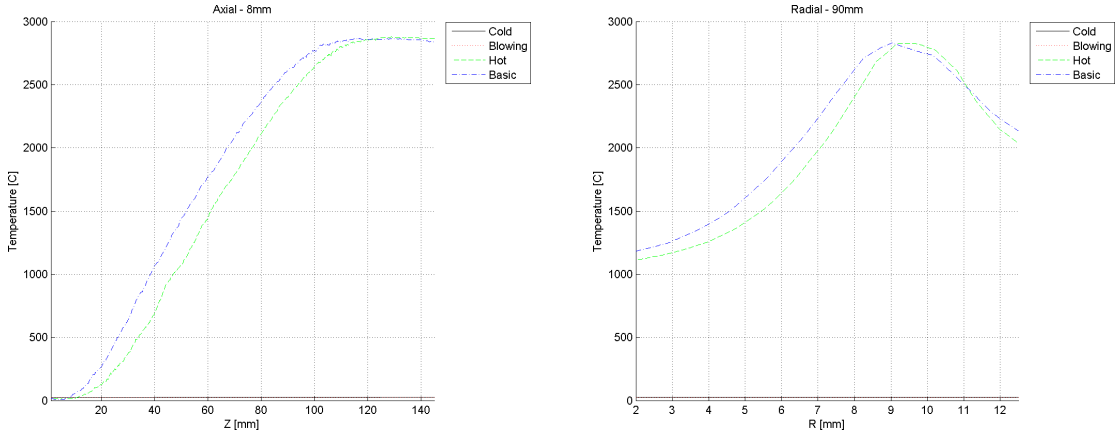

(a) Axial line at 8mm from motor axis (b) Radial line at 90mm from grain start

Figure 3.23: Temperature comparison in cases *cold*, *blowing*, *hot* and *nozzle*

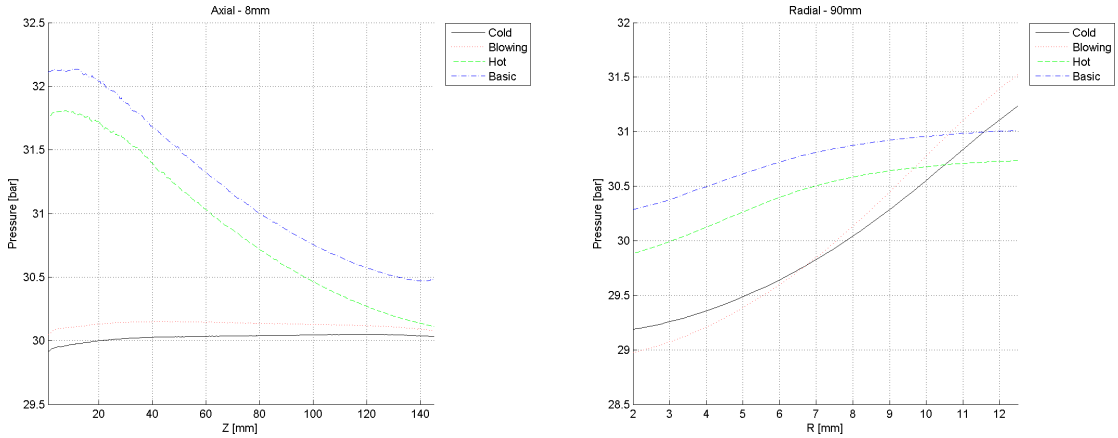

(a) Axial line at 8mm from motor axis (b) Radial line at 90mm from grain start

Figure 3.24: Pressure comparison in cases *cold*, *blowing*, *hot* and *nozzle*

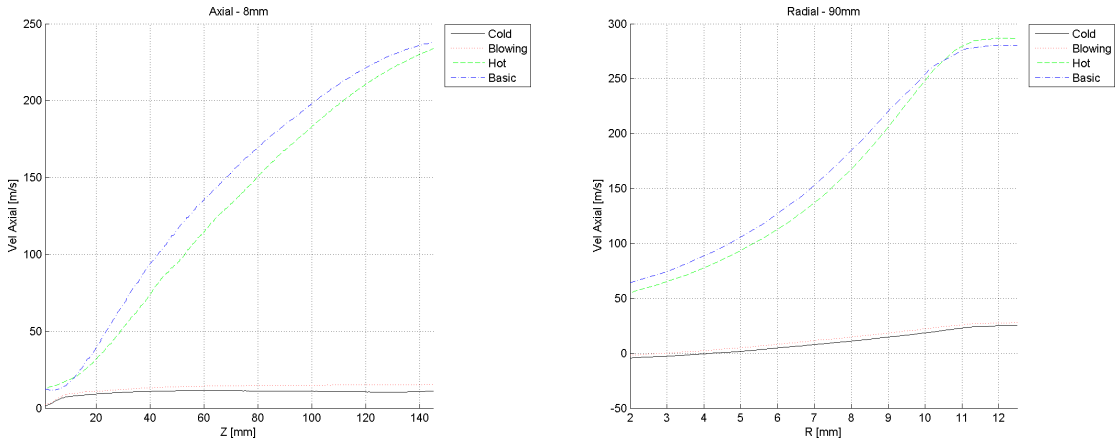

(a) Axial line at 8mm from motor axis (b) Radial line at 90mm from grain start

Figure 3.25: Axial velocity comparison in cases *cold*, *blowing*, *hot* and *nozzle*

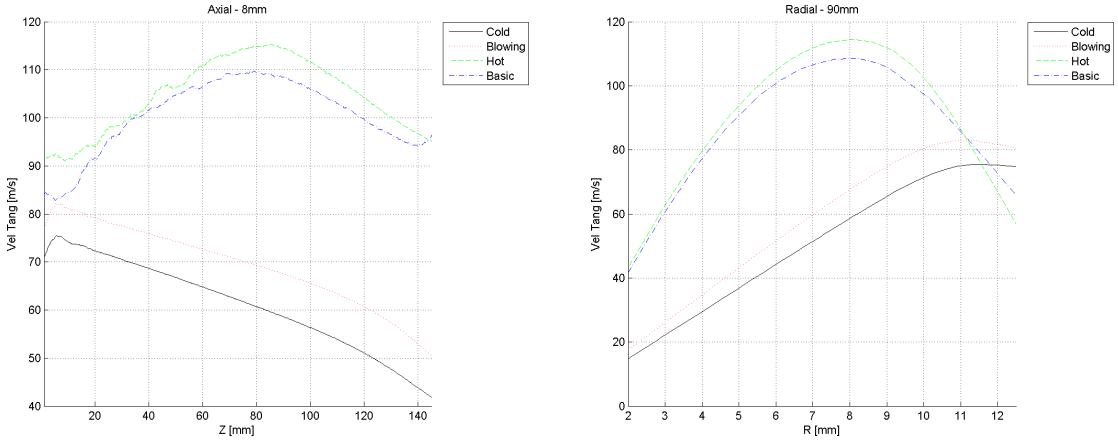

(a) Axial line at 8mm from motor axis (b) Radial line at 90mm from grain start

Figure 3.26: Tangential velocity comparison in cases *cold*, *blowing*, *hot* and *nozzle*

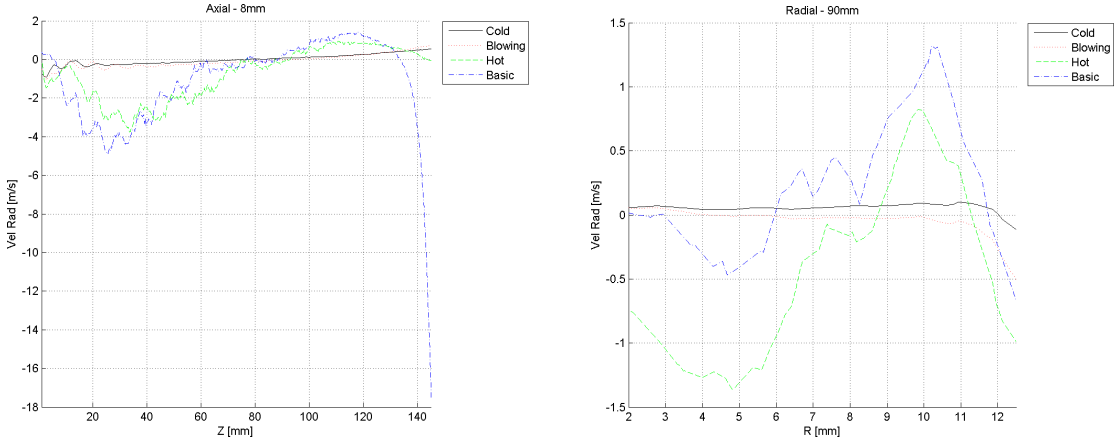

(a) Axial line at 8mm from motor axis (b) Radial line at 90mm from grain start

Figure 3.27: Radial velocity comparison in cases *cold*, *blowing*, *hot* and *nozzle*

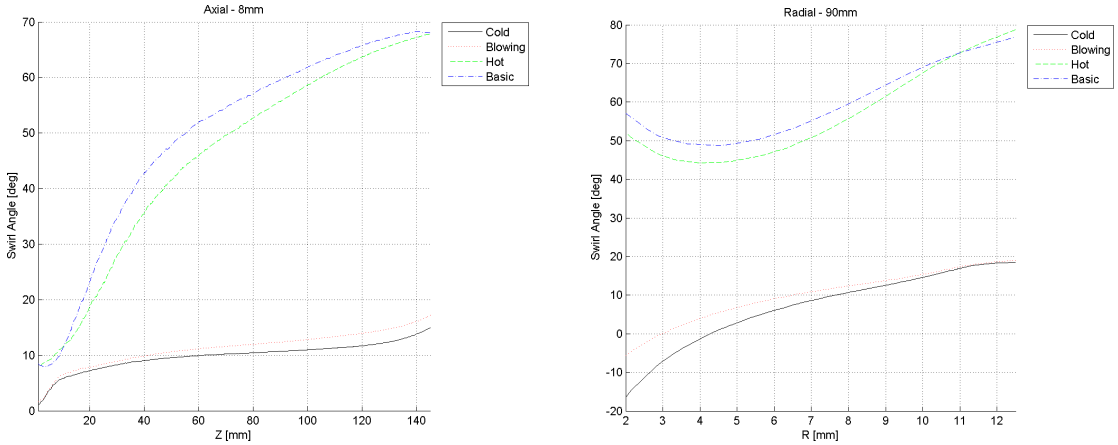

(a) Axial line at 8mm from motor axis (b) Radial line at 90mm from grain start

Figure 3.28: Swirl angle comparison in cases *cold*, *blowing*, *hot* and *nozzle*

an increasing swirl angle (remember, 90° mean purely axial flow, 0° means purely tangential).
Also pressure has a similar trend, showing a higher pressure in the near-injection region whit combustion; on the contrary, a flat profile is observed in *cold* and *blowing* cases. This is due to the high angular velocity and temperature increase: we'll see later that a lower temperature, given the same angular velocity, give a higher pressure gradient in radial coordinate. Again, radial velocity is negligible (one order of magnitude lower) respect to axial and tangential.

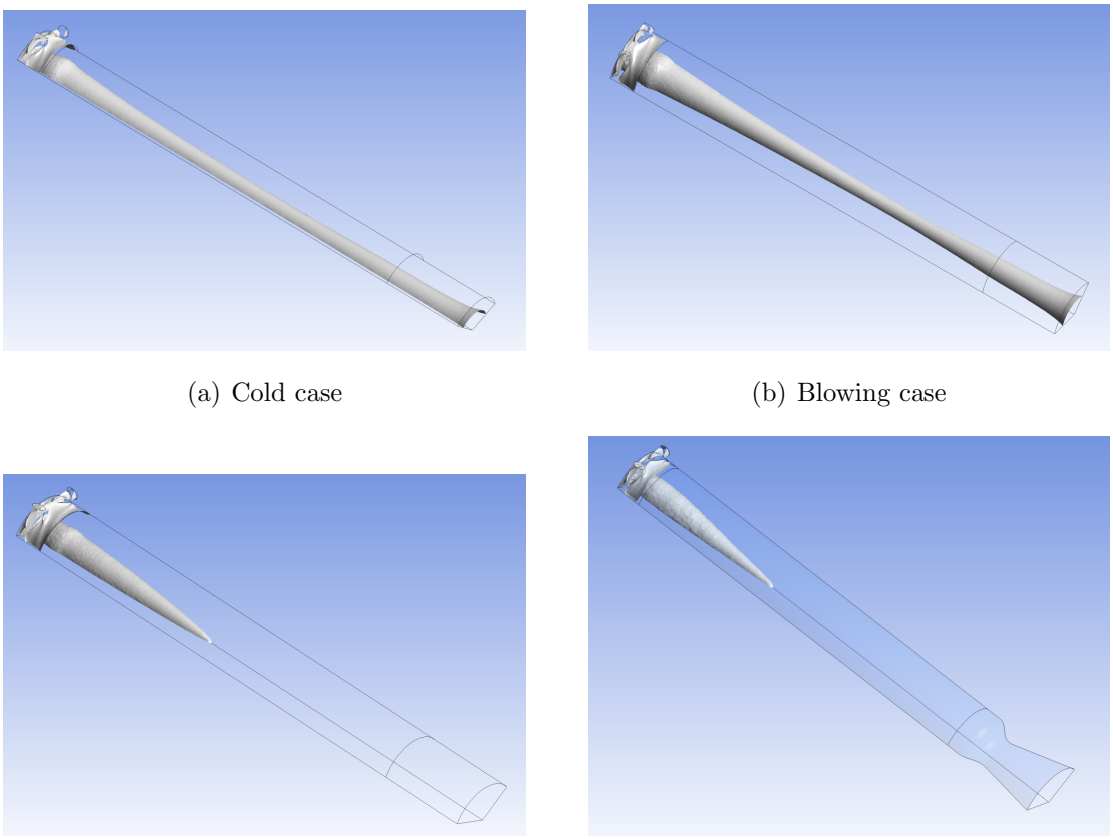

(a) Cold case

(b) Blowing case

(c) Hot case

(d) Nozzle case

Figure 3.29: Isosurface (null axial velocity) in combustion chamber, vortex injection

In fig.3.29 are showed isosurfaces of null axial velocity inside combustion chamber for all cases. It can be seen that when combustion doesn't take place (that means, no axial acceleration and no swirl angle variation) the reverse flow continue up to the end of the fluid volume.

In summary, we can say that going from axial to vortex injection there is an increment of turbulence in the combustion chamber, and this enhance the combustion

efficiency. The added tangential velocity permits an higher thermal flux toward the grain surface, and this increase the melted paraffin and thus the regression rate.

3.3 Analytical model

Some important considerations can be done in the vortex fluid flow using compressible Navier-Stokes equations, neglecting the gravity and normal viscous terms. In cylindrical coordinates, balance in tangential direction is the following:

$$\begin{gathered}\rho\left(\frac{\partial u_\theta}{\partial t}+u_r\frac{\partial u_\theta}{\partial r}+\frac{u_\theta}{r}\frac{\partial u_\theta}{\partial \theta}+u_z\frac{\partial u_\theta}{\partial z}+\frac{u_r u_\theta}{r}\right)= \\ -\frac{1}{r}\frac{\partial p}{\partial \theta}+\mu\left[\frac{1}{r}\frac{\partial}{\partial r}\left(r\frac{\partial u_\theta}{\partial r}\right)+\frac{1}{r^2}\frac{\partial^2 u_\theta}{\partial \theta^2}+\frac{\partial^2 u_\theta}{\partial z^2}-\frac{u_\theta}{r^2}+\frac{2}{r^2}\frac{\partial u_r}{\partial \theta}\right]\end{gathered} \tag{3.7}$$

Some simplifications can be introduced based on the following assumptions:

- steady state flow - null time derivative;
- axis-symmetry - null derivative over the tangential direction;
- variation of tangential velocity in z can be neglected;
- radial velocity is low compared to axial and tangential (and thus is neglected).

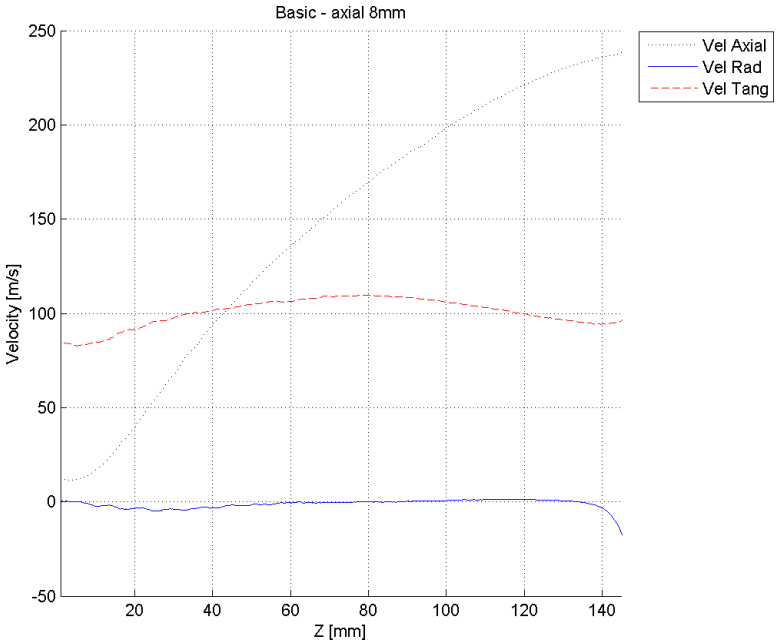

Figure 3.30: Velocity comparison in axial line at 8mm from motor axis - *nozzle* case

These last two assumptions have been validated through CFD simulations. In particular, in fig.3.30 it is proved that the radial component is negligible, while tangential component has a very flat behaviour compared to axial.

Equation 3.7 becomes:

$$\frac{1}{r}\frac{\partial}{\partial r}\left(r\frac{\partial u_\theta}{\partial r}\right) - \frac{u_\theta}{r^2} = 0 \tag{3.8}$$

The only possible solution (excluded trivials) for the flow field is the forced vortex:

$$\omega r = u_\theta \tag{3.9}$$

where ω means the angular velocity of the vortex fluid lines and r is the distance from motor axis. It can be seen from CFD (fig.3.26, where for the nozzle case the velocity is scaled according to chamber pressure), proving the theory, that there is no sliding (same angular velocity) between different radial position. This is mathematically true when only oxidizer is injected, but is empirically valid also for the other cases, taking into account the effect of the borders of the grain.

In particular, it can be seen that the change in tangential velocity is due to:

- friction with chamber walls in cold case;
- friction with fuel flow in blowing case (this is less effective, as suggested by the example of the no-friction table with air films);
- flame in *hot* and *nozzle* cases.

In cylindrical reference frame, balance in radial coordinates gives:

$$\begin{gathered}\rho\left(\frac{\partial u_r}{\partial t} + u_r\frac{\partial u_r}{\partial r} + \frac{u_\theta}{r}\frac{\partial u_r}{\partial \theta} + u_z\frac{\partial u_r}{\partial z} - \frac{u_\theta^2}{r}\right) = \\ -\frac{\partial p}{\partial r} + \mu\left[\frac{1}{r}\frac{\partial u_r}{\partial r} + \frac{1}{r^2}\frac{\partial^2 u_r}{\partial \theta^2} + \frac{\partial^2 u_r}{\partial z^2} - \frac{u_r}{r^2} - \frac{2}{r^2}\frac{\partial u_\theta}{\partial \theta}\right]\end{gathered} \tag{3.10}$$

Applying the same simplification as in the previous equation we get:

$$\rho\frac{u_\theta^2}{r} = \frac{\partial p}{\partial r} \tag{3.11}$$

The hypothesis of ideal gas and forced vortex lead to:

$$\rho\frac{u_\theta^2}{r} = \frac{\partial p}{\partial r} = \frac{\omega^2 r M_m p}{R_u T} \tag{3.12}$$

Introducing the further hypothesis of null chemical and temperature gradient in the radial direction the previous equation can be integrated between the center (r=0 and p=pi) and a radial position r providing:

$$\frac{\omega^2 r^2 M_m}{2R_u T} = ln\left(\frac{p}{p_i}\right) \tag{3.13}$$

$$\frac{\omega^2 r^2 M_m}{2R_u T} = ln\left(\frac{\rho}{\rho_i}\right) \tag{3.14}$$

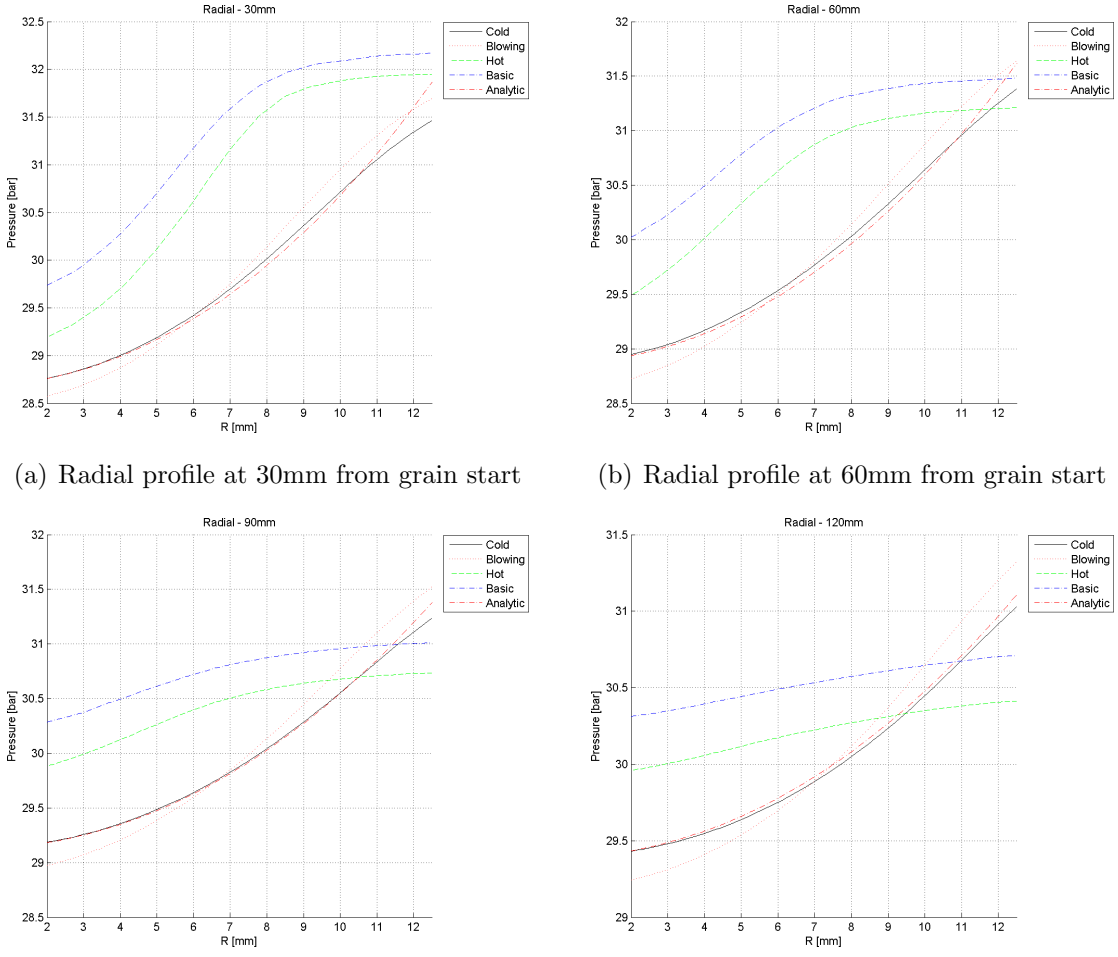

(a) Radial profile at 30mm from grain start

(b) Radial profile at 60mm from grain start

(c) Radial profile at 90mm from grain start

(d) Radial profile at 120mm from grain start

Figure 3.31: Pressure comparison of CFD vs. analytical data

In fig.3.31 is depicted the analytical formula, and compared with CFD data. For each distance from grain start, a different profile has been calculated taking the velocity at 8mm from motor axis using *cold* case for reference value, molar mass of N_2O, mean temperature in the radial direction and pressure *p0* picked in the motor axis.

These equations highlight a centrifugal effect due to the rotation of the flow, pushing the fluid towards the external wall of the combustion chamber.
Once again, increasing the complexity of the system pushes away from the mathematical correctness: adding mass (blowing case) doesn't give any significant disturbance, but when the combustion takes place these formulas are no longer valid to

predict the pressure distribution due to temperature and fluid composition gradients in the radial and axial direction. However, the shape (increased pressure from center to walls) is still valid, and so its effect on the flow field.
In case of gradient of temperature or chemical species , this force acts as a mixer, letting the heaviest components (reactants) go in the outer part, while pushing the lighter (products of reaction) in the center of the combustion chamber. For this reason, the flame is more diffuse than using the axial injector (Fig. 5).

Chapter 4

CFD characterization

Use of CFD has not only the aim of design the motor itself, but also it helped in the experimental characterization.

In particular, the knowledge of what happen in combustion chamber is useful to decide sensors position and performance.

In this part, many motor configurations have been analysed, to evaluate fluid field in the following conditions:

- burn time: on a same chamber configuration, different inner grain diameter have been simulated;
- throttling: oxidizer mass flow has been modulated up to a ratio of 50%;
- devices: three combustion chamber configuration have been studied, evaluating the impact of pre-chamber, post-chamber and mixer.

In all these simulations, the fluid will be analyzed to understand its interaction with the measurement system. In particular, the choice of pressure sensors position is fundamental to have a precise measurement system and evaluate in a correct way the performance parameters.

CFD is a crucial point in the design process of an hybrid rocket, but must be clear that it has its own "sinks and sources of knowledge": there are many assumptions that made it a valuable tool to discretized between solutions, but can't be used to give a precise judgement on the goodness of a technical solution on its own, e.g. if you want to know the precise ($\pm$0.1bar) pressure. In this way it is used in this thesis: a 0-D tool (see chap.2.2) give a raw dimension of the motor, that can be checked out with CFD to study for example different injection methods, but all works can not be valid without experimental data, needed to tune the previous work for parameters like regression rate or mass flow with a certain injector.

4.1 Case analysis

4.1.1 Different burning time

In this part will be analysed the fluid field at different burning time. According to this, the geometry has different grain diameter: 25mm, 40mm, 55mm. The purpose is to evidence the fact that the vortex behaviour of the fluid in the combustion chamber remains also if there is a step (grain that is consumed) after injection.

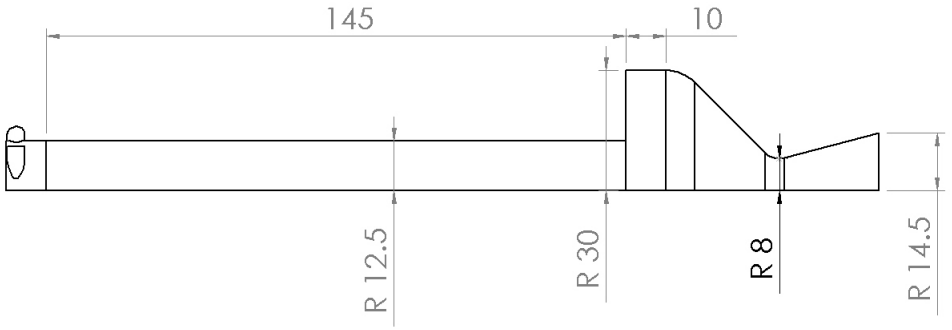

Figure 4.1: *Real* geometry simulated

The atual motor configuration, defined at the beginning of test campaing, is presented in fig.4.1, and is called *real*. Respect to cases discussed in chap.3.2, here the nozzle starts from a greater diameter, equivalent to the outer grain diameter.

As a comparison with the *basic* case is depicted in fig.4.2, where streamlines for *real* case are showed. At a first look, it can be noted that in combustion chamber the higher is the temperature, the more straight is the velocity vector in that point (see upper view). Again (fig.4.2(b)) there is a backflow in the injection zone, indicated by the grey isosurface of null axial velocity.

A difference is in the recirculation zone in the small post-chamber created by the nozzle (fig.4.2(b) and 4.4). This phenomenon is typical when there is a step in a geometry; it can be seen, also, that the vortex fluid continue to rotate in the same manner, as depicted in fig.4.3. Similar effects happen in simulation with higher port diameter, but with lower effect (recirculating vortex are smaller) for the obvious reason that the post-chamber zone and the step are smaller.

All variable, however, remain constant between the two simulations (*basic* and *real*), except from pressure that in *real* case is 1.5% higher (inside the uncertainty level of the software, 5%).

Different thing is the behaviour of most important parameters in combustion chambers with different grain diameter.

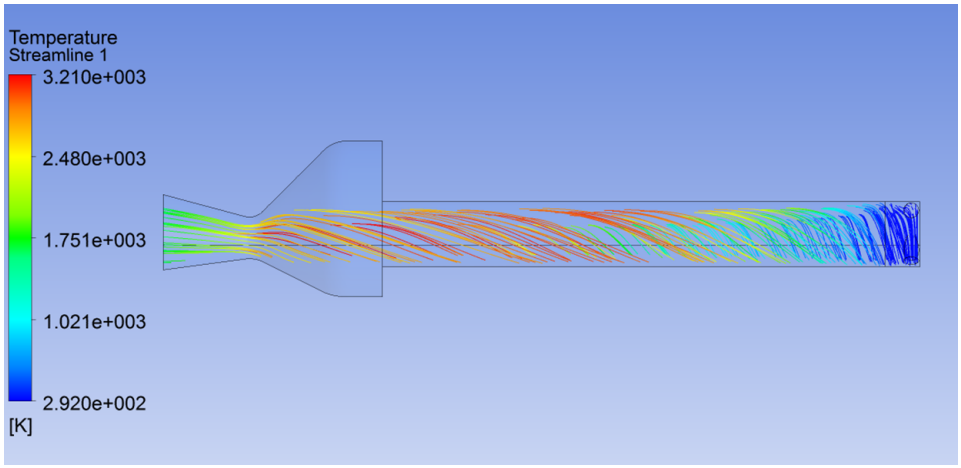

(a) Upper view

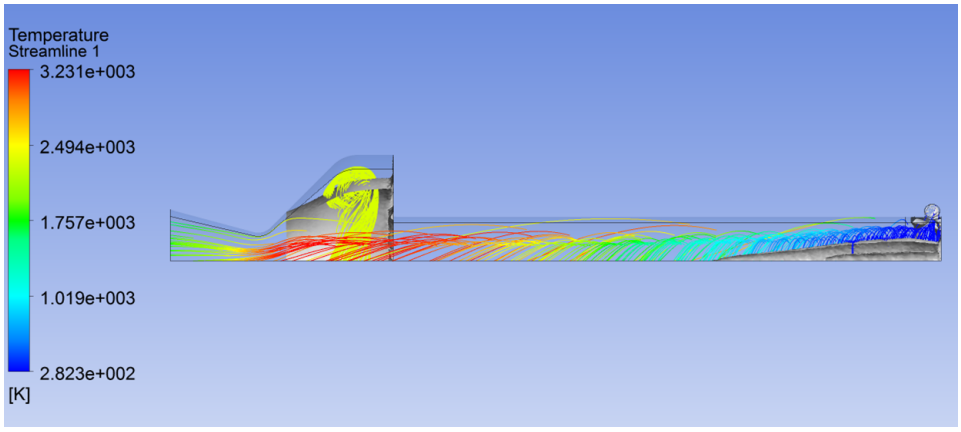

(b) Lateral view

Figure 4.2: *Real* case - streamlines

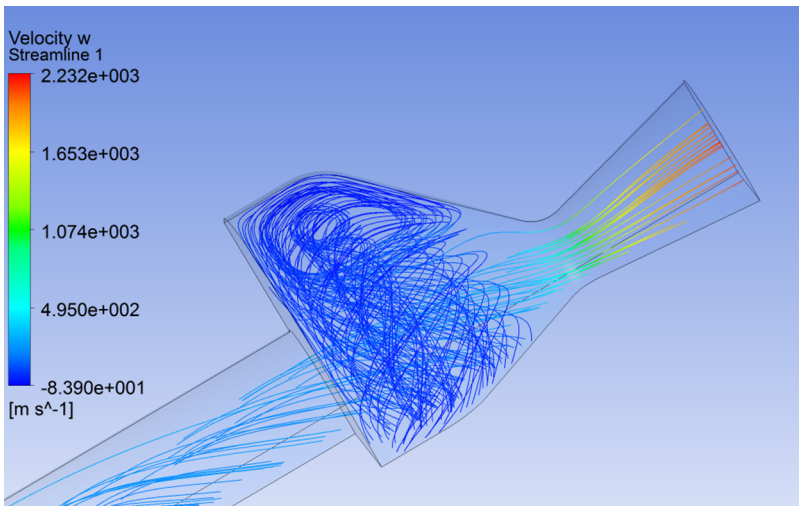

Figure 4.3: Streamlines in recirculation zone for *real* case

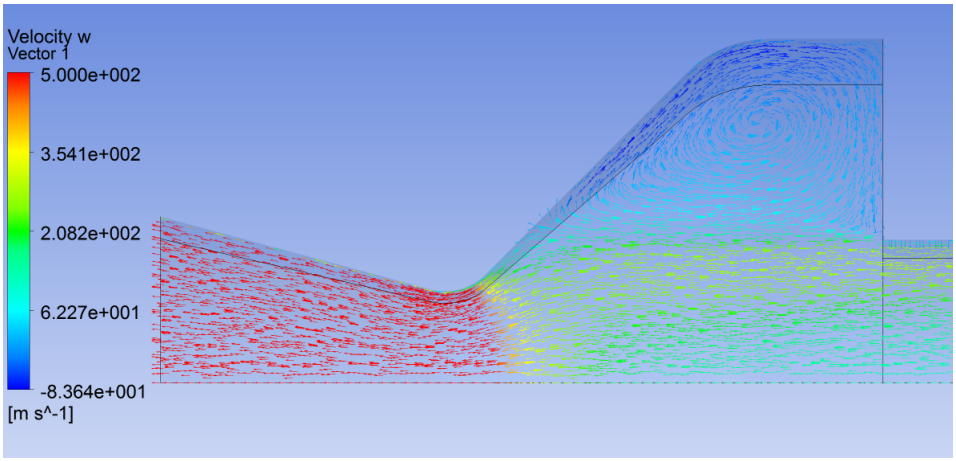

Figure 4.4: Vector plot in recirculation zone for *real* case

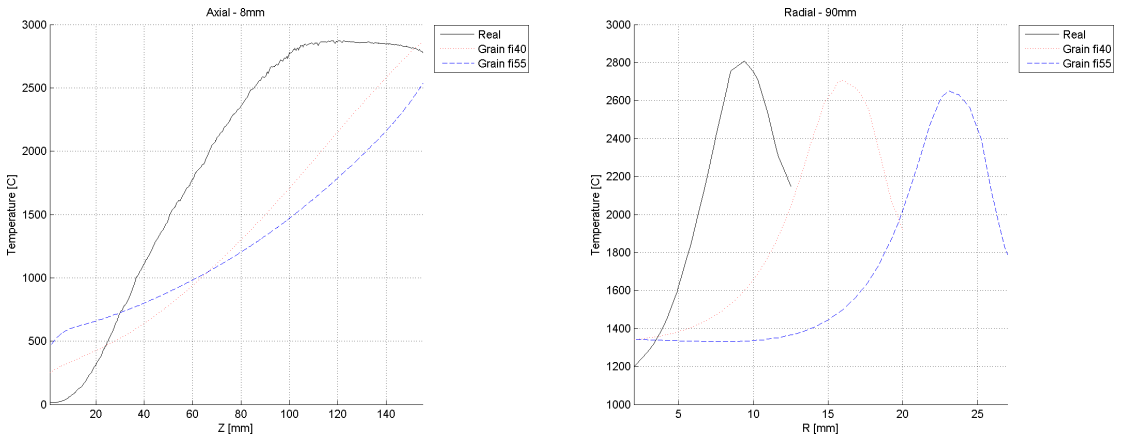

(a) Axial profile at 8mm from motor axis

(b) Radial profile at 90m from grain start

Figure 4.5: Different grain diameter comparison - temperature

In fig.4.5 temperature is plotted over a radial (distance 90mm from grain start) and an axial (at 8mm from grain axis) line. In the radial plot, it can be seen that the profile temperature is similar but dilated.

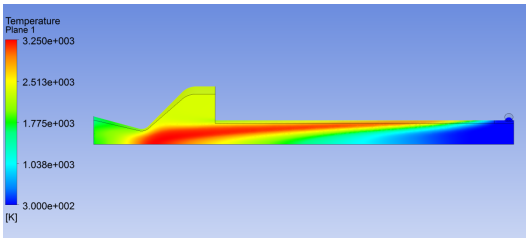

(a) Grain 25mm

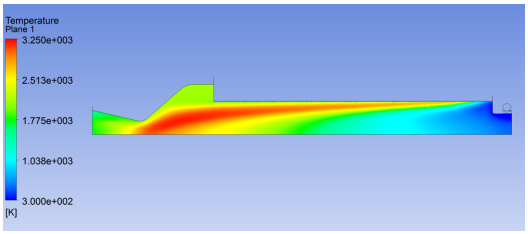

(b) Grain 40mm

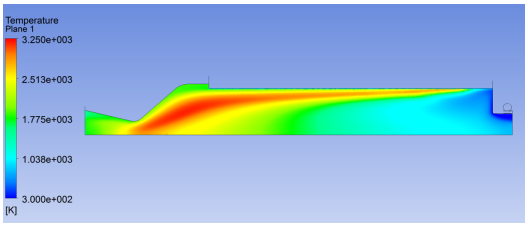

(c) Grain 55mm

Figure 4.6: Different grain diameter comparison - temperature

This is evident in fig.4.6 where temperature profile is plotted on a mid-plane. the flame shape is similar, but the temperature pike tends to remain near the grain wall due to the angular speed that act as a centrifugal force.

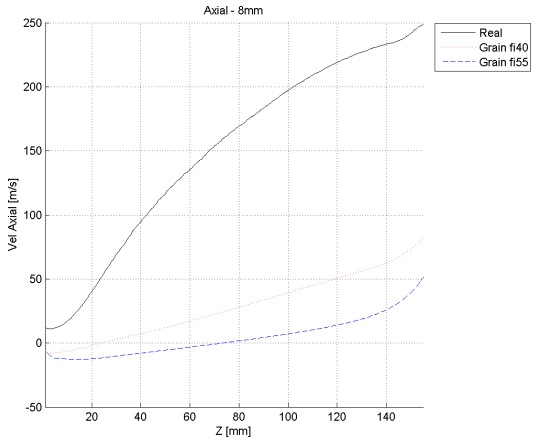

(a) Axial profile at 8mm from motor axis

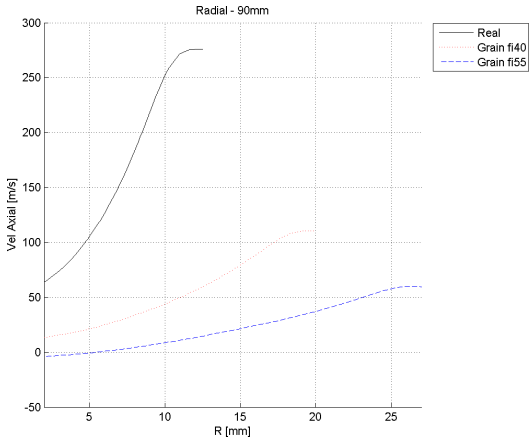

(b) Radial profile at 90mm from grain start

Figure 4.7: Different grain diameter comparison - axial velocity

Axial velocity (fig.4.7) evidence the same trend (growing) but with different value. The explanation is in the continuity equation: same mass flow at same pressure and temperature but different area where the fluid can pass through.

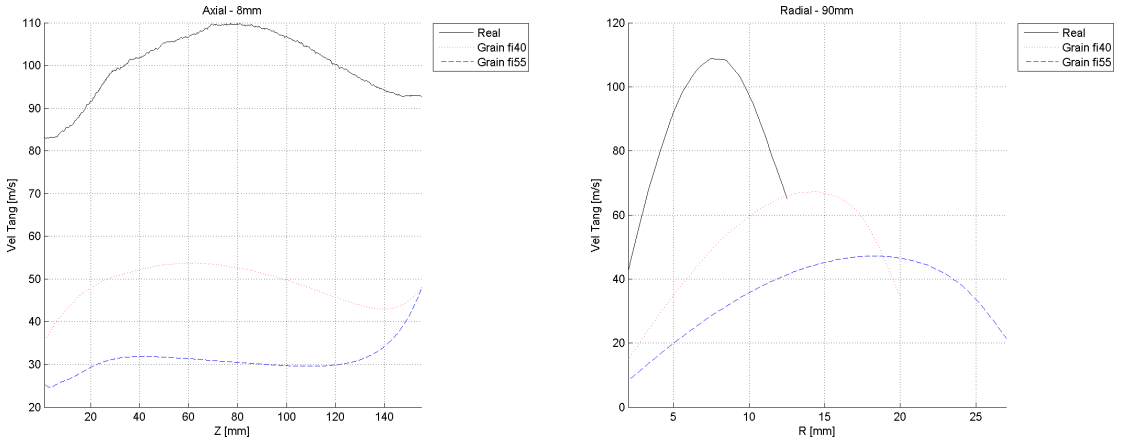

(a) Axial profile at 8mm from motor axis (b) Radial profile at 90mm from grain start

Figure 4.8: Different grain diameter comparison - tangential velocity

Analogous situation is if fig.4.8, where tangential velocity is plotted. The different values are explained by the angular momentum conservation: higher inertia (same mass on a greater radius) means lower angular speed.

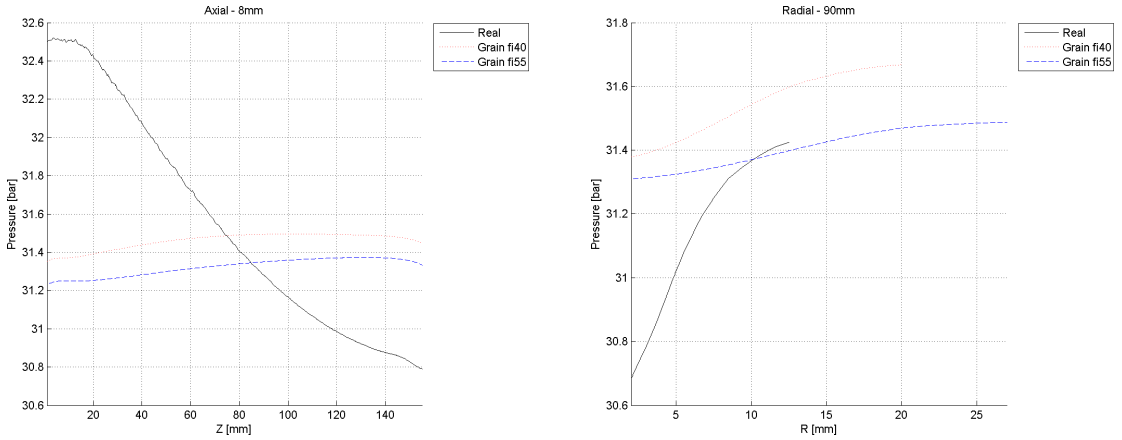

(a) Axial profile at 8mm from motor axis (b) Radial profile at 90mm from grain start

Figure 4.9: Different grain diameter comparison - pressure

Pressure profiles are shown in fig.4.9: the mean value is compatible between all three simulations, but trends are very different: with lower diameter of the grain port, the pressure gradient (both in axial and radial direction) is lower, due to the lower axial and tangential velocities.

4.1.2 Throttling

In this section we want to analyse the behaviour of the motor to different mass flow. As an assumption, same O/F ratio in all cases has been utilized.

The only change in geometry is the injection channels diameter: according to what explained in chap.3.1.2 and isentropic nozzle equation, to maintain the same mass flow and injection speed of the liquid case (remember, oxidizer when injected is in liquid phase) diameter must increase when pressure goes down.

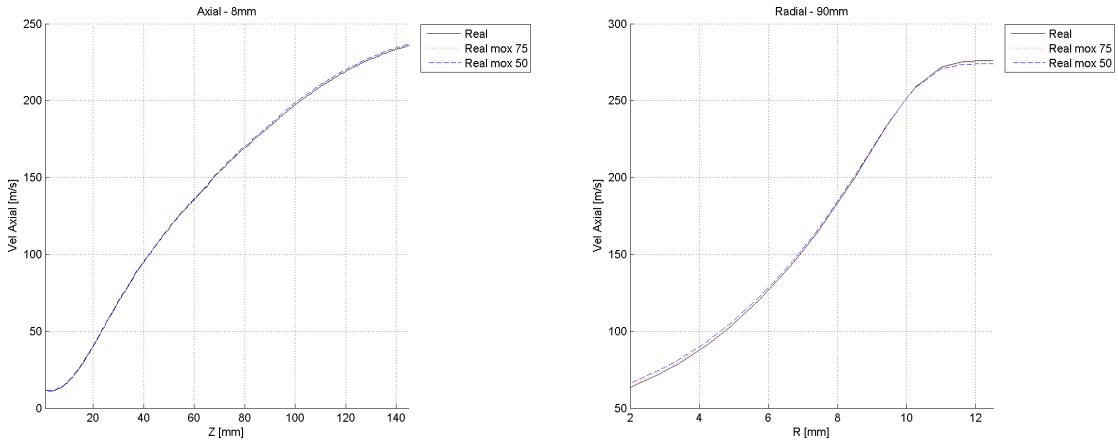

(a) Axial profile at 8mm from motor axis

(b) Radial profile at 90m from grain start

Figure 4.10: Comparison in different flow rate (full, 75%, 50%) - axial velocity

The fact that we don't simulate the liquid injection and evaporation is a very limiting factor, as will be exposed soon.

Fig.4.10 and 4.11 shows that velocity profiles remain unchanged between different cases.

The results show that do not change anything except for the pressure in combustion chamber.

Pressure (fig.4.12) is reduced according to nozzle isentropic equation.

Streamlines (fig.4.14) evidence the fact that the fluid field calculated with these hypothesis and simplifications is the same in all cases.

Temperature plots (fig.4.14) shows that reducing the mass flow the flame is sharper and less diffuse.

Mass flow definition:

$$\dot{m} = \rho v A \tag{4.1}$$

Ideal gas equation:

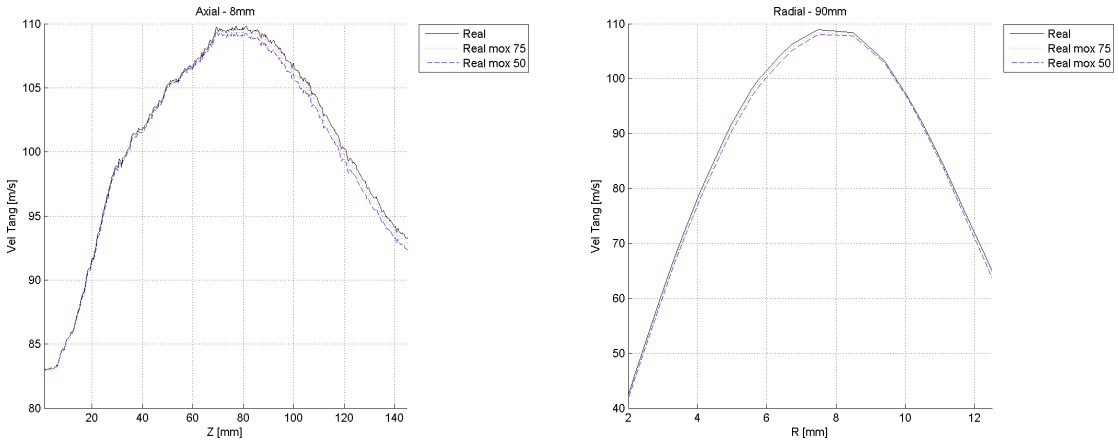

(a) Axial profile at 8mm from motor axis (b) Radial profile at 90m from grain start

Figure 4.11: Comparison in different flow rate (full, 75%, 50%) - tangential velocity

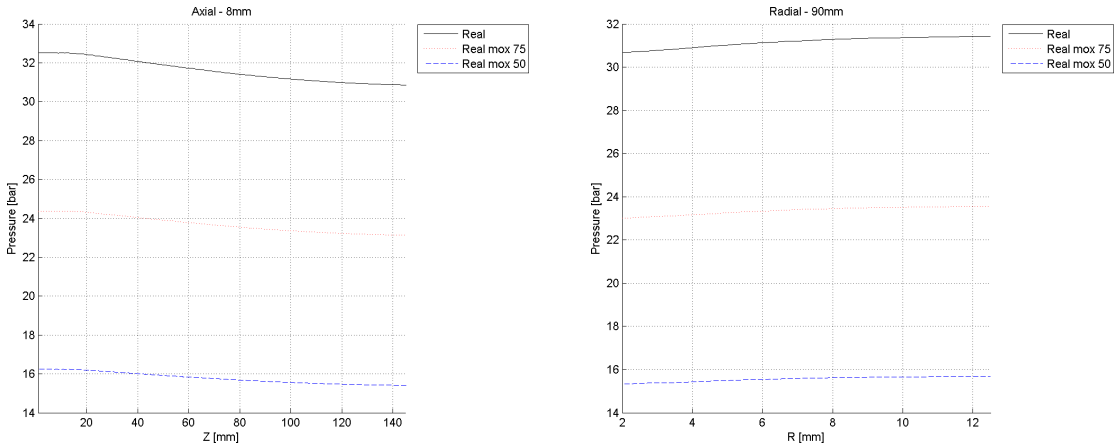

(a) Axial profile at 8mm from motor axis (b) Radial profile at 90m from grain start

Figure 4.12: Comparison in different flow rate (full, 75%, 50%) - pressure

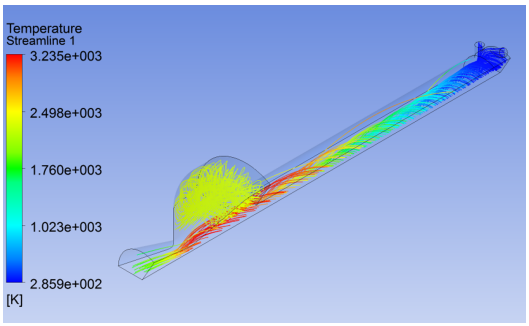

(a) Case full mass flow

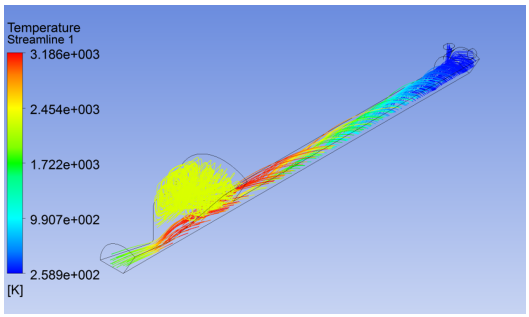

(b) Case mass flow at 75%

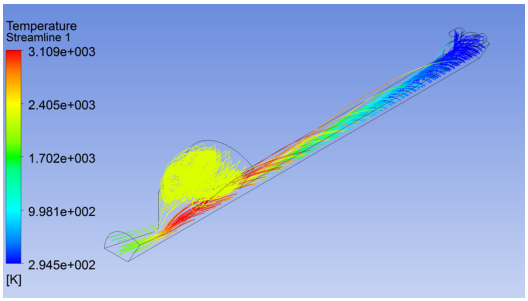

(c) Case mass flow at 50%

Figure 4.13: Comparison in different flow rate (full, 75%, 50%) - streamlines

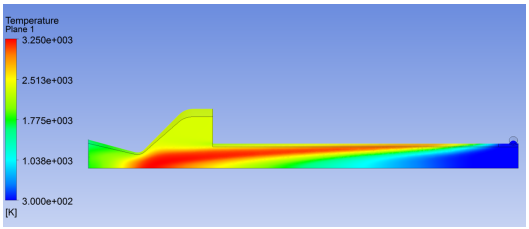

(a) Case full mass flow

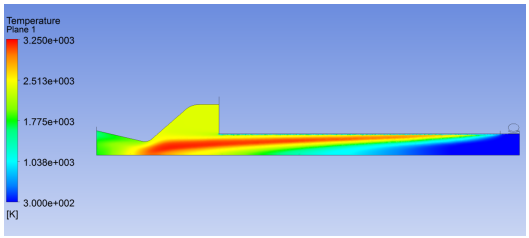

(b) Case mass flow at 75%

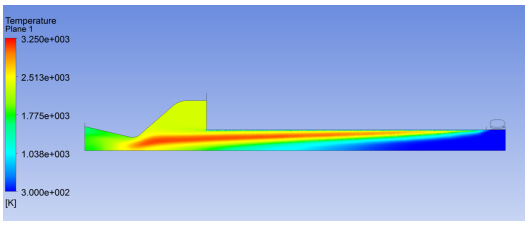

(c) Case mass flow at 50%

Figure 4.14: Comparison in different flow rate (full, 75%, 50%) - temperature plot

$$\frac{p}{\rho} = \frac{R_u}{M_m} T \tag{4.2}$$

Isentropic nozzle equation:

$$\dot{m} = \frac{A * p_t}{\sqrt{T_t}} \sqrt{\frac{\gamma}{R}} \left(\frac{\gamma + 1}{2} \right)^{\frac{\gamma + 1}{2(\gamma - 1)}} \tag{4.3}$$

with:

$$R = \frac{R_u}{M_m} \tag{4.4}$$

specific gas constant.

Fixed the temperature and species (and so T_t, R and γ) there is a linear relationship between pressure and mass flow from eq.4.3: half the mass flow means half the pressure.

All products and reactants in simulation have been modelized as ideal gases and then, from eq.4.2, half the pressure (fixed the temperature) means half the density.

Last passage, from eq.4.1 with fixed the mass flow, half the density means double the velocity.

For tangential velocity the explanation is similar: reduction in mass flow and in pressure are counter-balanced by a different injection holes dimension.

In the truth, however, there are many different facts that act a role in combustion chamber: the liquid injection cone has different shape with different chamber pressure; atomization of the oxidizer is different for all cases. All this causes a different combustion that change the combustion efficiency and so chamber temperature. In summary, for such a kind of analysis would be necessary a complete liquid-gaseous model for oxidizer injection.

One of the main parameter, more over, is the diameter of the injection holes, that has a great influence on the performance parameters of the motor in terms of velocities inside the chamber. The method to calculate oxidizer velocity in injection channels do not take into account for phenomena like cavitation or energy dispersion that lower the speed.

4.1.3 Internal devices

In this section, *real* case will be compared to three cases with a different configuration in combustion chamber:

- case *pre*: pre-chamber of 20mm length and 60mm in diameter;

- case *post*: post-chamber of 30mm length and 60mm in diameter;
- case *mixer*: mixer-like device after the grain.

Let's analyse first the *pre* case; the geometry is depicted in fig.4.15.

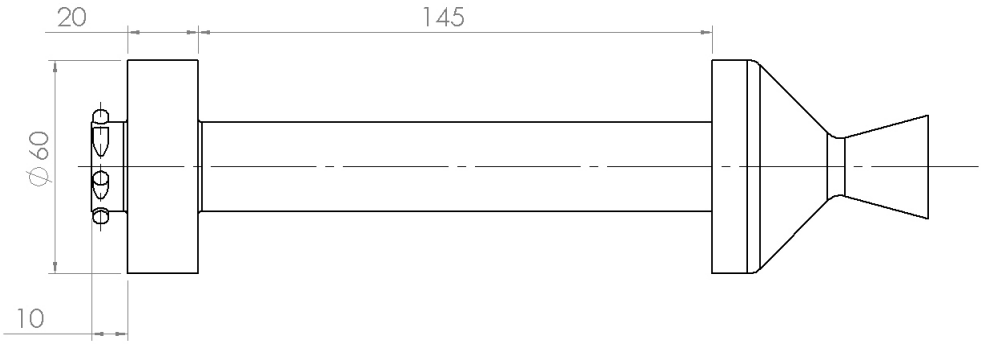

Figure 4.15: Case *pre* geometry (dimensions in mm)

The use of a pre-combustion chambers is helpful because it helps vaporize the liquid oxidizer adding more space before it encounters the fuel. Also in case of gaseous oxidizers (like oxygen or catalyzed hydrogen peroxide) the longer travel the gas have to do before the start of the grain tends to make it hotter.

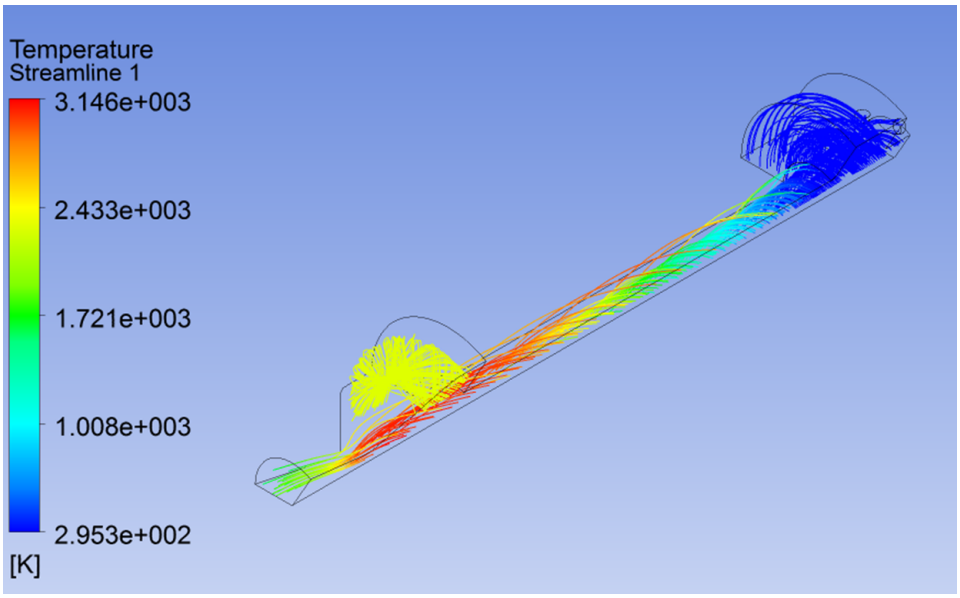

Figure 4.16: Case *pre* streamlines

First thing to ask is: do the vortex flow continue to swirl also with that sudden change in diameter? Answer is in streamlines showed in fig.4.16: yes.

Again, it as been found as expected that the sharp step causes a recirculation zone. This has a positive benefit in the fact that enhance the heating of the oxidizer

before it encounters the melted fuel. In fig.4.17, indeed, this zone is in evidence with a velocity vector plot, with colour based on axial velocity (scale is limited between $-10 \div 0$ m/s to have a clearer view of the phenomenon). The isosurface of null axial velocity is used as a delimiter for different direction (forward and back) flow.

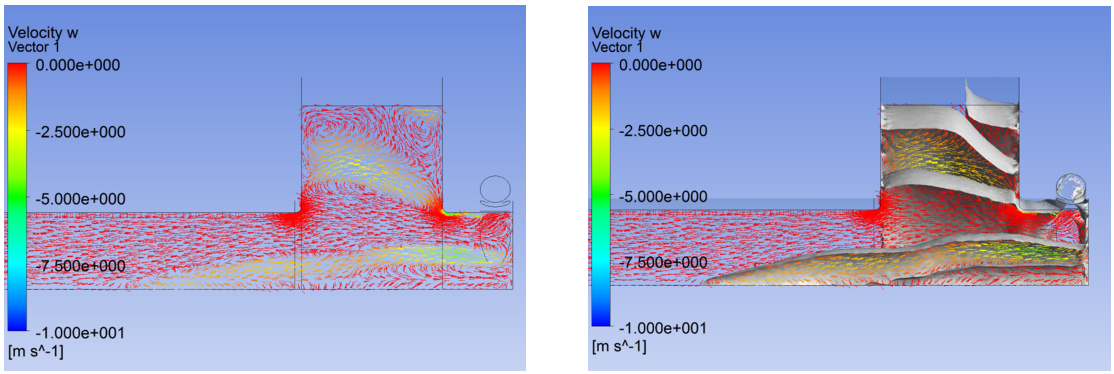

(a) Velocity vector

(b) Velocity vector and isosurface of null axial speed

Figure 4.17: *Pre* case - flow recirculation in pre-chamber (vector colour is axial velocity)

Post case, on the contrary, have the same space used in the previous case (a void volume of 20mm length and 60mm of diameter) but placed after the grain. Use of the post-chamber is very diffuse in all propulsion branches, as liquid and solid. the purpose is to extent the space in which chemical reactions can take place, and to have a better mixing of chemical species.

Streamlines and recirculation zone are very similar to *real* case (see fig.4.18).

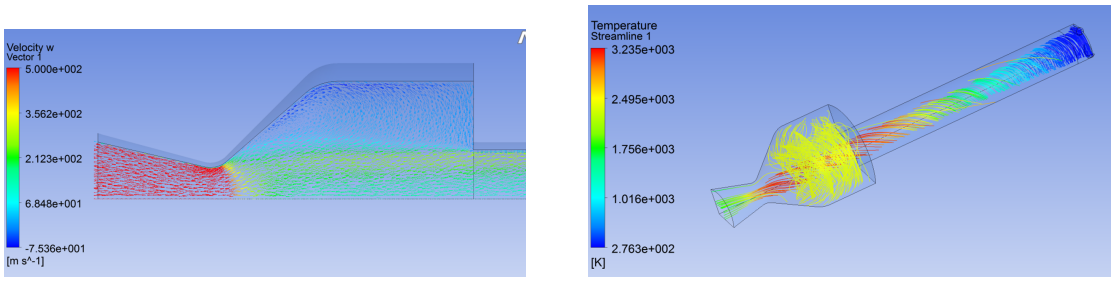

(a) Velocity vector - color scale limited

(b) Streamlines

Figure 4.18: *Post* case - flow recirculation in post-chamber and streamlines)

The *mixer* case have a geometry similar to what showed in fig.4.19: a drilled diaphragm have been placed between the end of the grain and the nozzle. Such a

device has already been used in the middle of the combustion grain in previous works, and has demonstrated several benefits [8].

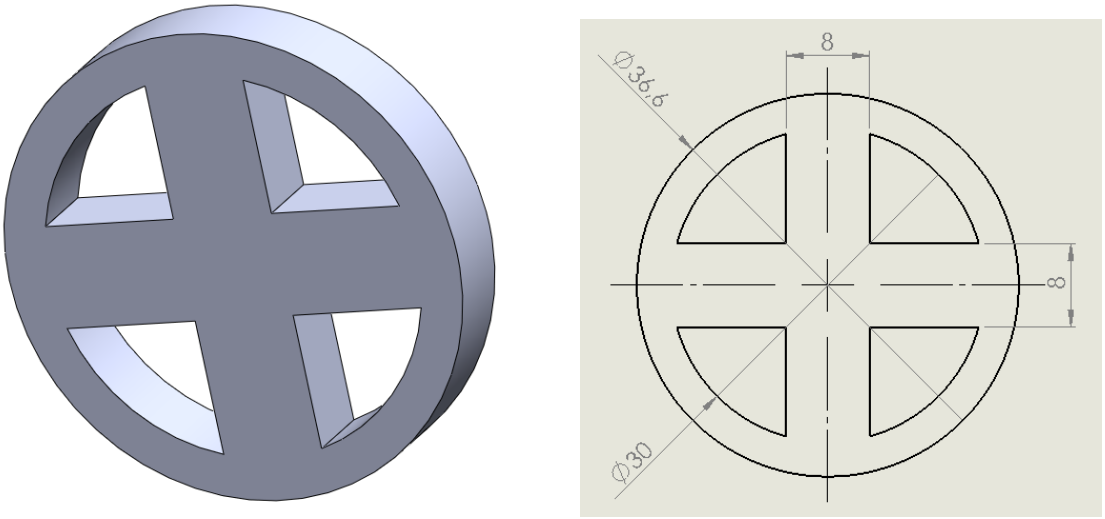

(a) 3D model (b) Schematic drawing

Figure 4.19: Mixer-like device

The purpose is to enhance the mixing of products with the turbulence created after the device, and to eliminate the tangential component of the velocity in the nozzle region.

Streamlines are similar to *real* case in the combustion chamber region.

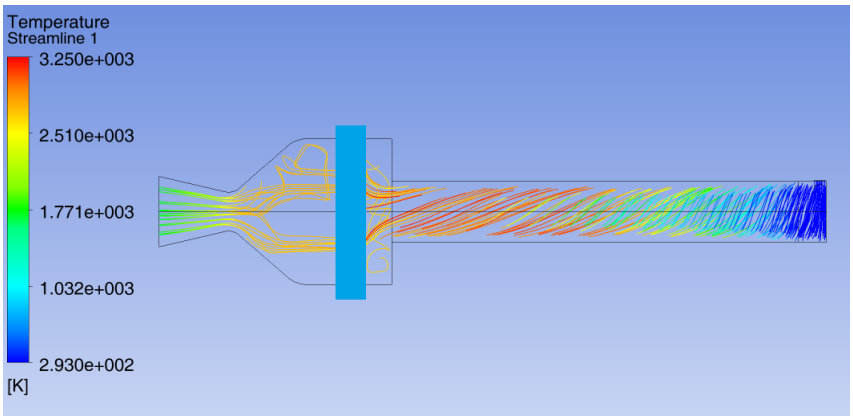

Figure 4.20: Case *mixer* streamlines

The main difference in after the device, where a recirculation zone (different from previous) is affecting the fluid field as showed in fig.4.21.

In that picture is clear (see also 4.21) that there is no more a vortex field, but a more complex one, with a great turbulence created by all recirculations. This

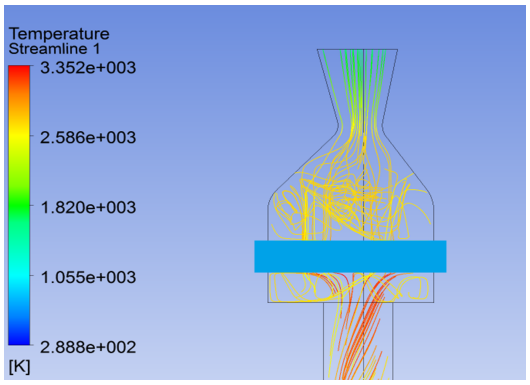

Figure 4.21: *Mixer* case - flow recirculation in nozzle zone

enables a complete mixing of the reactants. All this is not for free, but there is a pressure loss in the device that drops from a mean value of 35.1bar before the holes to 31.3bar after.

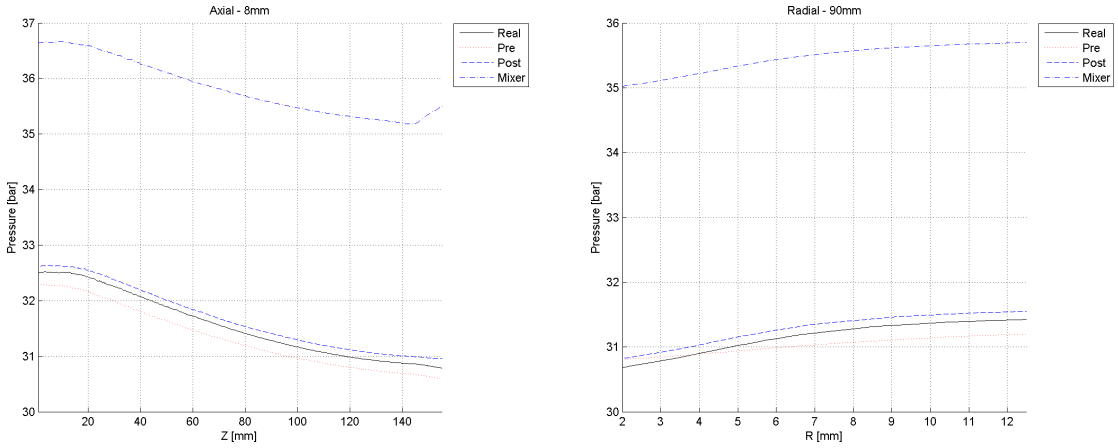

(a) Axial profile at 8mm from motor axis

(b) Radial profile at 90mm from grain start

Figure 4.22: Axial and radial comparison plot - pressure)

It has however to be noted that, despite the pressure drop, the resulting pressure that act propulsively (it means, the pressure right behind the nozzle) is similar to that of other cases (see fig.4.22). In more simple words, using a mixer enhances the combustion increasing its efficiency.

In fig.4.23 CFD simulation temperature profiles are plotted. Flame inside combustion chamber is compatible in all cases, and it's also very close to the *real* case. The main difference is in the homogeneity in the nozzle section.

In fig.4.24 temperature is plotted in axial and radial line. It can be seen that the *pre* case starts at a slightly higher ($1435°C$ vs. $1321°C$) temperature in radial case near the motor axis. This is the pre-heating phenomenon before mentioned.

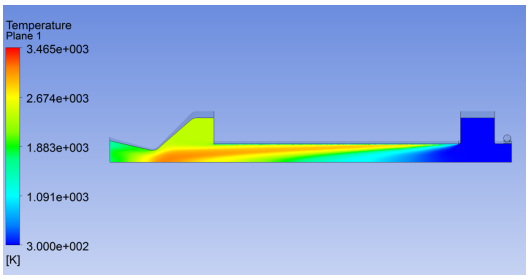

(a) Case *pre*

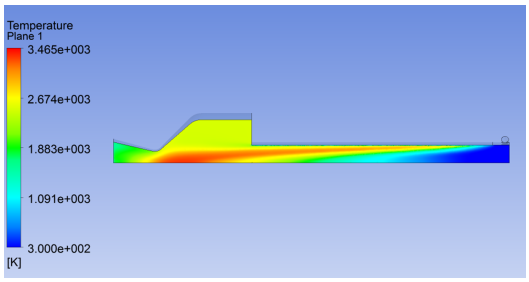

(b) Case *post*

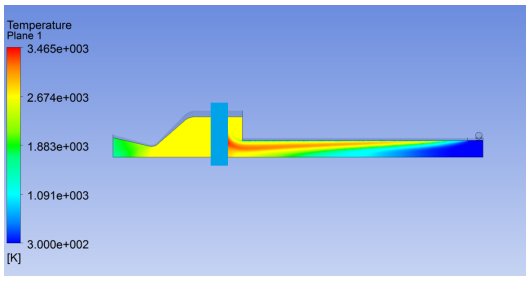

(c) Case *mixer*

Figure 4.23: CFD simulation comparison - temperature)

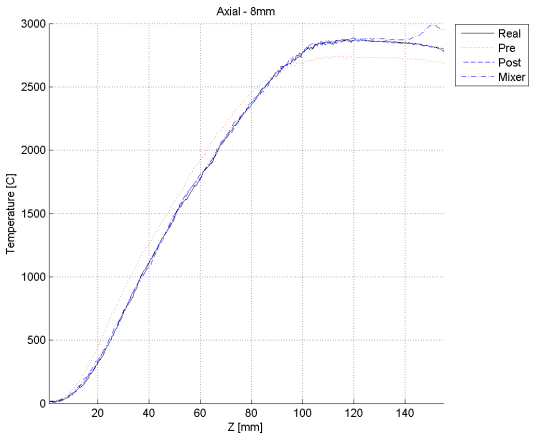

(a) Axial profile at 8mm from motor axis

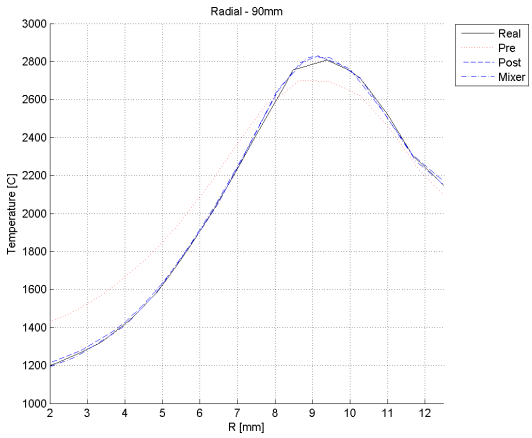

(b) Radial profile at 90mm from grain start

Figure 4.24: Axial and radial comparison plot - temperature)

Apart from this, trends in combustion chamber are similar.

4.2 CFD summary

We want now to summarize all work done in CFD analysis.
Several models have been simulated, defining four groups on tests:

1. *basic*: understand the main parameters influencing the vortex fluid field, and analyse the differences with axial injection;
2. *grain*: variation of the internal grain diameter;
3. *throttling*: variation of oxidizer mass flow;
4. *devices*: different combustion chamber configurations;
5. *analytical*: Navier-Stokes equations have been used to discuss about pressure gradients and flow profile;

All simulations are steady state, with many assumption and simplification in the model, like:

- gaseous injection of both fuel and oxidizer;
- eddy dissipation combustion model with fixed chemistry;
- ideal gas equation for all fluids in the combustion chamber.

Starting from the beginning, it has been shown that the main parameter that influence the vortex fluid field is the combustion: it affect the axial velocity impressing an acceleration; this, with the fact that the radial velocity is negligible and the tangential velocity is less influenced, straighten the fluid field. The tangential velocity has been proven that follows a forced vortex profile in the inner part of combustion chamber, that change to adapt to the outer boundary condition and the rise temperature in the flame.

Comparing axial and vortex injection, we can say that the first type has a narrow flame region (with flame, we mean the highest peak temperature). The more turbulent flow in vortex enhance the mixing of products and reactants, increasing combustion efficiency and regression rate.

Variation of grain diameter, maintaining the same mass flows, showed that the vortex streamlines remains also if a sudden step is introduced right after the injection point. To respect continuity equation and angular momentum conservation,

speed (both tangential and axial) is scaled down but qualitatively preserves the same trends.

Change in oxidizer mass flow (maintaining the same O/F ratio) requested a change in injection geometry due to a change in flow speed. It has been demonstrated that with this type of solution everything remains still except for the chamber pressure that follows the isentropic nozzle equation (less flow and same temperature means less pressure). The vortex flow is not affected by this variation.

Devices inside combustion chamber can have different uses: mixers between end grain and nozzle enable a better mixing of reactants and products, enhancing the combustion and straightening the flow in the nozzle section. Pre-chamber between injection and grain has the benefit to heat the oxidizer before it encounters the hot fuel. Moreover, add space to its travel to permit it to evaporate. This, obviously, has not been simulated due to simplifications on the model. A post-combustion chamber, instead, is a zone placed after the grain, a void volume used to increase the space where reactions can take place.

Analytical discussion using Navier-Stokes equations in cylindrical coordinates showed and confirmed the vortex flow behaviour of the fluid inside the combustion chamber using vortex injection. Moreover, a pressure and density profile has been discovered. Comparison with CFD data has proven the validity of the theory, with all precautions given by the simplification: no temperature gradients and no molar mass variation. This has been shown to be valid in the injection region, where the main component is the oxidizer.

What we have seen is that the best point to measure chamber pressure is right before the nozzle, where the influence of a radial pressure gradient is the weakest. Another advantage for this point is seen with the mixer-like configuration: pressure must be measured after the device because that is the correct value to evaluate the motor performance.

Drawbacks of these simulation is the fact that we do not simulate liquid injection, that has been proven to have significant effects especially in the injection region. In particular, simulations in which use of pre-chamber or change in oxidizer mass flow (as thus change in injection speed) is requested can be affected in their results.

The use of CFD simulation is a powerful tool but it must be clear that they aren't the very truth; the use done in this thesis is to compare different cases: trends are very well simulated.

Furthermore, they help in choosing specific configuration in the measurement

system. As an example, position of pressure sensors must be in the post-chamber to have a minimum effect due to the pressure gradient in radial direction. Again, we can understand that the nozzle effect (fluid acceleration) is still negligible in that zone.

Chapter 5

Throttling

One of the main topics of this thesis is the throttle of the oxidizer mass flow. There are many methods to achieve that purpose, and the main are:

1. pulsed system;
2. variable orifices injection.
3. pintle injection;
4. regulating valve;

The first method is not properly a variable thrust, but permits to obtain a mean thrust profile to achieve a specific goal. Typical example is the use of on/off systems in attitude control, with cold gas or mono-propellant thrusters.

The second method, instead, consists of a double plate injection, with one plate fixed and the other moving: in both sides a different holes pattern is machined; rotating one of them permits to have different holes opened or closed. In terms of throttling, this method permits a step-modulation of mass flow and thrust.

A pintle injection system is a well know device to throttle a propulsion system; it was the first choice in the Apollo 11 Lunar Ascent Motor [14]. The design (see fig.5.1) is composed of two coaxial bodies that permits the flow to pass through; changing the mutual position, the injection area can vary, and so the mass flow and spray angle [13].

The regulating system has the peculiarity that do not act in the injection point, but in the feed system. The idea at the base is to introduce losses in the fluid line, to reduce the pressure and so the mass flow. Such a method, usually, involve a motor performance degradation with throttling, due to a different injection "shape" of the oxidizer in the combustion chambers [32].

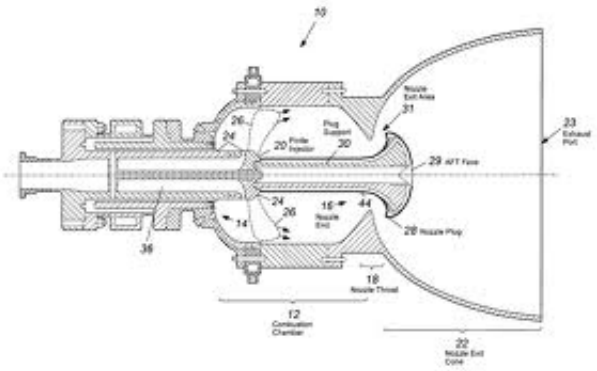

Figure 5.1: Pintle injector scheme

Usually such systems, to achieve a more stable and fine throttling control, require a double regulation system: one like those mentioned above and one in the pressure tank. In our case, pressure is regulate at 80bar and must not decrease in value: we don't want to achieve an auto-pressurized system. It has to be said that this is a peculiarity of this kind of motor, that is not observed with other oxidizer but only with N_2O.

5.1 Valve design

To obtain a continuous modulation of the thrust, as reported before, the choice was between a pintle valve or a regulation system in the feed line.

The choice was this last method, because in this way we can decouple the effects of the vortex injection system to those of the regulating valve.

The choice for the valve fallen in a needle valve from Ham-Let (see fig.5.4).

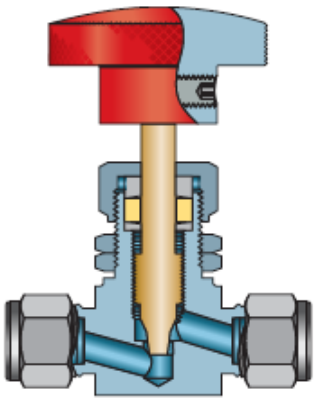

Figure 5.2: Needle valve scheme

The flow enters from the right. The rotation of the yellow stem pulls it up and

down. In this way we can achieve the desired pressure loss in the feed system.

The materials used, according to N_2O compatibility data, are stainless steel (AISI 316) for the body and stem, and PTFE for the sealing.

The design of such a device require the use of the following formula:

$$q = N_1 C_v \sqrt{\frac{\Delta p}{G_f}} \tag{5.1}$$

where G_f is the specific gravity (ratio between density of liquid used and that of water), q is the volumetric flow, Δp is the pressure difference ($p_1 - p_2$ in fig.5.3), C_v is the flow coefficient and N_1 is a multiplicative coefficient that depends on the measurement units used. When q is expressed in L/min and pressure in bar, $N_1 = 14.42$.

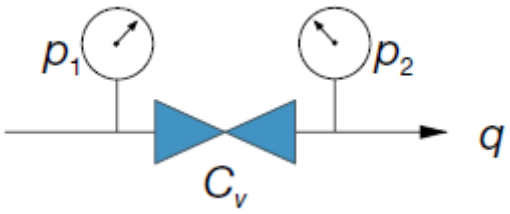

Figure 5.3: Needle valve design rapresentation

The role of the C_v coefficient is like an energy loss, and the lower its value, the higher the loss.

In our case p_1 is the pressure in tank data. For this reason, in calculating G_f the density of N_2O we take NIST data [2] for 80bar and 25°C, values used in our tests. The density value is $796 kg/m^3$.

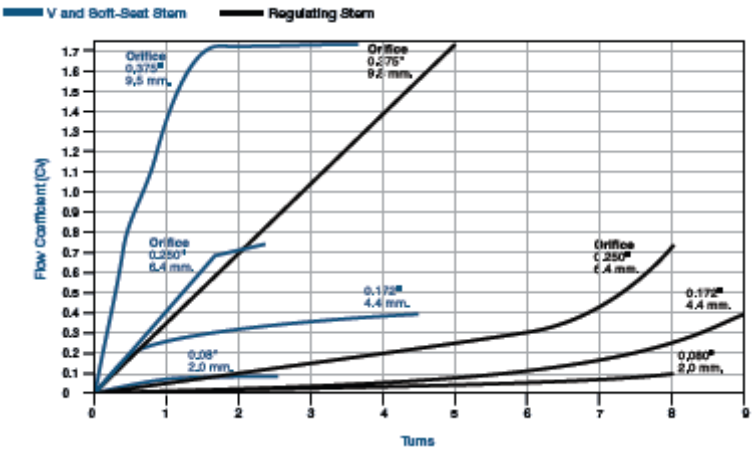

Figure 5.4: Needle valve characterization

First, we wanted that when fully opened, the C_v coefficient would be as higher as commercially possible, with the intent to have the lowest pressure drop (design goal fixed at 0.1bar) possible. To achieve this goal, a piping dimension of 1/2" is required.

Another choice parameter is the type of stem: we choose the *regulating* stem, in order to have a linear C_v decay.

Theoretical values for the chosen valve are reported in fig.5.4.

5.2 Valve characterization

To evaluate the performance of the needle valve, a characterization is needed before its use in the hybrid motor. In our intent, we wanted to reconstruct the plot in fig.5.4.

Another purpose of this investigation is to define the valve needle position to achieve a reduction in mass flow of 75% and 50%, that are the value used in throttled burn test.

The test bench apparatus was composed by:

- a tank able to withstand pressure up to 80bar;
- the needle valve;
- an electro-pneumatic valve;
- the vortex injector used during burn tests.

A scheme is reported in fig.5.5, while the actual setup can be observed in fig.5.6.

It was chosen to use also the vortex injector to have the closest configuration possible to the real burn tests.

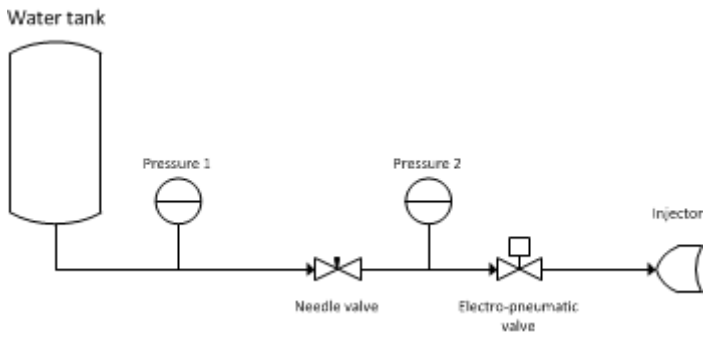

Figure 5.5: Needle valve characterization setup scheme

The procedure was the following:

1. fill the tank with water;
2. pressurize the tank up to 30bar;
3. measure the weight of the tank;
4. set the needle valve to the desired stem height (turn the grip handle)
5. open the electro-pneumatic valve for 5s and discharge the water;
6. measure the weight of the tank.

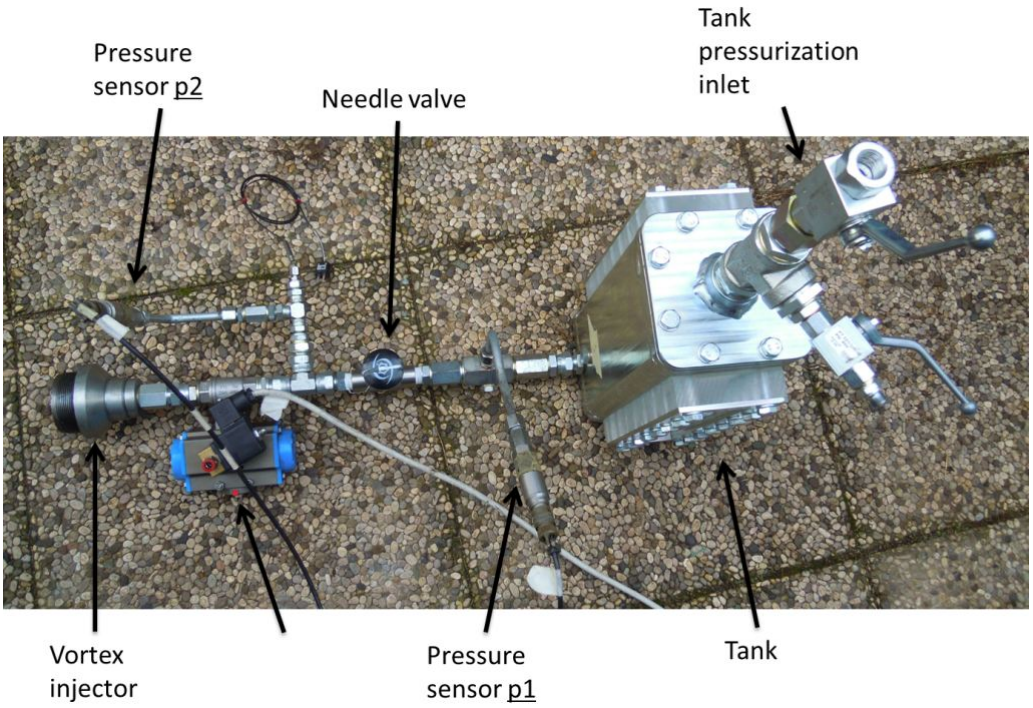

Figure 5.6: Needle valve characterization setup

There is one observation in this procedure: the pressure tank can vary during the water discharge. This is not a problem, because pressure is measured continuously; on the contrary, mass is measured as a mean value before and after the test. To reduce errors in the calculus of the flow coefficient, it is a good choice to fill the tank volume as low as possible (the water volume was 1/10 of the void volume in our case); in this way, also the pressure difference in the tank will be low. To avoid this problems, it would be indicate to use a mass flow measurement system (like a volumetric system, a turbine) and/or a pressure regulating system to maintain always the same pressure in the tank.

To calculate Cv, rearranging 5.1, and remembering that the specific gravity for water in unitary, we obtain:

$$Cv = \frac{q}{N1}\sqrt{\frac{1}{\Delta p}} \tag{5.2}$$

Mass flux is calculated as:

$$q = \frac{M1 - M2}{\rho \Delta t} \tag{5.3}$$

where $M1$ and $M2$ are masses of the tank before (1) and after (2) the test, ρ is the water density (equal to $1000 kg/m^3$) and Δt is the test run time, setted up at 5s.

Table 5.1: Valve tests summary - part 1

Valve turns	**Discharged water mass [kg]**	**Discharged water mass uncertainty**	**Mass flux** [L/min]	**Mass flux uncertainty**
0.125	0.50	5.7%	6.0	6.0%
0.25	1.18	2.4%	14.2	3.1%
0.5	1.32	2.1%	15.8	2.9%
0.75	1.26	2.2%	15.1	3.0%
1	1.39	2.0%	16.7	2.9%
2	1.32	2.1%	15.8	2.9%
5	1.50	1.9%	18.0	2.7%

Table 5.2: Valve tests summary - part 2

Valve turns	Δp mean [bar]	Δp uncertainty (3σ)	Theoretical Cv	Mean Cv	Mean Cv uncertainty (3σ)
0.125	23.0	4.0%	0.045	0.075	2.0%
0.25	12.7	9.2%	0.09	0.238	4.6%
0.5	4.9	11.5%	0.18	0.428	5.7%
0.75	2.1	26.6%	0.27	0.627	13.1%
1	2.1	11.7%	0.36	0.683	5.8%
2	1.2	10.3%	0.72	0.851	5.1%
5	0.8	15.9%	1.8	1.182	7.9%

Uncertainty analysis has been performed, using Kline-McClintock formula [20].

$$i_y = \left[\sum_{k=1}^{N}\left(\frac{dy}{dx_k} i_k\right)^2\right]^{1/2} \tag{5.4}$$

Estimated uncertainties on measured data are the following:

- $\Delta t = 0.1$s - due to opening and closing valve time;
- M1 and M2 = 0.02kg - balance uncertainty and repeatability;
- pressure = it's a continuous value, uncertainty determined by standard deviation (3σ).

Using eq.5.4, uncertainty on mass flux is:

$$i_q = \left[2\left(\frac{1}{\rho \Delta t} i_t\right)^2 + \left(\frac{M1 - M2}{\Delta t^2 \rho} i_{\Delta t}\right)^2 \right]^{1/2} \tag{5.5}$$

Uncertainty on flow coefficient is:

$$i_{Cv} = \left[\left(\frac{Cv}{q} i_q\right)^2 + \left(\frac{Cv}{2\Delta p} i_{\Delta p}\right)^2 \right]^{1/2} \tag{5.6}$$

In total, 7 handle turns have been tested (from 1/4 to 5), going more deeply in the "low turn" zone, from 0 to 1. The reason is that these are the most used values for low mass flow tests (75% and 50% throttling).

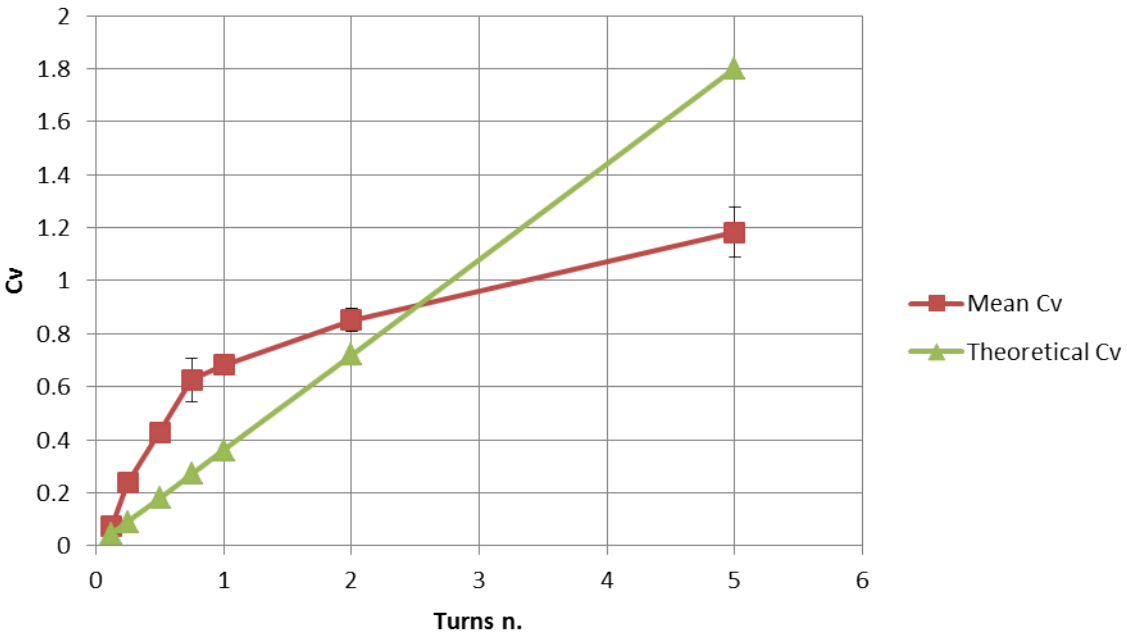

Figure 5.7: Needle valve tests chart

In fig.5.7 results are plotted, and a comparison with datasheet data is presented. It can be seen that, in particular in the interest zone (between 0 to 1 valve turns)

the calculated data do not fit with the theoretical value. On the contrary, there is a negative effect: the sensitivity of the flow coefficient to the handle position is higher (double than manufacturer specs.). In table 5.1 and 5.2 a summary of test data is reported.

Pointing at uncertainty, it can be said that for flow coefficient it remains below 6% except for two cases: for both of the, this is due to a high (5bar) pressure difference in tank before and after the test. This is negative because it goes against the validity of the stationary mean mass flow hypothesis.

A similar analysis has been performed also using the experimental test bed used for the motor.

Similar trends have been observed (see fig.5.8).

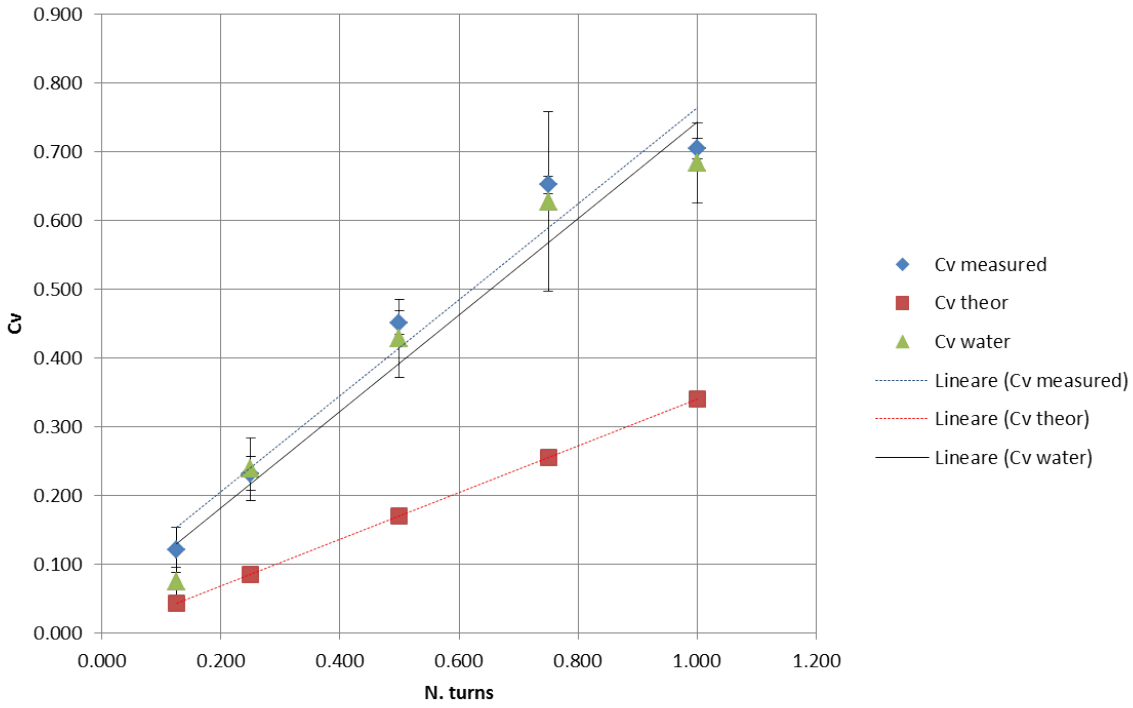

Figure 5.8: Needle valve tests chart

In this case, only the zone between 1/8 turns and 1 turns have been analyzed, and this for two reasons: first it is the test-interested zone and second is that outside this zone (higher needle turns) the pressure difference felt outside the measurable range and inside the instruments uncertainty range (mass flow is different respect to water tests).

Numerical value are reported in table 5.3.

It can be seen that experimental results (water and N_2O) are compatible between each other, but not with datasheet data.

Table 5.3: Cold test needle valve characterization data

Needle turns	Cv measured	Uncertainty	Rel. uncert.	Cv theor
0.125	0.121	0.004	3.3%	0.0425
0.250	0.232	0.006	2.5%	0.085
0.500	0.451	0.008	1.7%	0.17
0.750	0.651	0.009	1.3%	0.255
1.000	0.704	0.011	1.5%	0.34

Another observation is that uncertainty in cold test is lower. This is due to the fact that in that case both pressure difference and mass flow have been measured in continuous mode.

Final consideration is that for burn test data the needle position has been defined:

- 1/4 turns for the 75% throttling;
- 1/8 turns for the 50% throttling.

Chapter 6

Experimental activity

The last part of every project is the experimental activity. In summary, we started from a 0-D transient analytical model, that in few seconds for every test gave us a preliminary design of the motor in terms of dimensions and performance.

Then, CFD analysis with a steady state model helped us to have a clear view of what happens inside the combustion chamber. Different models have been implemented, each one with its peculiarities. This has been useful in the definition of the experimental setup, e.g. in sensors selection and positioning.

And the end of this process, an experimental campaign has been planned.

The design of an experimental campaign can be divided in the following parts:

1. test matrix definition;
2. test bed design;
3. measurement system definition;
4. data analysis.

In the following, each element will be analysed.

6.1 Test bed

The motor described before is connected to other external devices, to complete the test bed configuration:

- feed line with needle valve and electro-pneumatic valve;
- oxidizer tank;

- pressurization system;
- thrust measurement.

A schematic view of the system is shown in fig.6.1.

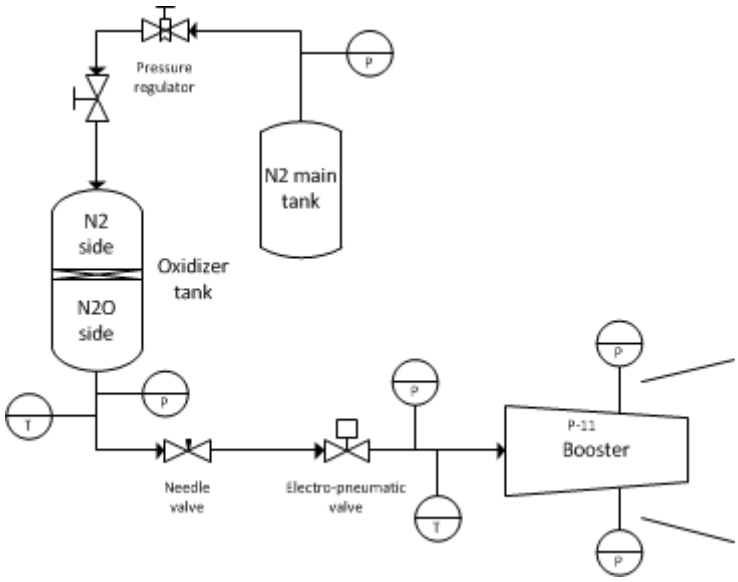

Figure 6.1: Test bed hydraulic and pneumatic scheme

The motor is provided of an oxidizer tank with an inner diameter of 160mm and a length of 306mm for a total empty volume of $6.15dm^3$. In the internal zone, a sliding piston can compress the fluid (see fig.6.2) to maintain the oxidizer at the desired pressure during the discharge.

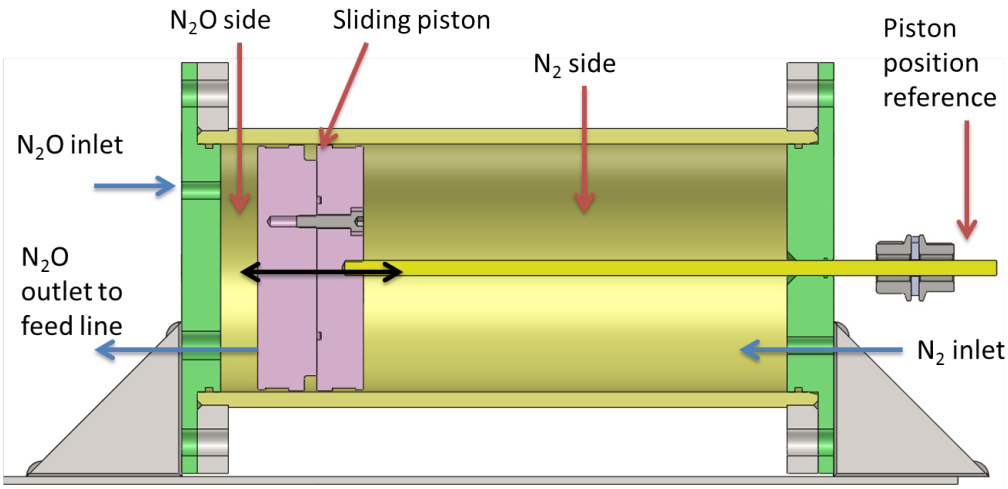

Figure 6.2: Tank internal view

The piston separates two different zone inside the tank, one filled with nitrous oxide (left in picture), and the other with nitrogen (right in picture). Sealing is

maintained by energized Parker o-rings.

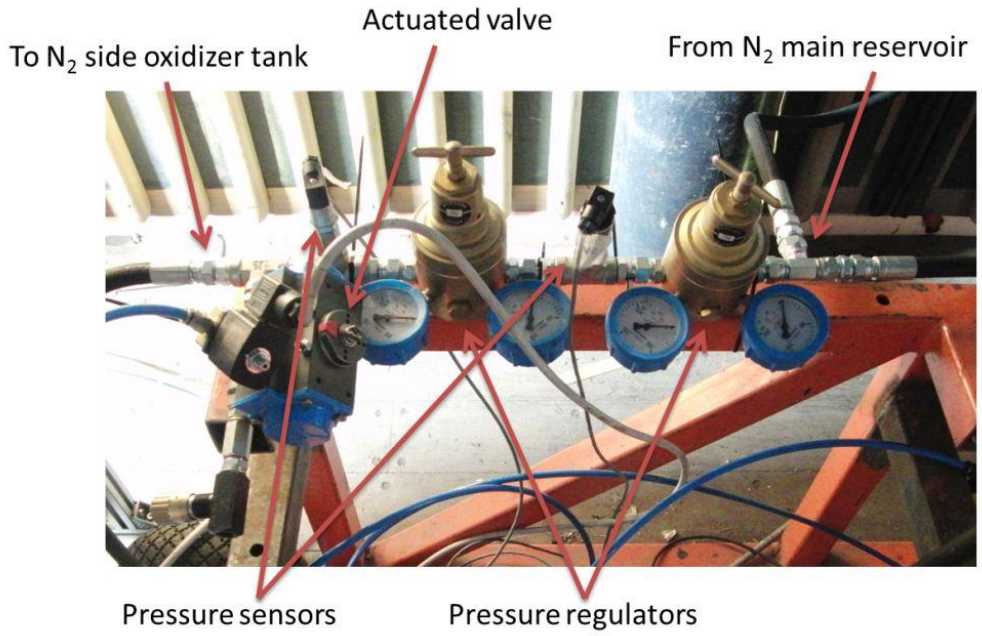

Figure 6.3: Pressure regulation system

The pressurization system (see fig.6.3) starts from a N_2 reservoir kept at pressure between $100 \div 200$bar. Nitrogen goes through 2 pressure regulators, that are fully mechanical devices needed to reduce the pressure in 2 steps for a finer setting down to 80bar (fixed oxidizer pressure for our tests).

Piston position is measured with an external potentiometer (see fig.6.4). This data, together with temperature and pressure information in N_2O, is used to evaluate oxidizer density and mass flow during burn tests. In fig.6.5 are showed pressure and temperature sensors position. In particular, temperature is measured in 3 points (1/4 - 1/2 - 3/4 of the total height) to avoid (and in case reveal) errors due to stratification of the fluid.

Feed line is the group of devices (tubes, fittings, sensors and valves) that connects the oxidizer tank to the motor (see fig.6.6). It comprises, in order from tank, the needle valve, an electro-pneumatic valve that start the oxidizer flow in combustion chamber and a fluid parameters pick-up point (temperature and pressure).

A thermal blanket that cover the tank is used to heat up the oxidizer to the desired temperature, $25°C$.

All the components described before are mounted on a steel plate, connected to a test bench using a linear guide that permits the movement in the motor axis direction. This is used to measure the thrust, with a load cell fixed between the

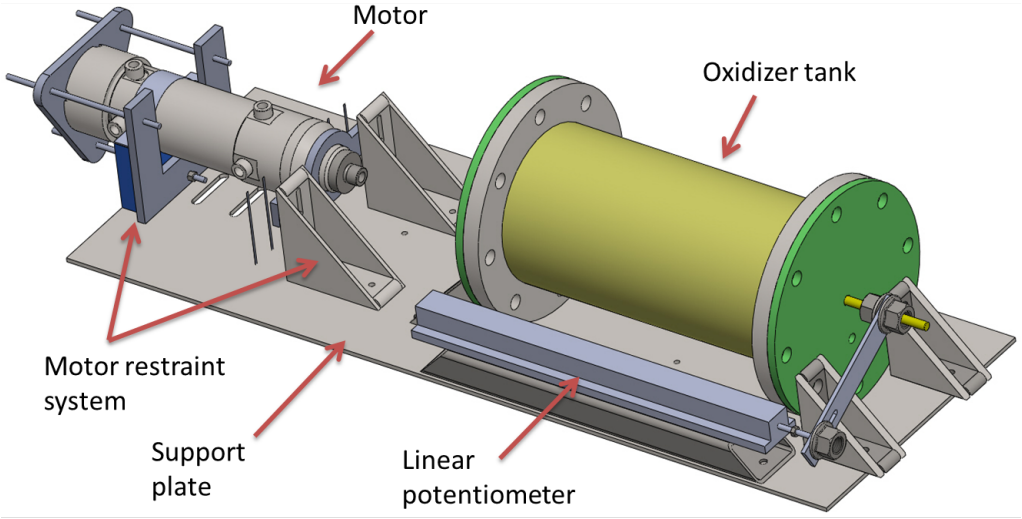

Figure 6.4: Test bed configuration

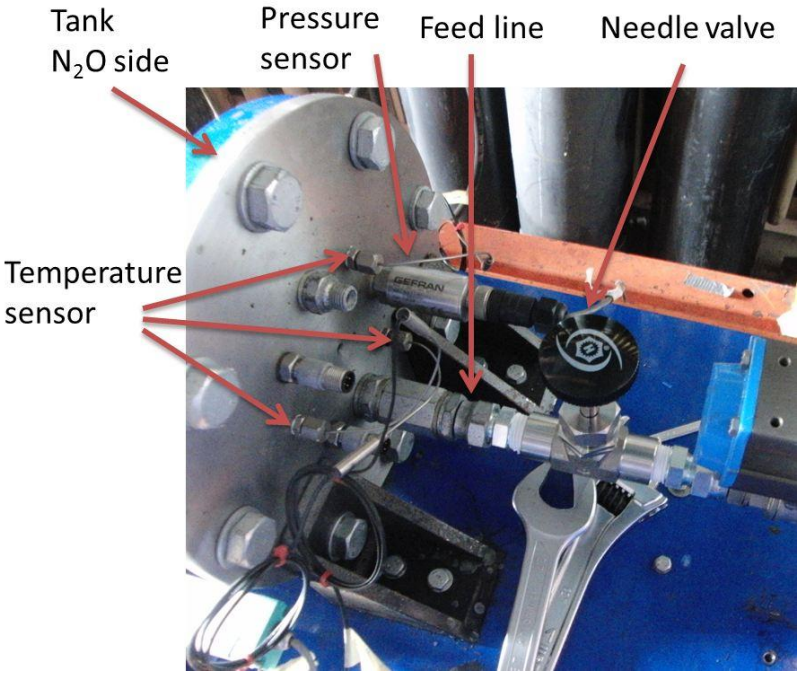

Figure 6.5: Tank sensors

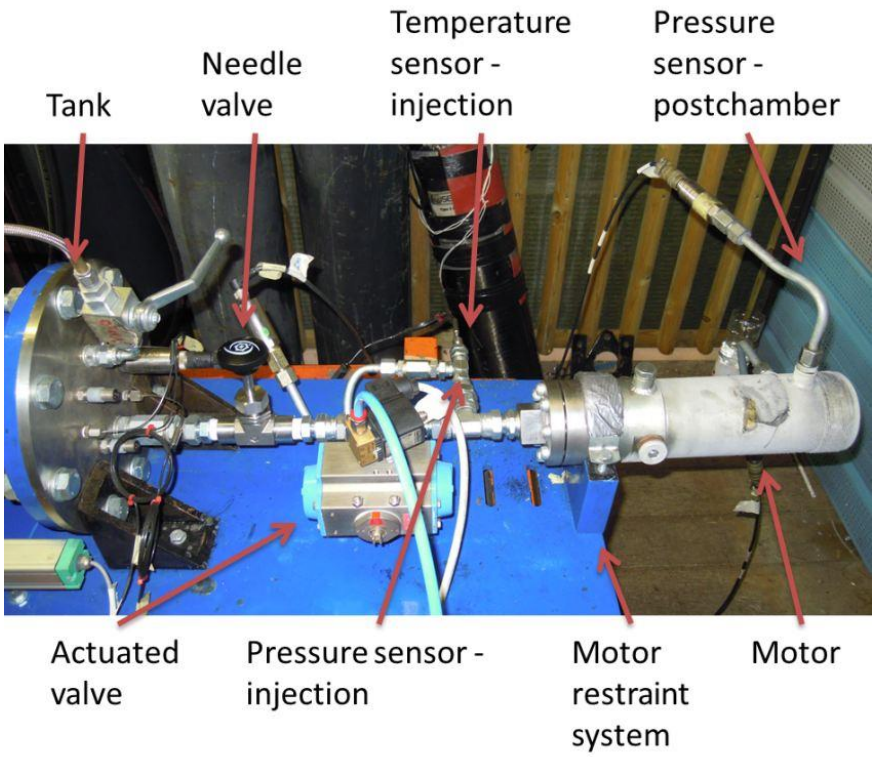

Figure 6.6: Feed line

metallic plate and the test bench.

Test schedule is defined mainly by 2 events: start of the igniters and oxidizer valve opening. There is a delay of 3.5s between the two events.

The test procedure, similar for all tests, was the following:

1. components cleaning;
2. measure of grain data (dimensions, mass);
3. oxidizer tank filling;
4. oxidizer thermalization (80bar and 298K);
5. burn test procedure;
6. measure of grain data after burn (dimensions, mass);

6.2 Measurement system

The most important part in a test is the measurement system. First, to design it, a precise knowledge of the parameters that influence the motor is needed.

A characteristic of an hybrid motor is that many different ambient are present at a very close distance. For example, there is the need to measure pressure in tank, feed line and combustion chamber. All these have its own peculiarities: for example pressure must be measured both in tank at near ambient temperature and in chamber at $2000K \div 3000K$. In this view, sensor choice is an important task.

In this thesis the purpose is to measure the influence of vortex injection, and compare it with axial. To achieve this results, the following parameters have taken into account:

1. chamber pressure;
2. chamber pressure oscillations (instability);
3. oxidizer mass flow;
4. combustion efficiency;
5. regression rate;

Moreover, test bench permits the measurement also of thrust and specific impulse.

A video camera was placed behind the rocket, to record every burn. Another one, but with high speed recoding capabilities (420fps), was placed aside from the nozzle, to record the plume.

All data is acquired thanks to a PLC system from Beckhoff with a frequency of 1kHz. This value was selected due to the pressure frequency range, that gives important informations in the interval 0÷400 Hz. Digitalization has been performed at 16bit. Measuring accuracy of the input channels is less than 0.3% on full scale value.

All selected instruments are temperature compensated in the range (at least) $-10 \div 80°C$, that means that at ambient temperature no thermal problems must be taken into account, except those give by the fluid contact.

Uncertainty for the majority of the parameters is derived from Kline McClintock equation [20] reported in chap.5.2, eq.5.4.

With that formula is possible to evaluate the uncertainty of a measure; rearranging it, follows the relative error, recalling that y is the dependent variable, functions on x_i independent (not correlated) variables with $i = 1 \dots N$:

$$E_y = \frac{i_y}{|y|} = \frac{1}{|y|}\left[\sum_{i=1}^{N}\left(\frac{dy}{dx}i_y\right)^2\right]^{1/2} = \left[\sum_{i=1}^{N}\left(\frac{dy}{dx}\frac{x}{y}\frac{i_y}{x}\right)^2\right]^{1/2} = \left[\sum_{i=1}^{N}\left(\frac{dy}{dx}\frac{x}{y}E_y\right)^2\right]^{1/2} \tag{6.1}$$

It is important to notice that eq.5.4 and 6.1 are first order approximations, and are valid as long as all x_i variables are independent.

The previous discussion is valid for dependent variables, as mass flow or regression rate. In case of direct measurement, like pressure and temperature, there are 2 type of uncertainties [1]:

- type A: uncertainty is evaluated using statistical methods (ex. Gaussian distribution);
- type B: uncertainty is evaluated in other non statistical methods, like it's declared on the manufacturer datasheet.

All uncertainties declared in this thesys have a cover factor of 3, that when a gaussian distribution is considered means an accuracy of 99.7%.

All sensors are digitalized at 16bit, that give rise to an uncertainty evaluated with the following formula:

$$i_{digit} = \frac{FS}{2^n - 1} \tag{6.2}$$

where FS is the full scale value and n is the number of bits. The use of this equation makes implicit the assumption for the number representation: no bits are used for sign, neither the number is divided in exponent and mantissa.

6.2.1 Pressure

Pressure is measured in three zones: tank, injection and combustion chamber.

In tank its interesting frequency range is within $1 \div 10$Hz; from its knowledge is derived the density of the oxidizer that enters the motor. Full scale level is 100bar, beacause the operative design pressure is 80bar. The model chosen is from Gefran, model TK, full scale 100bar, accuracy 0.25% FSO, response time less than 1ms.

In injection, the purpose is to measure the pressure difference with tank and chamber, and so calculate flow coefficient for both needle valve and injection system. It has been reported from other laboratories that N_2O spontaneous decomposition may occur in feed lines in case of impurities or other ignition sources [3].

Other case of dangerous sudden pressure rise are hard start in combustion chamber. In this case it is important to have a quick (1ms) response time sensor, to better identify the source of the problem looking at the phase shift of he pressure peak between two different sensors positions (e.g. chamber and injection). Also here, as in previous case, the choice for the sensor is a Gefran, model TPSA, full scale 100bar, accuracy 0.1% FS, response time less than 1ms, placed between the electro-pneumatic valve and the injection.

In combustion chamber, it is important to have fast sensors (less that 1ms of response time). Pressure range upper limit is about $30 \div 40$bar, depending of the motor configuration. What is very important is that in this ambient temperature will rise very sudden up to 2000K.

For this zone, the chosen sensors are two piezoresistive pressure transducer from Kistler, model 4260A, full scale 70bar, accuracy 0.1%, response time less than 1ms, both placed in the post-chamber zone.

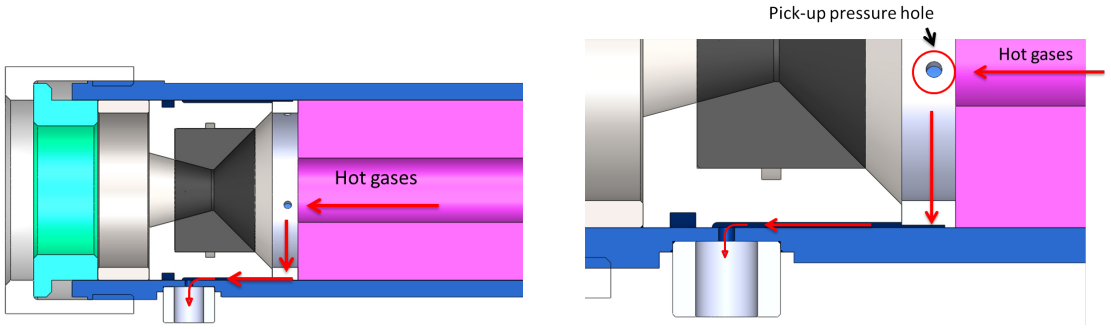

(a) Flow path (b) Flow path - detail

Figure 6.7: Post-chamber pressure pick-up

In fig.6.7 there is a detail on how pressure is measured in post-chamber. A ring (see fig.6.8) is placed before the nozzle; in this device, 4 holes permit the fluid to go in the outer part of the nozzle, where a clearance of 1mm in diameter has been machined.

In this way it is possible to move the nozzle to change the motor configuration (see chap.2.3) without modifying the pressure sensor adapter position.

The position of this pick-up point is chosen at the end of the combustion chamber because in this zone the pressure difference induced by vortex flow (see chap.3.3) analyzed also with the use of CFD is negligible in all configurations (¡0.1%).

Between pressure sensors in combustion chamber and their respective interface

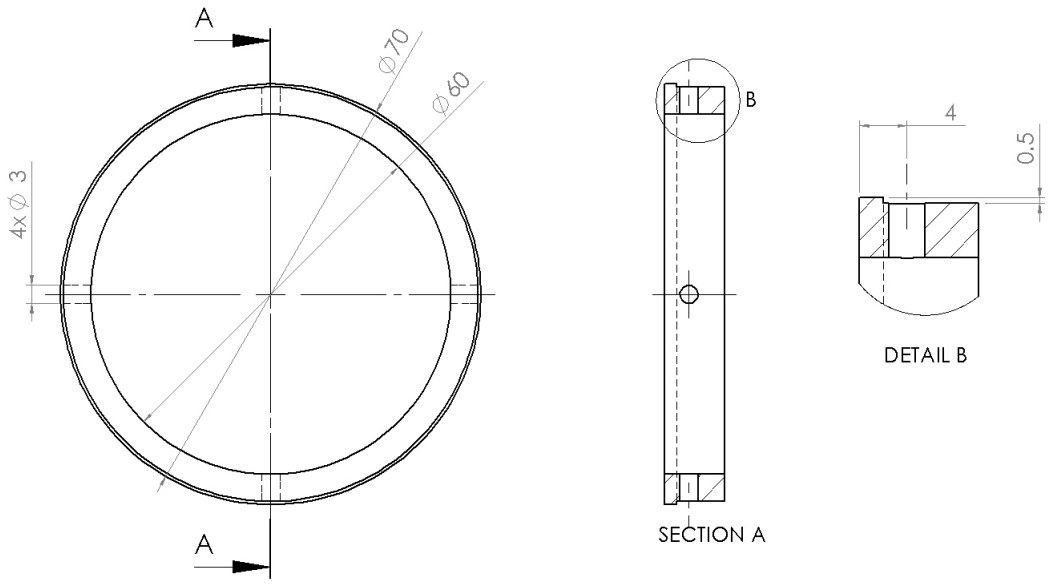

Figure 6.8: Pressure pick-up ring (dimensions in mm)

has been placed a tube filled with water, to protect them against high temperature flow. Post-processing FFT of the signal proved, according to theory, that in this way no elements of the signal were filtered by the liquid medium in comparison with the tube filled with air.

For this instruments, uncertainty is of type B, and is given by manufacturer and data acquisition system datasheet:

- tank: 0.4bar
- injection: 0.3bar
- combustion chamber: 0.2bar

6.2.2 Temperature

Temperature is measured in tank in 3 points (see chap.6.1). It's value is used together with pressure data to obtain N_2O density.

Another point is in injection: it is important to know if temperature is out of range $(-10 \div +80°C)$ of pressure sensors.

All sensors are thermocouple type J, with a metallic sheath. This sheath is necessary to assure sealing, due to the high pressure (up to 100bar) of the fluid.

The accuracy of these sensors are class 2, that means an accuracy of $\pm 2.5K$.

Temperature uncertainty derives from manufacturer datasheet and data acquisition system accuracy. Its maximum value is 4K.

6.2.3 Mass flow

Mass flow is an important value for all following parameters.

Its measure is derived from 3 sources, all related to tank:

- pressure;
- temperature;
- volumetric mass flow.

Density is derived from interpolation of NIST data [2]; input parameters are pressure and temperature.

Uncertainty on density is not straightforward, because there is not a explicit function that gives its value. To perform this task, the dithering method [11] has been used: starting from equation 5.4, derivatives are evaluated numerically (with central difference scheme) using the same calculus program that give the true value. For example, if i_p is the uncertainty of the pressure measurement, p its value, ρ the density value and T the temperature:

$$\frac{\partial p}{\partial \rho} = \frac{\rho(p - i_p, T) + \rho(p + i_p, T) - 2\rho(p, T)}{2i_p} \tag{6.3}$$

In the above equation, $\rho(p, T)$ means that density is evaluated with the value p for pressure and T for temperature.

This method is commonly used when no other indication can be given on uncertainty, but is very time-consuming if the run-time of the program is very long, because at least 2 runs per each variable must be done.

Evaluated both temperature and pressure derivatives, density uncertainty is computed:

$$i_\rho = \left[\left(\frac{\partial p}{\partial \rho} i_p \right)^2 + \left(\frac{\partial T}{\partial \rho} i_T \right)^2 \right]^{1/2} \tag{6.4}$$

With this methodology, the density uncertainty value is $5 kg/m^3$.

Uncertainty single terms analysis have been performed as following: each single terms in eq.6.4 gives the uncertainty influence:

$$h_{y,x_i} = \frac{\partial y}{\partial x_i} i_{x_i} \tag{6.5}$$

For each term, relative uncertainty influence is the following:

$$j_{y,x_i} = \left[\frac{\left(\frac{\partial y}{\partial x_i} i_{x_i} \right)^2}{\sum_{k=1}^{N} \left(\frac{\partial y}{\partial x_k} i_{x_k} \right)^2} \right] = \left(\frac{h_{y,x_i}}{i_y} \right)^2 \tag{6.6}$$

In table 6.1 details of uncertainty calculations for density have been reported.

Table 6.1: Density uncertainty detail

Variable	Unit	Value	Uncertainty	Rel. unc.	Influence	Rel. infl.
Pressure	bar	80	0.4	0.5%	7.04E-03	0.1%
Temperature	K	298	4	1.3%	4.9	99.9%
Density	kg/m3	796	5	0.6%		

It can be seen that the relative influence to density uncertainty of presure is negligible respect to temperature.

Volumetric mass flow is derived from potentiometer measurement of piston position and knowledge of tank internal dimensions.

Potentiometer is a device that measure a linear relative motion [12]. The instrument selected is a resistive potentiometer, from Gefran, model PC with a total run (full scale) of 400mm. It offers a linearity error of ±0.05% on full scale.

As for pressure and temperature, uncertainty has been evaluated, and its value is of 1.2mm.

Mass flow formula is (v is piston velocity, A is piston area):

$$\dot{m} = vA\rho \tag{6.7}$$

Its uncertainty, therefore, is:

$$i_{\dot{m}_{ox}} = \left[\left(\frac{\dot{m}_{ox}}{v} i_v \right)^2 + \left(\frac{\dot{m}_{ox}}{A} i_A \right)^2 + \left(\frac{\dot{m}_{ox}}{\rho} i_\rho \right)^2 \right]^{1/2} \tag{6.8}$$

Area and its uncertainty are (ϕ is the tank diameter):

$$A = \frac{\pi}{4}\phi^2 \tag{6.9}$$

$$i_A = \frac{\pi}{2}\phi \tag{6.10}$$

Piston velocity equation (ΔL is the piston travel) is:

$$v = \frac{\Delta L}{\Delta t} \tag{6.11}$$

Uncertainty is:

$$i_v = \left[\left(\frac{1}{\Delta t} i_{\Delta L} \right)^2 + \left(\frac{\Delta L}{\Delta t^2} i_{\Delta t} \right)^2 \right]^{1/2} \tag{6.12}$$

In tab.6.2 numerical data (using typical experimental activity values) is reported for piston velocity uncertainty. For influence and relative influence, refer to eq.6.5 and 6.6.

Table 6.2: Piston velocity uncertainty detail

Variable	Unit	Value	Uncertainty	Rel. unc.	Influence	Rel. infl.
Time	s	3.00	0.01	0.3%	0.08	3.5%
Piston travel	mm	69.9	1.2	1.7%	0.41	96.5%
Piston speed	mm/s	23.3	0.6	2.5%		

It can be seen that the major uncertain source is due to the piston travel measured by potentiometer.

In tab.6.3 a summary of mass flow uncertainty analysis is reported. Data are typical value reported in experimental activities.

Table 6.3: Oxidizer mass flow uncertainty summary

Variable	Unit	Value	Uncertainty	Rel. Uncertainty
Pressure	bar	80	0.4	0.5%
Temperature	K	298	4	1.3%
Density	kg/m3	796	5	0.6%
Tank diameter	mm	160.0	0.1	0.1%
Piston area	mm2	20106	25	0.1%
Time	s	3.00	0.01	0.3%
Piston travel	mm	69.9	1.2	1.7%
Piston speed	mm/s	23.3	0.6	2.5%
Mass flow	g/s	351	9	2.5%

Table 6.4: Mass flow uncertainty detail

Variable	Unit	Value	Uncertainty	Rel. unc.	Influence	Rel. infl.
Piston area	mm2	20106	25	0.1%	0.44	0.5%
Density	kg/m3	796	5	0.6%	1.87	8.3%
Piston speed	mm/s	23.3	0.6	2.5%	6.226	91.28%
Mass flow	g/s	351	9	2.5%		

In tab.6.4 details on mass flow uncertainty are shown. It can be seen that the major source of uncertainty is the piston speed: this is common, because the computation of velocity is a derivative, and it is well known that this kind of operators enhance uncertainty. Going back to tab.6.2, piston travel (and so potentiometer) is the main causes of uncertainty in the measurement of oxidizer mass flow.

6.2.4 Regression rate

Regression rate is the measure of the velocity of the burning surface of the grain. What follows will have the implicit assumption that the grain shape is a hollow cylinder, burning from inside. One of the main purposes of this study is to enhance this value.

Following [16], space-time averaged regression rate formula is:

$$\bar{\dot{r}} = \frac{\phi_f - \phi_i}{2t_b} \tag{6.13}$$

where $\bar{\dot{r}}$ is the mean regression rate value, ϕ_f and ϕ_i are final and initial grain internal diameter and t_b is the burning time.

Final diameter is evaluated by measuring grain mass at the end of the burning, and comparing it with initial data:

$$\phi_f = \left(\phi_i^2 + \frac{4\Delta M}{\pi \rho_f L_g}\right)^{1/2} \tag{6.14}$$

with ΔM burned mass, L_g grain length, ρ_f fuel density.

In this equation there is the assumption that the final shape of the internal void space is still a perfect cylinder. This is usually not true, and is highly dependent on injection type. In fig.6.9 are showed 2 paraffin grains after a burn test of 3s [7] with two different type of injection, one axial and one mixed axial-tangential. It can be observed that in the injection side there is a higher consumption of the grain.

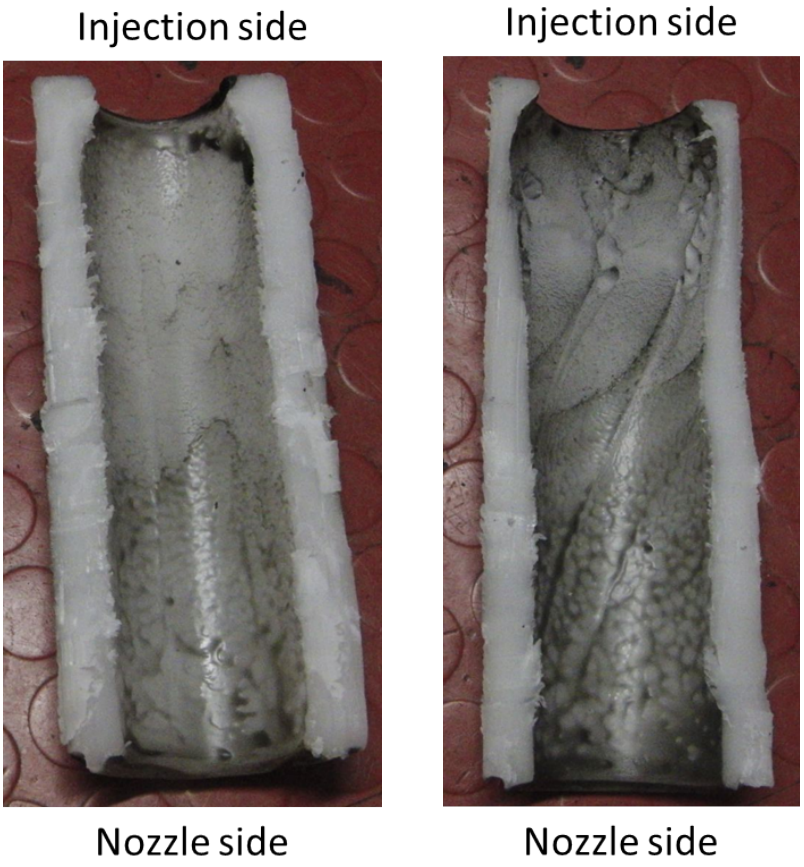

(a) Axial injection

(b) Mixed axial-tangential injection

Figure 6.9: Grain erosion

Previous formulation is useful in test data analysis. To design a motor, instead, another equation that takes into account different parameters is used:

$$\bar{\dot{r}} = a{G_{ox}}^{n} \tag{6.15}$$

where G_{ox} is the mean oxidizer flux on port area (defined by grain inner diameter):

$$G_{ox} = \frac{16\dot{m}_{ox}}{\pi(\phi_i + \phi_f)^2} \tag{6.16}$$

Here, a and n are coefficient determined experimentally. Typical values [7] are:

- a=0.19mm/s : axial injection;
- n=0.5 : paraffin fuel.

n depends usually on fuel-oxidizer mixture (e.g. $HTPB/H_2O_2$ n value is between 0.62 and 0.68), while a on motor configuration (injection type, use of devices inside combustion chamber).

Rearranging eq.6.16, we have:

$$a = \frac{\bar{\dot{r}}}{G_{ox}^{n}} \tag{6.17}$$

Due to too low number of tests, it wasn't possible to evaluate both regression rate coefficients, a and n; a supposed $n = 0.5$ was used in this calculation. This number comes out from the observation of the chamber pressure during the burn, that remains constant when the mass flow is constant. Moreover, this is also a typical value for the combination of N_2O/paraffin hybrid rockets [31].

Previous formulation requires a constant condition in combustion chamber; chamber pressure and flame behaviour do not respond with a step function when oxidizer valve is closed. This is more clear in fig.6.10.

To take into account also this phenomenon, a thrust termination effect correction has been used in regression rate formulation [16], to have a more precise value for previous values.

Valve closure effect can be discovered using the derivative of pressure and mass flow data. From this point (valve closing effect) up to the end burning (null pressure in chamber), pressure data is fitted with an exponential law:

$$p_{fit} = p_0 e^{-t/\tau_c} \tag{6.18}$$

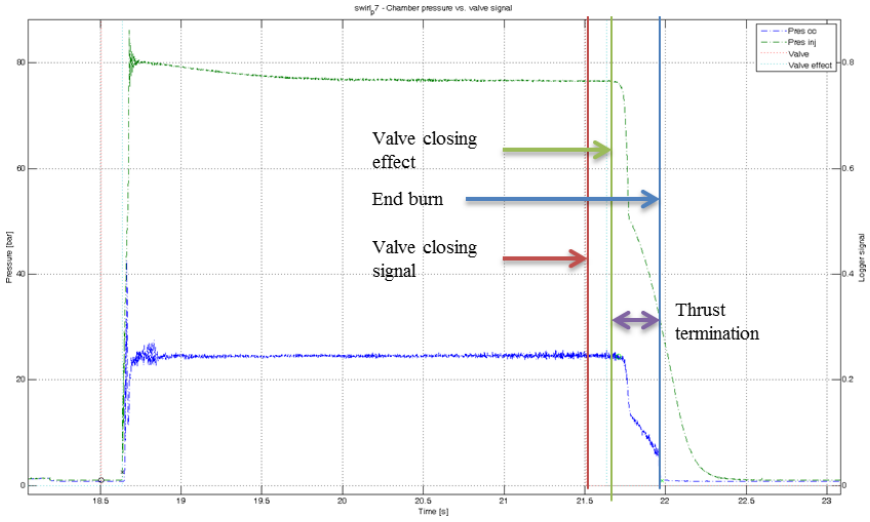

Figure 6.10: Thrust termination effect

p0 is evaluated as the average of the last 0.2s of the chamber pressure before valve closing effect. A typical value of τ_c is 0.15s, but in our algorithm has been evaluated at each burn. An iterative method (in following formulas, i is the iteration number) is used to obtain new values for oxidizer mass flux, end diameter, regression rate and its a coefficient.

$$G_{ox,i} = \frac{16\dot{m}_{\mathrm{ox}}}{\pi(\phi_{f,i-1} + \phi_i)^2} \tag{6.19}$$

$$\phi_{f,i} = \left[\frac{2n+1}{n} \frac{2^{n+1}}{\pi^n} \tau_c a_{i-1} m_{ox}^n \left(e^{-n\frac{t}{\tau_c}} - 1 \right) + \phi_{f,i-1}^{2n+1} \right]^{\frac{1}{2n+1}} \tag{6.20}$$

$$\bar{\dot{r}}_i = \frac{\phi_{f,i} - \phi_i}{2t_{b,eff}} \tag{6.21}$$

$$a_i = \frac{\bar{\dot{r}}_i}{G_{ox,i}^n} \tag{6.22}$$

Here, $t_{b,eff}$ is the burn time corrected for the thrust termination effect.

Uncertainty analysis using Kline McClintock formula (eq.5.4) gives the following equations:

$$i_{\phi_f} = \left[\left(\frac{\phi_{\mathrm{i}}}{\phi_{\mathrm{f}}} i_{\phi_i} \right)^2 + \left(\frac{2}{\pi\rho L_g \phi_e} i_{\phi_{\mathrm{M_f}}} \right)^2 + \left(\frac{2\mathrm{M_f}}{\pi\rho^2 L_g \phi_e} i_{\phi_\rho} \right)^2 + \left(\frac{2\mathrm{M_f}}{\pi\rho L_g^2 \phi_e} i_{\phi_{\mathrm{Lg}}} \right)^2 \right]^{1/2} \tag{6.23}$$

$$i_{\dot{r}} = \left[\frac{i_{\phi_i}^2 + i_{\phi_f}^2}{4t_b^2} + \left(\frac{\dot{\mathrm{r}}}{t_b} i_{\mathrm{t_b}} \right)^2 \right]^{1/2} \tag{6.24}$$

$$i_{G_{ox}} = \left[\left(\frac{2G_{ox}}{\phi_f + \phi_i} \right)^2 \left(i_{\phi_i}^2 + i_{\phi_f}^2 \right) + \left(\frac{G_{ox}}{\dot{m}} i_{\dot{m}} \right)^2 \right]^{1/2} \tag{6.25}$$

$$i_a = \left[\left(\frac{a}{\dot{r}} i_{\dot{r}} \right)^2 + \left(\frac{n\dot{r}}{G_{ox}^{n+1}} i_{G_{ox}} \right)^2 + \left(\frac{\ln(G_{ox})\dot{r}}{G_{ox}^n} i_n \right)^2 \right]^{1/2} \tag{6.26}$$

To evaluate uncertainties with previous equations, basic data must be know, reported in table 6.5.

Table 6.5: Regression rate basic uncertainties

Variable	Unit	Symbol	Uncertainty
Initial grain diameter	mm	ϕ_i	0.1
Grain burned mass	g	ΔM	2
Grain length	mm	L_g	0.1
Burning time	s	t_b	0.1
Grain density	$\frac{kg}{m^3}$	ρ_g	4
n exponent		n	0.01

6.2.5 Combustion efficiency

Evaluation of combustion efficiency start from isentropic equations [28].

$$\dot{m} = \frac{A_t p_0}{\sqrt{T_0}} \sqrt{(\frac{\gamma}{R} \left(\frac{\gamma+1}{2} \right)^{\frac{\gamma+1}{2(\gamma-1)}}} = \frac{A^* p_0}{\sqrt{\gamma R T_0}} \Gamma \tag{6.27}$$

Eq.6.27 relates mass flow $\dot{m}$ to chamber total temperature T_0 and pressure p_0, nozzle throat area A_t and fluid mixture properties (R si the gas constant and γ is the ratio of specific heat at constant pressure and volume).

Noting that $a_0 = \sqrt{\gamma R T_0}$ is the speed of sound in combustio chamber, eq.6.27 can be rearranged in:

$$\dot{m} = \frac{\Gamma}{a_o} p_o A_t \tag{6.28}$$

Characteristic exhaust velocity is defined with the following equation:

$$c^* = \frac{a_o}{\Gamma} \tag{6.29}$$

Rearranging eq.6.28 and 6.29 we arrive at:

$$c^* = \frac{p_0 A_t}{\dot{m}} \tag{6.30}$$

Uncertainty analysis comes from each parameter definition. For fuel mass flow is the following:

$$\dot{m}_{fuel} = \frac{\Delta M}{t_b} \tag{6.31}$$

$$i_{\dot{m}_{fuel}} = \left[\left(\frac{m_{fuel}}{\Delta M} i_{\Delta M} \right)^2 + \left(\frac{m_{fuel}}{t_b} i_{t_b} \right)^2 \right]^{1/2} \tag{6.32}$$

Table 6.6: Fuel mass flow uncertainty analysis

Variable	Unit	Value	Uncertainty	Rel. unc.	Influence	Rel. infl.
Burned fuel mass	g	320	4	1.3%	1.3	93.3%
Burning time	s	3.00	0.01	0.3%	0.4	6.7%
Fuel mass flow	g/s	107	1	1.3%		

In tab.6.6 numerical values are presented for fuel mass flow uncertainty, with typical experimental values. It can be seen that the major uncertainty source is derived from the burned fuel mass measurement.

Total mass flow equations are the following:

$$\dot{m}_{tot} = \dot{m}_{fuel} + \dot{m}_{ox} \tag{6.33}$$

$$i_{m_{tot}} = \left[i_{m_{fuel}}^2 + i_{m_{ox}}^2 \right]^{1/2} \tag{6.34}$$

Experimental values and numerical uncertainty are reported in tab. 6.7. Here, oxidizer mass flow is the most important parameter, because it has a high influence on the measure.

Combustion efficiency uncertainty is defined as:

$$i_{c^*} = \left[\left(\frac{c^*}{p_c} i_{p_c} \right)^2 + \left(\frac{c^*}{A_t} i_{A_t} \right)^2 + \left(\frac{c^*}{\dot{m}_{tot}} i_{\dot{m}_{tot}} \right)^2 \right]^{1/2} \tag{6.35}$$

Table 6.7: Total mass flow uncertainty analysis

Variable	Unit	Value	Uncertainty	Rel. unc.	Influence	Rel. infl.
Oxidizer mass flow	g/s	351	7	1.9%	6.5	95.7%
Fuel mass flow	g/s	107	1	1.3%	1.4	4.3%
Total mass flow	g/s	458	7	1.5%		

In tab.6.8 details on numerical values for uncertainty analysis of characteristic velocity are reported. It can be see that the total mass flow gives the most of the uncertainty.

Table 6.8: Characteristic velocity uncertainty analysis

Variable	Unit	Value	Uncertainty	Rel. unc.	Influence	Rel. infl.
Nozzle throat diameter	mm	16.00	0.05	0.3%		
Nozzle throat area	mm2	201	1	0.6%	8.2	11.1%
Chamber pressure	bar	30.0	0.3	1.0%	13.2	28.5%
Total mass flow	g/s	458	7	1.5%	19.2	60.3%
Characteristic speed	m/s	1317	25	1.9%		

Summarizing previous tables, the most important measure is the oxidizer mass flow.

To calculate theoretical combustion efficiency, we adopted an external program (CProPep). Input parameters are O/F ratio, total mass flow, exit and throat diameter. Again, dithering method is the chosen uncertainty tool.

O/F ratio value and uncertainty use the following equations:

$$\frac{O}{F} = \frac{\dot{m}_{ox}}{\dot{m}_{fuel}} \tag{6.36}$$

$$i_{O/F} = \left[\left(\frac{O/F}{\dot{m}_{fuel}} i_{\dot{m}_{fuel}} \right)^2 + \left(\frac{O/F}{\dot{m}_{ox}} i_{\dot{m}_{ox}} \right)^2 \right]^{1/2} \tag{6.37}$$

Numerical values with experimental data are reported in table 6.9

Combustion efficiency equations are the following:

$$\epsilon_c^* = \frac{c^*}{c^*_{theo}} \tag{6.38}$$

Table 6.9: O/F ratio uncertainty analysis

Variable	Unit	Value	Uncertainty	Rel. unc.	Influence	Rel. infl.
Oxidizer mass flow	g/s	351	7	1.9%	0.06	68.0%
Fuel mass flow	g/s	107	1	1.3%	0.04	33.8%
O/F ratio		3.29	0.07	2.2%		

$$i_{\varepsilon_{c^*}} = \left[\left(\frac{\varepsilon_{c^*}}{c^*} i_{c^*} \right)^2 + \left(\frac{\varepsilon_{c^*}}{c^*_{theo}} i_{c^*_{theo}} \right)^2 \right]^{1/2} \tag{6.39}$$

where c^* is the measured value and c^*_{theo} is the theoretical value, calculated from thermo-chemistry data.

Values with burn test are reported in table 6.10.

Table 6.10: Combustion efficiency uncertainty data

Variable	Unit	Value	Uncertainty	Rel. unc.	Influence	Rel. infl.
Theor. c^*	m/s	1387.1	0.16	0.01%	0.0001	0.0036%
Meas. c^*	m/s	1317	24.7	1.87%	0.018	99.9427%
Comb. Efficiency	%	94.97	0.02	1.87%		

Analysis of values shows a great dependency to measurement data respect to theoretical values.

6.2.6 Thrust and specific impulse

Motor thrust is measured with a load cell linked between the support plate (see fig.6.4) and the ground fixed test bench in fig.6.11.

Axial movement is permitted by two linear guides. Measure is performed by a load cell from Laumas, model CTOL, 300kg of full scale, with an accuracy of 0.03% on full scale. Combined with acquisition system accuracy, it gave a 0.3% uncertainty on measurement, that reported to the instrument full scale is 9N.

It has to be noted, however, that in this thesis thrust measurement has not been taken into account for configurations comparison. The explanation is that

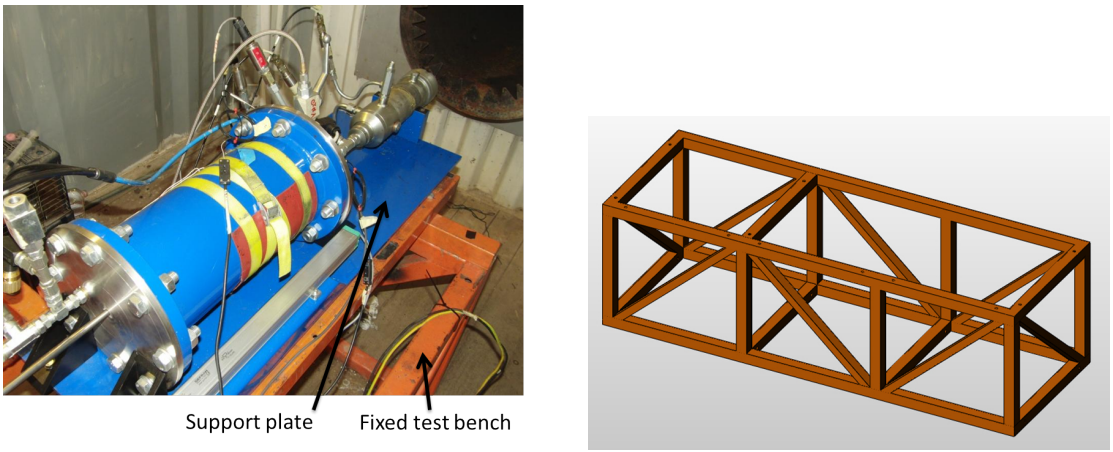

(a) Connection (b) Ground fixed component

Figure 6.11: Test bench for thrust

there are many uncertainty in this system that enter in the measurement chain that has not been treated and analyzed; the major are:

- structural vibrations in ground fixed test bench and in motor system;
- depressurization in the facility.

In particular, the last elements has an influence on comparing the thrust model (using isentropic nozzle equations) with measured data. The problem is that due to neighbourhood reasons the motor is inside a container, and the exhausts are directed to a silencer system. This produce a depressurization inside the container that modify the ambient pressure.

Specific impulse (I_{sp}) is derived from thrust (T) measurement:

$$I_{sp} = \frac{T}{\dot{m}_{tot} g_0} \tag{6.40}$$

where $\dot{m}_{tot}$ is the total (both oxidizer and fuel) mass flow, and g_0 is the standard gravity acceleration (9.80665 m/s^2).

6.3 Results

The experimental campaign followed a 3 aims investigation purpose:

1. comparison between axial and vortex injection;
2. throttling behaviour;

3. performance variation with different combustion chamber devices.

For each test, the main focused parameters are:

- pressure behaviour (trend, oscillations and instabilities);
- regression rate;
- combustion efficiency.

In every following table and chart 8 groups have been analyzed:

1. axial;
2. vortex at full throttle with 5mm and 10mm (basic case) of post-chamber;
3. vortex at 75% throttle with 17mm and 10mm of pre-chamber;
4. vortex at 50% throttle with 17mm and 10mm of pre-chamber;
5. mixer.

In every table, every case will have 3 rows for parameter: one with value, then its uncertainty and its relative uncertainty.

6.3.1 Test overview

Test campaign has seen a total of 51 tests, comprises both hot (burning) and cold (no ignition, only oxidizer discharge).

First part had the purpose to characterize the injector discharge and throttling valve performance (this last aspect reported in chap.5). Two tests have been performed, with no combustion chamber mounted in the test bed for both axial and vortex injector.

Oxidizer mass flow is reported in fig.6.12). A similar trend in mass flow discharge is a very important result because in this way one variable in combustion chamber is fixed without adjusting tank pressure.

Tab.6.11 gives numerical results. Again, it can be seen that performance of both injection devices are very similar in terms of mass flow and discharge coefficient. Cv data have been obtained with an analysis similar to what reported in 5.2.

It has to be noticed, however, that these values are obtained with a very high pressure difference: 80bar. The particular oxidizer used (nitrous oxide) has the effect that its behaviour do not depend only on Δp, but also on single pressure

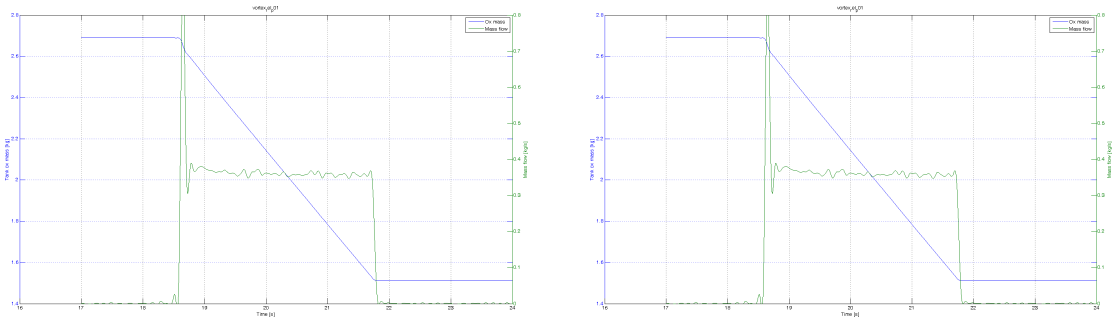

(a) Vortex injection (b) Axial injection

Figure 6.12: Mass flow discharge in cold test

Table 6.11: Cold test results - mass flow and injector discharge coefficient

	Ox mass flow [g/s]	**Cv injection**
Vortex	362	0.194
	7	0.003
	1.9%	1.6%
Axial	362	0.192
	9	0.004
	2.4%	1.9%

value before and (in particular) after injection. Experimental campaign showed that similar results (same discharge) are obtained also during burn tests.

Following step was a study on optimal motor configuration with vortex injection. In particular, we found and solved two different issues:

- pressure regime change during burn;
- ignition overpressure.

The first issue is depicted in fig.6.16.

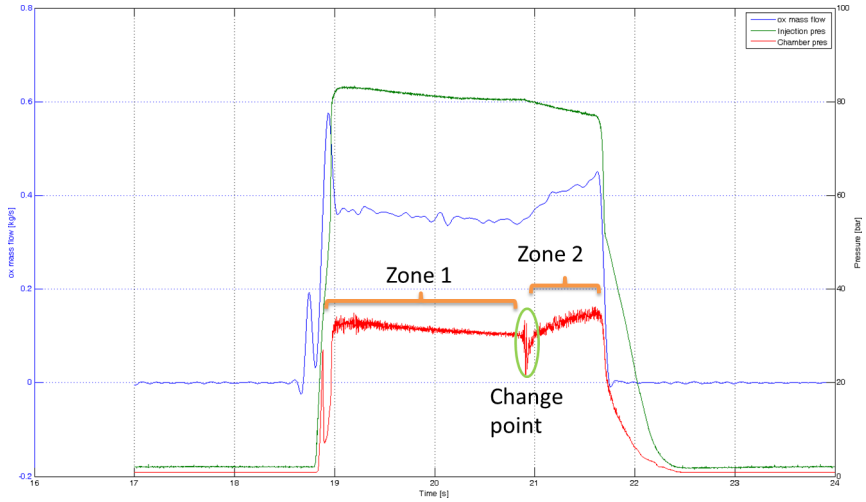

Figure 6.13: Burning issue - change in regime

Pressure profile shows a decay in the first part, and an increase in the second. Both trends correspond to a similar one in mass flow.

In fig.6.14 the spectrogram of the chamber pressure is presented. It can be seen that the second regime zone has a more rough signal, connected with higher instability behaviour. This phenomenon has been linked with long post-combustion chambers.

Ignition overpressure, instead, is connected to both pre-chamber dimensions and pyrotechnic igniter position and quantity (see fig.6.15).

In particular, adding a pre-combustion chamber reduce (if present) the ignition over-pressure. This phenomenon has been measured only in full throttle tests, but not at reduced mass flow.

Final configuration with vortex injection showed a 10mm pre-chamber and a 10mm post-chamber. A similar configuration has been used for axial test.

In tab.6.12 experimental results on mass flow and thrust are presented. As previously noted, mass flow between cold test and burn test is similar. It is not

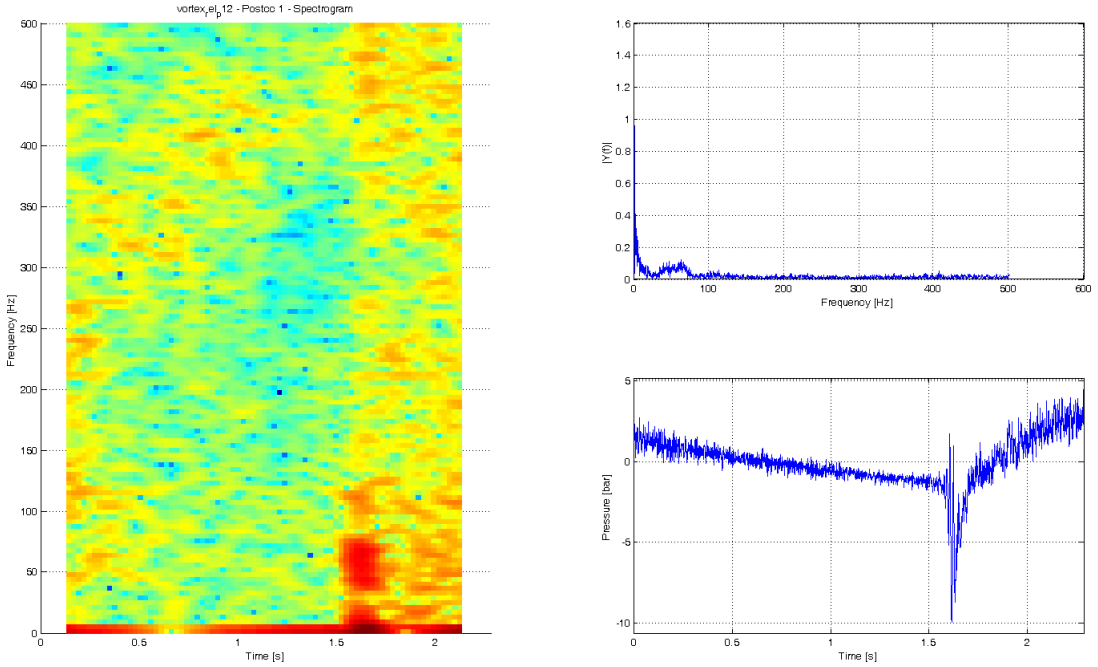

Figure 6.14: Burning issue - spectrogram

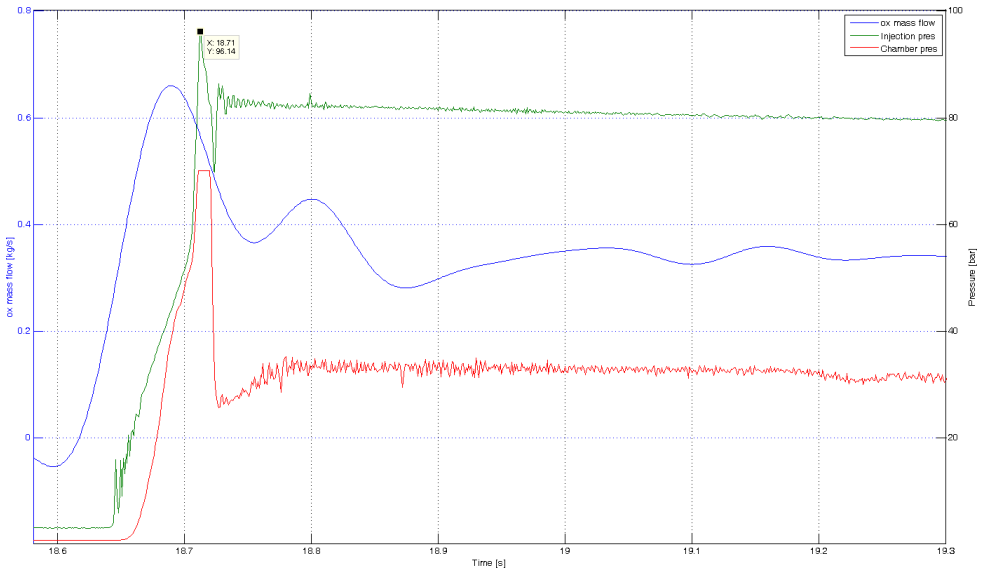

Figure 6.15: Burning issue - overpressure

Table 6.12: Mass flow and thrust data

	Ox mass flow [g/s]	**Fuel mass flow [g/s]**	**O/F**	**Total mass flow [g/s]**	**Thrust [N]**
Axial	373 7.1 1.9%	61 1.2 1.9%	6.4 0.12 1.9%	435 11.8 2.7%	722 27 3.7%
Vortex basic post 5	341 7.6 2.2%	105 1.8 1.7%	3.4 0.06 1.9%	446 12.6 2.8%	777 25 3.3%
Vortex basic	366 8.9 2.4%	109 1.9 1.7%	3.6 0.06 1.7%	475 14.3 3.0%	889 37 4.2%
Vortex 1/4 pre 17	229 5.4 2.4%	79 1.4 1.8%	3.0 0.08 2.7%	308 9.1 3.0%	550 3 0.6%
Vortex 1/4	231 6.7 2.9%	81 1.4 1.8%	2.9 0.08 2.8%	311 10.6 3.4%	481 6 1.2%
Vortex 1/8 pre 17	118 9.4 7.9%	61 1.2 1.9%	1.9 0.10 5.4%	179 14.6 8.2%	398 3 0.9%
Vortex 1/8	127 3.7 2.9%	63 1.2 1.9%	2.1 0.10 4.9%	190 6.7 3.5%	322 4 1.3%
Mixer	367 8.5 2.3%	118 2.0 1.7%	3.3 0.06 1.7%	485 14.0 2.9%	916 19 2.1%

compatible because its value is highly dependent on tank pressure (due to Bernoulli equation), and this had a variation in the order of 4bar between different test.

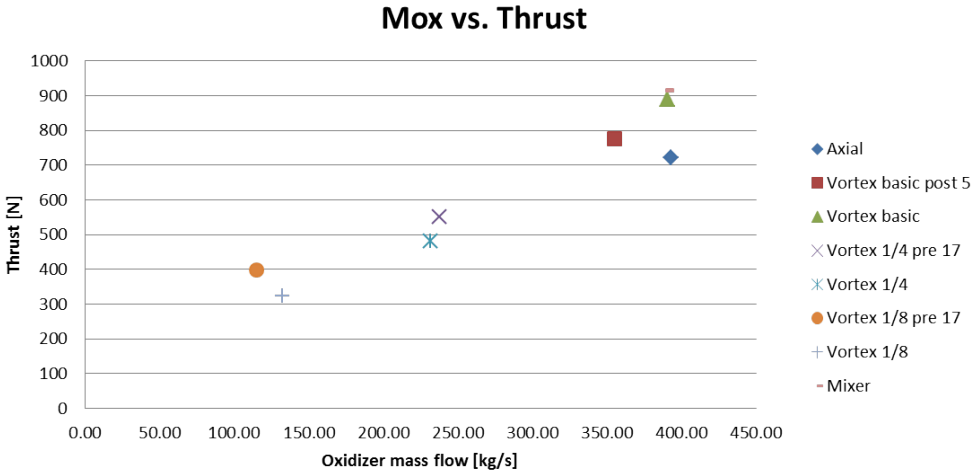

Figure 6.16: Experimental test data - $\dot{m_{ox}}$ vs. thrust

In fig.6.16 oxidizer mass flow and thrust data are compared with different cases. First thing is that there is a linear relationship between mass flow and thrust. This is due to isentropic nozzle equation.

Axial injection gives a lower mean thrust (722N) respect to vortex (889N) because of less regression rate and combustion efficiency. Less regression rate means less total mass that exit through the nozzle. Less combustion efficiency is linked to a lower pressure chamber and mean temperature chamber.

6.3.2 Pressure behaviour

An important thing in an hybrid rocket motor is the pressure behaviour. In particular, pressure oscillations are very dangerous (especially in solid motors) and can cause serious damage. Furthermore, also the thrust is affected, and a stable thrust profile is usually wanted.

In our analysis we separate a stable motor from an unstable one when the pressure oscillations are higher that 5% from the mean pressure.

In table 6.13 numerical values are presented.

Oscillations are evaluated with a linear fitting on pressure measurement within a specified time interval. The standard deviation of the difference of linear value and measured pressure gives the measure of oscillation. Its ratio with mean pressure gives the relative value (see fig.6.17).

Table 6.13: Experimental results: pressure data

	Oscillations [bar] and [%]	**Upper and lower limits [bar]**	**Tank pres [bar]**	**Chamb pres [bar]**	**Dp tank - chamb [bar]**
Axial	2.1 7.5%	24.8 29.2	85.0 1.1 1.2%	27.4 1.5 5.5%	57.6 2.4 4.1%
Vortex basic post 5	1.1 3.8%	31.5 28.9	79.6 0.3 0.4%	29.9 0.9 2.9%	49.7 0.7 1.4%
Vortex basic	1.2 3.8%	34.7 31.2	82.2 0.4 0.4%	33.1 1.8 5.4%	49.1 1.6 3.4%
Vortex 1/4 pre 17	0.3 1.6%	19.5 19.4	79.2 0.1 0.1%	19.5 0.1 0.7%	59.7 0.2 0.3%
Vortex 1/4	0.7 3.9%	19.0 19.0	82.0 0.1 0.2%	18.9 0.3 1.4%	63.1 0.3 0.5%
Vortex 1/8 pre 17	0.2 1.7%	10.0 10.1	79.1 0.2 0.2%	10.0 0.1 0.9%	69.1 0.2 0.3%
Vortex 1/8	0.4 4.1%	10.4 10.5	81.9 0.3 0.3%	10.4 0.2 1.7%	71.5 0.3 0.4%
Mixer	0.4 1.2%	36.2 34.1	83.2 0.2 0.3%	34.9 0.6 1.8%	48.3 0.4 0.9%

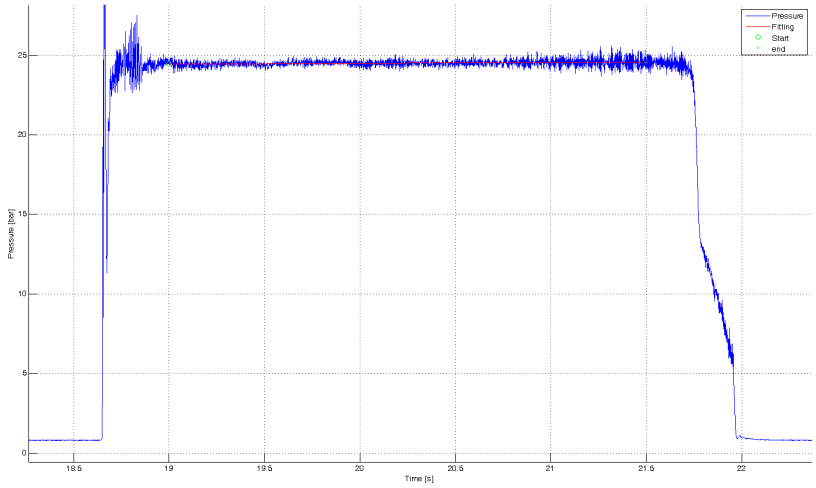

Figure 6.17: Pressure oscillations measurement technique

Results (see fig.6.18) show a reduction in pressure oscillations in combustion chamber from 7.5% with axial injection down to 3.8% with vortex; it has been measured that this value is independent from mass flow.

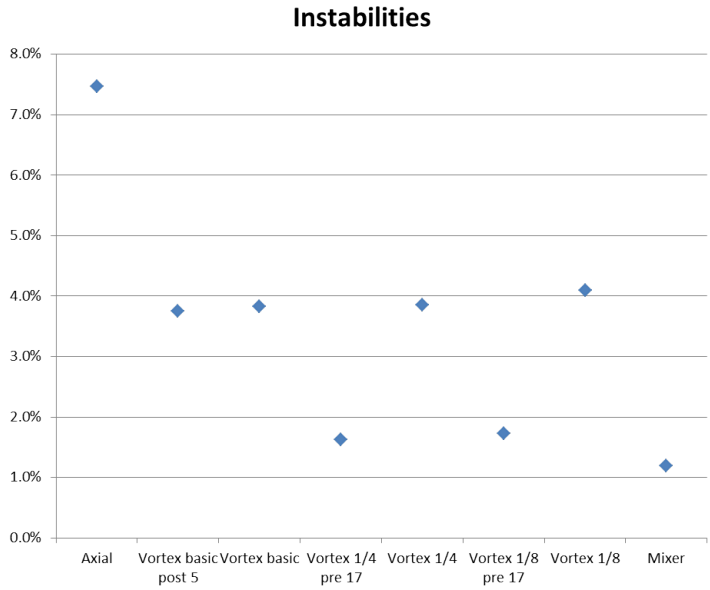

Figure 6.18: Experimental campaign data: pressure oscillations

What comes out, furthermore, is that the use of a shorter post-chamber (5mm against 10mm) do not affect pressure behaviour in terms of instability, while with a longer pre-chamber or a mixer-like device there is a damping to a level of less than 2%.

6.3.3 Regression rate

Regression rate numerical data are reported in tab.6.14.

Chart data are reported in fig.6.19 and 6.20.

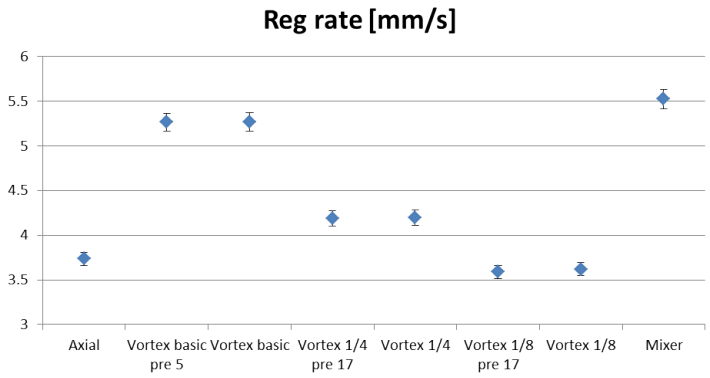

Figure 6.19: Regression rate experimental results

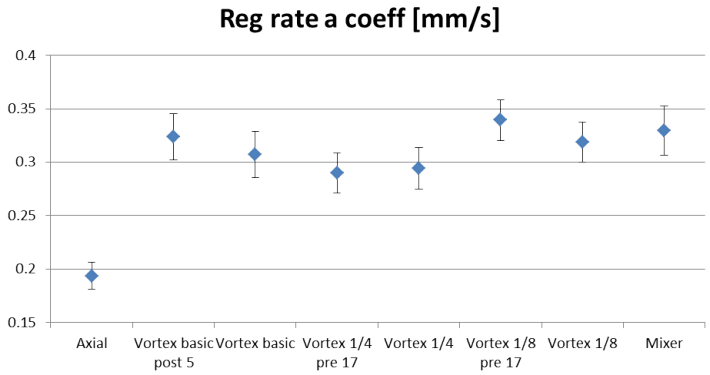

Figure 6.20: Regression rate results - a coefficient [mm/s]

First thing that comes out is that axial injection has a lower regression rate value (3.7mm/s) than vortex (5.3 mm/s) with the same oxidizer mass flow, with an increase ratio of 141% of the last one respect to axial.

Regression rate goes down with throttling, and this is natural due to the lower G_{ox}. The important this is that there is not an higher difference in the a coefficient of the regression rate formula. In axial injection its value is 0.19mm/s, while with vortex injection it remains between $0.29 \div 0.34$ mm/s.

There is not an advantage in the use of a pre-chamber of post-chamber. It can be seen also in fig.6.22 and 6.21 (numerical values in tab.6.15), where a comparison with axial and vortex test is presented.

In tab.6.15 and fig.6.21 and a comparison of experimental data with vortex and axial injection are presented.

Table 6.14: Regression rate data

	Gox [kg / (m2*s]	**Gox at start and end [kg / (s*m2)] and τ [s]**	**Reg rate [mm/s]**	**End diameter [mm]**	**a coef [mm/s]**
Axial	371.9 2.5 0.7%	800 214 0.16	3.73 0.07 2.0%	48.3 0.2 0.4%	0.19 0.01 6.6%
Vortex basic post 5	265.2 1.4 0.5%	723 136 0.36	5.26 0.10 1.9%	57.6 0.2 0.3%	0.32 0.02 6.6%
Vortex basic	294.7 1.5 0.5%	795 152 0.49	5.26 0.10 2.0%	57.2 0.2 0.3%	0.31 0.02 7.0%
Vortex 1/4 pre 17	208.6 1.4 0.7%	485 116 0.42	4.19 0.08 2.0%	51.2 0.2 0.4%	0.29 0.02 6.5%
Vortex 1/4	203.6 1.3 0.6%	471 113 0.50	4.19 0.09 2.0%	51.1 0.2 0.4%	0.29 0.02 6.6%
Vortex 1/8 pre 17	111.7 1.1 1.0%	235 65 0.28	3.59 0.07 2.0%	47.5 0.2 0.5%	0.34 0.02 5.6%
Vortex 1/8	130.1 1.2 0.9%	269 76 0.35	3.62 0.08 2.1%	47.0 0.2 0.5%	0.32 0.02 5.9%
Mixer	281.0 1.4 0.5%	794 142 0.51	5.53 0.11 2.0%	59.1 0.2 0.3%	0.33 0.02 7.0%

Table 6.15: Regression rate comparison with axial (a) and vortex (v) data - ratio value

	Gox [kg/(m2*s]		Reg rate [mm/s]		a coef [mm/s]	
Axial	126%	100%	71%	100%	63%	100%
Vortex basic post 5	90%	71%	100%	141%	105%	167%
Vortex basic	100%	79%	100%	141%	100%	159%
Vortex 1/4 pre 17	71%	56%	80%	112%	94%	150%
Vortex 1/4	69%	55%	80%	112%	96%	152%
Vortex 1/8 pre 17	38%	30%	68%	96%	111%	175%
Vortex 1/8	44%	35%	69%	97%	104%	165%
Mixer	95%	76%	105%	148%	107%	170%
Case	v	a	v	a	v	a

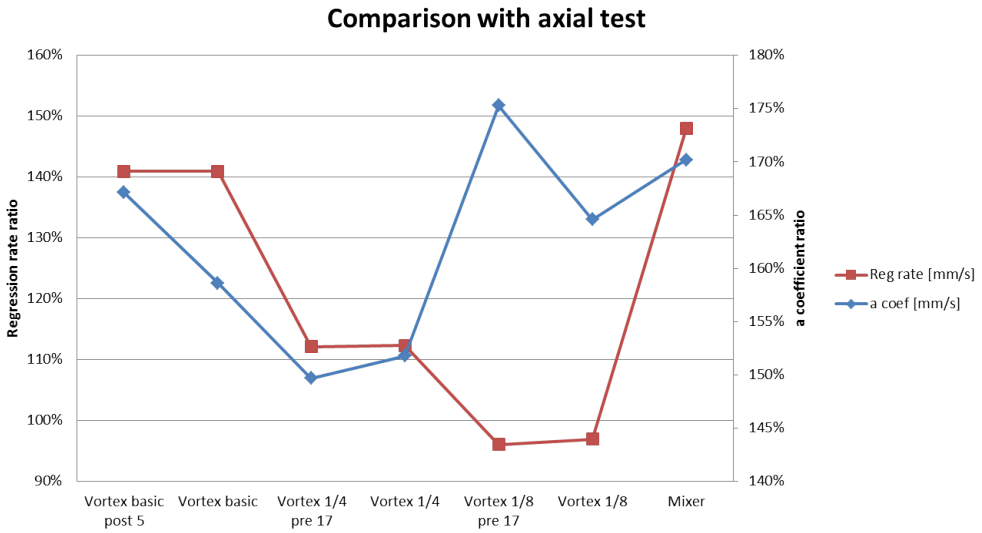

Figure 6.21: Regression rate test comparison - ratio value with axial data

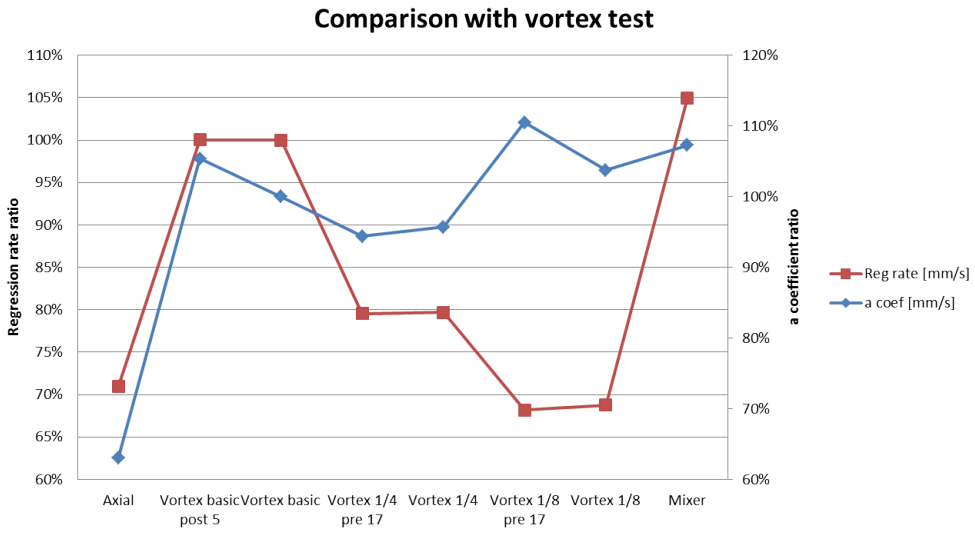

Figure 6.22: Regression rate test comparison - ratio value with vortex data

In fig.6.23 grain image are reported. The pictures shows the grain after a burn test with both axial and vortex injection (that is placed down in the image). It can be see the great difference in erosion between the two tests, in particular in the front section (near oxidizer injection). Clear marks are visible in the grain surface in fig.6.23(b) that are left by the swirling flow, and can be compared with CFD images in chap.4.1.

In fig.6.24 the same pictures were taken for the throttling configuration. Due to the lower mass flow the marks left on the grain surface are weaker than before, but it is clearer the differential regression rate that is higher in the front section than in the remaining of the grain burning area.

In fig.6.25 the combustion chamber configuration is changed, adding devices inside. Regression rate is 6% higher that with classical vortex. Marks on the surface are less visible due to the turbulence created by the device in the grain zone.

In conclusion, the most effective method to increase the regression rate is the change in injection (vortex respect to axial). Adding devices (pre-chamber, post-chamber, mixer) has a slight effect.

6.3.4 Combustion efficiency

Use of vortex injection has a high beneficial effect on combustion efficiency. In particular, experiments showed an increase in its value from 73% with axial injection up to 90% in vortex case. Numerical value are presented in tab.6.16.

Respect to regression rate, here we have a strong effect of combustion cham-

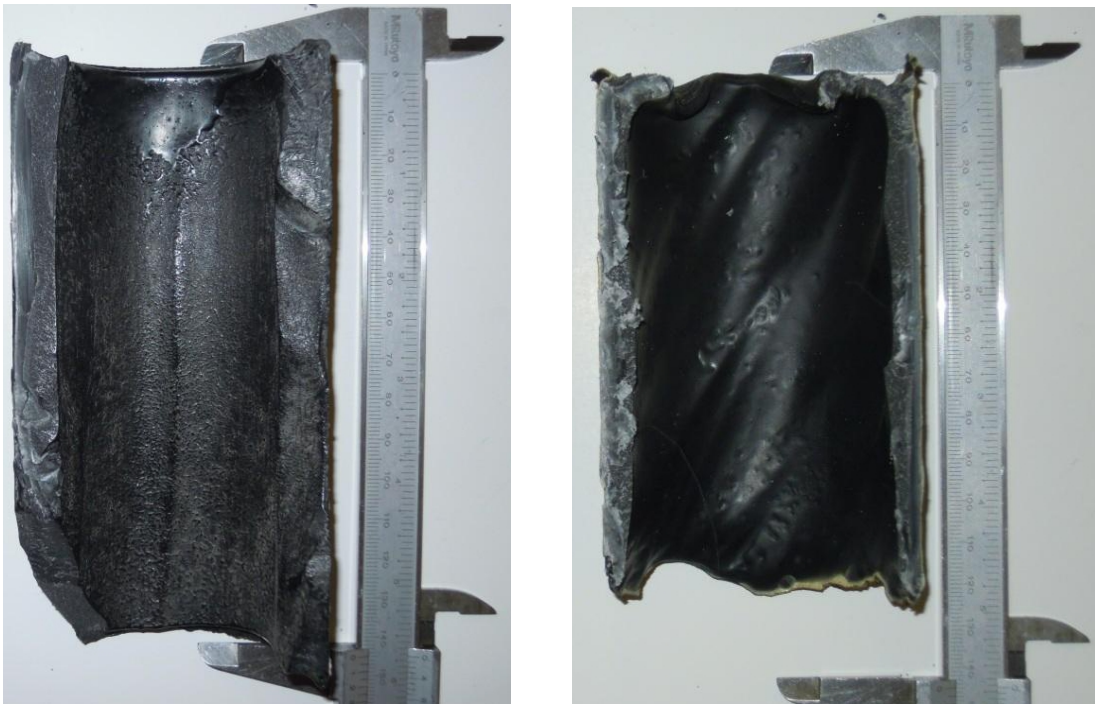

(a) Axial (b) Vortex

Figure 6.23: Grain after burn test: axial vs. vortex

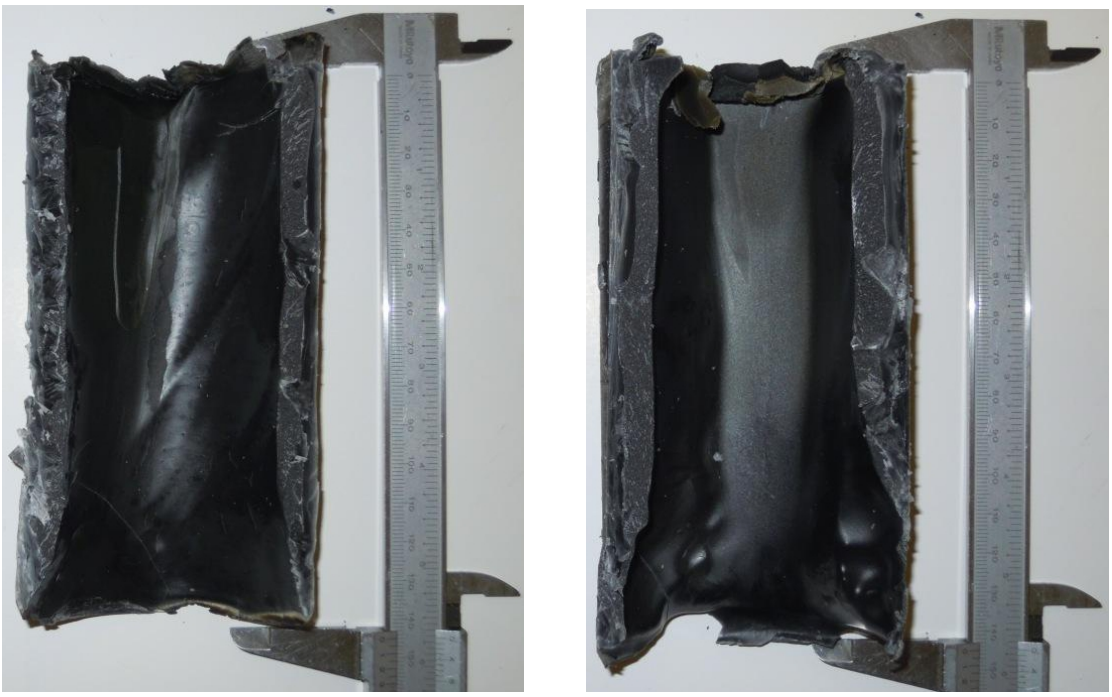

(a) 75% throttling (b) 50% throttling

Figure 6.24: Grain after burn test: throttling

Table 6.16: Burn test data - combustion efficiency

	c* [m/s]	Ideal c* [m/s]	c* efficiency	O/F
Axial	1169	1600	73.0%	6.4
	72		4.5%	0.12
	6.2%		6.2%	1.9%
Vortex basic post 5	1244	1400	88.9%	3.4
	51		3.7%	0.06
	4.1%		4.1%	1.9%
Vortex basic	1294	1426	90.7%	3.6
	82		5.7%	0.06
	6.3%		6.3%	1.7%
Vortex 1/4 pre 17	1177	1347	87.4%	3.0
	37		2.7%	0.08
	3.1%		3.1%	2.7%
Vortex 1/4	1126	1332	84.6%	2.9
	42		3.2%	0.08
	3.8%		3.8%	2.8%
Vortex 1/8 pre 17	1033	1219	84.7%	1.9
	85		7.0%	0.10
	8.2%		8.2%	5.4%
Vortex 1/8	1018	1244	81.8%	2.1
	40		3.2%	0.10
	4.0%		4.0%	4.9%
Mixer	1336	1390	96.1%	3.3
	46		3.3%	0.06
	3.5%		3.5%	1.7%

Figure 6.25: Grain after burn test: mixer

ber configuration. In particular, we have proved that increasing pre-combustion and post-combustion chambers enhance the combustion process, giving a higher c^* efficiency value (see fig.6.26), especially at low mi_{ox}. An explanation of the phenomenon is reported in chap.4.1. The best performances are given by the combined use of vortex injection and mixer-like devices (96% efficiency).

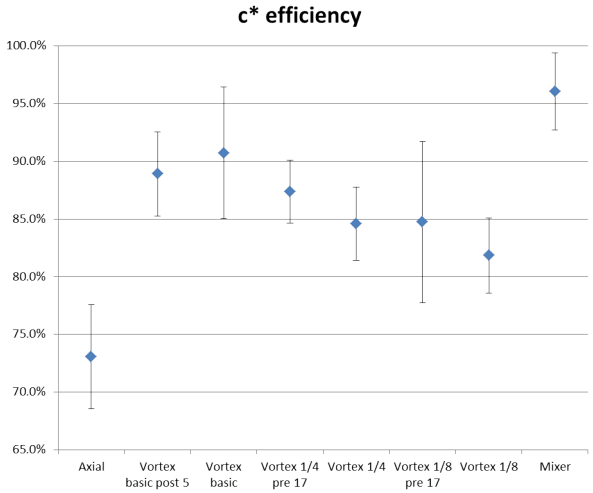

Figure 6.26: Experimental data: combustion efficiency

An important consideration is that given the same configuration (10mm of pre-chamber and 10mm of post-chamber), a reduction in the oxidizer mass flow

(throttling) produce a reduction in combustion efficiency (see fig.6.27). A quasi-linear relationship can be found using the same configuration and injection type between these values.

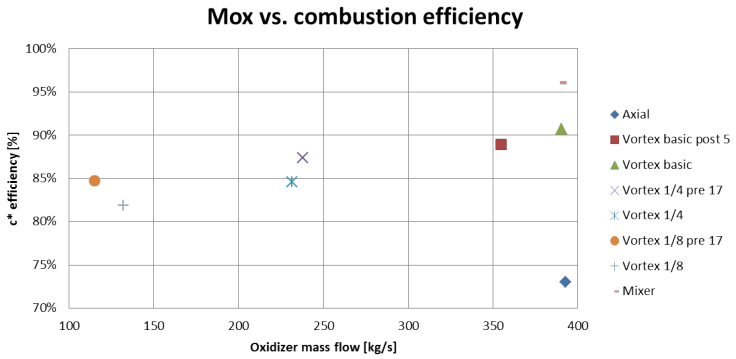

(a) All cases

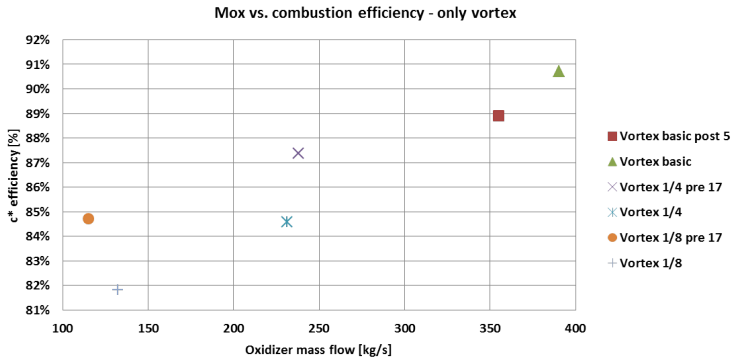

(b) Vortex cases

Figure 6.27: Experimental data: $\dot{m_{ox}}$ vs. combustion efficiency

Similar considerations can be found comparing O/F ratio and combustion efficiency (see fig.6.28): using vortex injection the O/F ratio is very low (between 1.9 and 3.6) respect to axial (6.4) because the burned propellant is higher and the oxidizer mass flow is the same. The ideal (max Isp) O/F is about 7. Despite this, using vortex injection we achieve the same a higher combustion efficiency.

Again, there is a linear relationship between O/F and c* efficiency (given the same configuration), that is in agreement with what previously said: as a rule of thumb, going away from ideal O/F means lower efficiency.

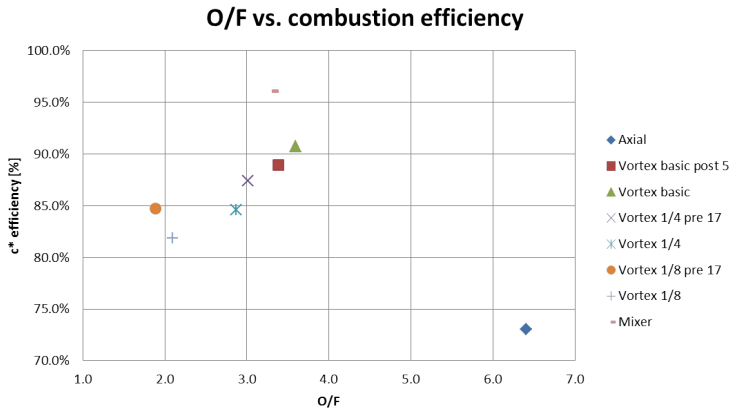

(a) All cases

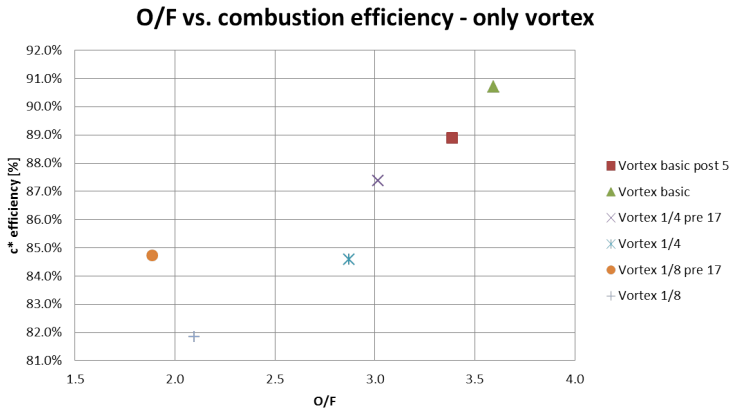

(b) Vortex cases

Figure 6.28: Experimental data: O/F ratio vs. combustion efficiency

Chapter 7

Conclusions

The aim of this thesis is to characterizer a throttled hybrid motor through a numerical and experimental investigation about vortex injection with pressurized nitrous oxide as oxidizer and paraffin as fuel. A comparison with classical axial shower-head injection has been investigated, together with different motor devices performance. The motor configuration has been adapted to fitful specific requirement for a formation flight mission, with a particular aim to collision avoidance.

This work has seen a first part with a numerical description of the fluid field inside the combustion chamber with an already validated CFD 3-D steady state software. Results showed that the swirling flow is highly influenced by the flame that accelerate the axial component of the velocity, straightening the fluid lines.

A 0-D analytical transient model has been used to achieve a preliminary design of the geometry, in terms of oxidizer mass flow, combustion chamber configuration (nozzle and paraffin fuel). This data has also been used in the test sensors choice, to evaluate the full scale value.

An analytical model has been developed using steady state Navier-Stokes in cylindrical coordinates: the solution showed a forced vortex behaviour of the velocity inside the combustion chamber. Moreover, a pressure gradient in the radial direction has been found, and verified comparing data with the CFD analysis. This information is useful in the selection of pressure pick-up point (post-chamber, where the gradient is negligible) and to analyze experimental data.

The 3D CFD model has also been involved also in the characterization of the motor with different configurations: a) different oxidizer mass flow to simulate the throttling, b) different grain diameter to evaluate the burn test at various time steps and c) change in combustion chamber configuration with pre/post-combustion chambers or mixer-like devices.

Results had a good agreement with experimental data, validating once more the software used. In particular, it has been observed that changing the motor configuration has a great impact on the performance, and an enhancement on pressure chamber and combustion efficiency can be achieved with a mixer. At different burning time, the important thing is that the swirling fluid field maintain the same shape also with sudden change in the diameter given by the burned grain. Changing the mass flow, once again, maintain the vortex behaviour reducing the pressure due to the lower mass flow.

Throttling design has passed through a first selection of the method to obtain it: the final has been choice a needle valve. A characterization has been performed, first using water and then with the actual oxidizer. The throttling ratio chosen is 75% and 50% of the mass flow.

Experimental analysis has been performed with both axial and vortex injection. The investigation was focused on chamber pressure oscillation, regression rate and combustion efficiency. A test bench has been designed in terms of sensors to be used for measurements of thrust, pressure, temperature and oxidizer mass flow. The campaign started with cold tests, measuring the same mass flow (350g/s) and thus injection discharge coefficient for both injectors.

Burn test showed an increase (from axial to vortex injection) in regression rate from 3.7mm/s up to 5.3mm/s (+41%), with an increment in a coefficient in the regression rate formula from 0.19mm/s up to 0.31mm/s (+67%). Chamber pressure oscillations where reduced from 7.5% of mean value in axial case down to 3.8%. Combustion efficiency has been increased from 73% up to 91%.

Second part of burn test regarded the throttling of the motor, with vortex injection and in a configuration with 1cm of pre-chamber and 1cm of post-chamber. The choice has been made in order to avoid ignition problems and different regime during burn. Throttling has seen a reduction in combustion efficiency down to 85% for the 75% throttle and 82% for the 50% throttling. Pressure oscillation has been maintained at the same level. Regression rate has been evaluated through the a coefficient, with values of 0.29mm/s for 75% throttling and 0.34mm/s for 50%.

Last part regarded the combustion chamber configuration. It has been observed that a longer pre-combustion chamber (17mm against 10mm) lower the pressure oscillation down to 2%. Use of mixer, furthermore, drops the value to 1.2%. Combustion efficiency is increased of 6% using mixer-like devices, and 3% with longer pre-chamber. Regression rate is enhanced by the use of mixer increasing the a coefficient value of 6%.

Chapter 8

Conclusioni

Questa tesi ha come obiettivo la caratterizzazione sperimentale e numerica di un propulsore ibrido a spinta variabile per formation flight. La scelta di ossidante e combustibile é ricaduta su N_2O pressurizzato e paraffina. La discussione é divisa in 3 parti: una prima in cui si compara l'iniezione vortex e quella assiale, una seconda in cui si analizza il fenomeno del throttling ed una terza in cui si affrontano differenti configurazioni interne della camera di combustione. Il motore é stato ottimizzato per l'impiego per collision avoidance.

Il lavoro ha visto una prima parte in cui la fluidodinamica interna viene analizzata con un codice CFD 3D stazionario, giá validato con altri test case. Il flusso vortex é stato analizzato, ed il risultato é che il parametro che maggiormente influenza il campo di moto é l'incremento di temperatura dato dalla fiamma che accelera la componente assiale della velocitá raddrizzando quindi l'angolo di swirl.

Un modello 0-D transiente analitico é stato sviluppato. Lo scopo é di avere un tool per un dimensionamento preliminare del motore, in particolare in termini di dimensioni della camera, del grano, dell'ugello e di portata di massa di ossidante. Questo modella ha inoltre aiutato nella scelta della strumentazione fornendo informazioni per quanto riguarda il fondo-scala degli strumenti da analizzare.

Un modello analitico é stato sviluppato utilizzando le equazioni di Navier-Stokes in coordinate cilindriche: la soluzione ha mostrato un campo di moto di tipo vortice forzato; oltre a questo, é stato calcolato un gradiente di pressione in senso radiale. Questa analisi é stata confrontata con il modello 3D precedentemente sviluppato. Questa analisi é stata di fondamentale importanza nel posizionamento dei sensori di pressione. In particolare, si é visto che in postcamera questo effetto di gradiente é trascurabile.

Il modello 3D fluidodinamico é stato impiegato anche nella caratterizzazione

del motore ibrido, studiando le diverse configurazioni in seguito testate: a) diverse portate di ossidante per studiare la variazione di spinta b) diametri di porta del grano differenti, per valutare le performance di una stessa configurazione in piú istanti del test e c) varie configurazioni della camera di combustione, valutando l'effetto di pre/post-camere e componenti tipo mixer.

I risultati sono stati concordanti con quelli sperimentali per quanto riguarda i trend, e questo ha contribuito ad ottenere una ulteriore validazione del codice CFD. In particolare, é stato osservato come la configurazione del motore (utilizzo di device nella camera di combustione) ha una grande influenza nelle performance, specialmente con l'utilizzo di mixer che aumentano l'efficienza di combustione. L'analisi di differenti time step ha fornito dati riguardanti l'andamento del campo di moto fluido, confermando che nonostante ci siano bruschi cambi di geometria (dati dal grano che si consuma) l'andamento swirling permane. Questo risultato é stato osservato anche simulando la variazione di portata, con il risultato di misurare una pressione in camera minore data dal minor afflusso di massa in camera.

Il design della componentistica di throttling ha visto una parte iniziale di scelta del metodo di riduzione della portata di ossidante, portando alla selezione di una valvola a spillo. Questa é stata caratterizzata tramite test con acqua e N_2O. Il rapporto di throttling scelto é stato di 75% e 50%.

L'ultima parte ha visto una estesa campagna di test sperimentali, in cui le precedenti configurazioni sono state analizzate. Lo scopo dell'indagine é stato lo studio del regression rate, dell'efficienza di combustione e delle oscillazioni di pressione in camera. Il design del motore é stato corredato da un banco da test in cui sono stati selezionati i sensori in base all'accuratezza richiesta per misure di pressione, temperatura, spinta e portata di massa di ossidante. La campagna sperimentale ha visto una prima parte in cui sono state effettuate delle scariche a freddo per valutare la portata di massa ed il coefficiente di scarica delle due tipologie di iniezione: il risultato é stato il medesimo per entrambi, con una portata di 350g/s.

I test a fuoco hanno mostrato un aumento (da iniezione assiale a vortex) nel regression rate da 3.7mm/s a 5.3mm/s (+41%) con un incremento del coefficiente a della formula del regression rate da 0.19mm/s a 0.31mm/s (+67%). Le oscillazioni di pressione in camera sono state ridotte dal 7.5% del valore medio nel caso assiale fino al 3.8% del caso vortex. L'efficienza di combustione é stata portata dal 73% al 91%.

Nella seconda parte dei test é stato analizzato il throttling del motore ibrido, utilizzando una configurazione con iniezione vortex e pre-camera e post-camera da

10mm. La scelta é stata effettuata per evitare problemi all'accensione e differenti regimi di pressione durante il burn. La riduzione della portata di massa ha visto una conseguente riduzione di efficienza di combustione fino a valori del 85% nel caso di throttling al 75% e del 82% nel caso di throttling al 50%. Le oscillazioni di pressione sono rimaste invariate. Il coefficiente di regression rate é stato misurato: con portata al 75% ha un valore di 0.29mm/s, mentre con portata al 50% ha un valore di 0.34mm/s.

L'ultima parte ha riguardato la configurazione della camera di combustione. Si é misurato un decremento delle oscillazioni di pressione fino al 2% con una precamera piú lunga (da 10mm a 17mm). Questo valore scende ancora fino al 1.2% se viene impiegato un mixer. L'efficienza di combustione viene aumentata del 6% con dispositivi tipo mixer, mentre l'incremento é del 3% con la pre-camera piú lunga. Il regression rate viene aumentato del 6% con l'impiego del mixer.

Bibliography

[1] *Evaluation of Measurement Data - Guide to the Expression of Uncertainty in Measurement (GUM).* International Organization for Standardization, 1995.

[2] http://webbook.nist.gov/chemistry/, Nov 2011.

[3] http://www.spg-corp.com/nitrous-oxide-safety.html, Jan 2012.

[4] *McGraw-Hill Dictionary of Scientific & Technical Terms.* The McGraw-Hill Companies, Inc., Jan. 2003.

[5] Andrew J. Tatem A, Scott J. Goetz B, and Simon I. Hay A. Terra and aqua: new data for epidemiology and public health abstract, 2003.

[6] F. Barato, N. Bellomo, M. Faenza, M. Lazzarin, A. Bettella, and D. Pavarin. A numerical model to analyze the transient behavior and instabilities on hybrid rocket motors. In *47th AIAA/ASME/SAE/ASEE Joint Propulsion Conference and Exhibit, 31 July – 3 August 2011, San Diego, California*, 2011.

[7] N. Bellomo, F. Barato, M. Faenza, M. Lazzarin, A. Bettella, and D. Pavarin. Numerical and experimental investigation on vortex injection in hybrid rocket motors. In *47th AIAA/ASME/SAE/ASEE Joint Propulsion Conference and Exhibit, 31 July – 3 August 2011, San Diego, California*, 2011.

[8] N. Bellomo, M. Lazzarin, F. Barato, and M. Grosse. Numerical investigation of the effect of a diaphragm on the performance of a hybrid rocket motor. In *46th AIAA/ASME/SAE/ASEE Joint Propulsion Conference, 25 - 28 Jul 2010, Nashville, Tennessee, USA*, 2010.

[9] J.J.C.M. Bik, P.N.A.M. Visser, and O. Jennrich. Lisa satellite formation control. *Advances in Space Research*, 40(1):25 – 34, 2007.

[10] M.J. Chiaverini and K.K. Kuo. *Fundamentals of hybrid rocket combustion and propulsion*. Progress in astronautics and aeronautics. American Institute of Aeronautics and Astronautics, 2007.

[11] R.H. Dieck. *Measurement uncertainty: methods and applications*. ISA, 2006.

[12] E.O. Doebelin. *Measurement systems: application and design*. International Student Editions. McGraw-Hill, 1975.

[13] Gordon A. Dressler and J. Martin Bauer. Trw pintle engine heritage and performance characteristics. *AIAA - American Institute of Aeronautics and Astronautics*, 2000.

[14] William R. Jr. Hammock, Eldon C. Currie, and Arlie E. Fisher. Apollo experience report - descent propulsiono system. Technical report, NASA, 1973.

[15] R. Humble, G.N. Henry, W.J. Larson, United States. Dept. of Defense, United States. National Aeronautics, and Space Administration. *Space propulsion analysis and design*. Space technology series. McGraw-Hill, 1995.

[16] A. Karabeyoglu, G. Zillic, B. J. Cantwell, S. DeZilwa, and P. Castellucci. Scale-up tests of high regression rate paraffin-based hybrid rocket fuels. *Journal of Propulsion and Power*, 20:1037–1045, 2004.

[17] M. A. Karabeyoglu, B. J. Cantwell, and D. Altman. Development and testing of paraffin-based hybrid rocket fuels. In *37th AIAA/ASME/SAE/ASEE Joint Propulsion Conference and Exhibit, 8-11 July, Salt Lake City, Utah*, 2001.

[18] Vivek K Khanna. *A Study of the Dynamics of Laminar and Turbulent Fully and Partially Premixed Flames*. PhD thesis, Virginia Polytechnic Institute and State University, 2001.

[19] K. Kitagawa, T. Mitsutani, T. Ro, and S. Yuasa. Effects of swirling liquid oxygen flow on combustion of a hybrid rocket engine. In *40th AIAA/ASME/SAE/ASEE Joint Propulsion Conference and Exhibit, 11-14 July 2004, Fort Lauderdale, Florida*, 2004.

[20] S. J. Kline and F. A. McClintock. Describing uncertainties in single-sample experiments. *Mech. Eng.*, 1953.

[21] William H Knuth, Martin J Chiaverini, Daniel J Gramer, and J Arthur Sauer. Solid-fuel regression rate behavior of vortex hybrid rocket engines. *Journal of Propulsion and Power*, 18(3):600–609, 2002.

[22] Wang Sang Koon, Jerrold E. Marsden, and Richard M. Murray. J2 dynamics and formation flight. In *In Proceedings of AIAA Guidance, Navigation, and Control Conference*, 2001.

[23] G. Krieger, A. Moreira, H. Fiedler, I. Hajnsek, M. Werner, M. Younis, and M. Zink. Tandem-x: A satellite formation for high-resolution sar interferometry. *Geoscience and Remote Sensing, IEEE Transactions on*, 45(11):3317 –3341, nov. 2007.

[24] M. Lazzarin, M. Faenza, F. Barato, N. Bellomo, A. Bettella, D. Pavarin, and M. Grosse. Cfd simulation of a hybrid rocket motor with liquid injection. In *47th AIAA/ASME/SAE/ASEE Joint Propulsion Conference and Exhibit, 31 July – 3 August 2011, San Diego, California*, 2011.

[25] Hank Pernicka, Brian A. Carlson, and S. N. Balakrishnan. Spacecraft formation flight about libration points using impulsive maneuvering. In *AIAA Journal of Guidance, Control, and Dynamics, Vol. 29, No. 5, pp. 1122-1130, 2006*, 2006.

[26] J. M. Pucci. The effects of swirl injector design on hybrid flame-holding combustion instability. *AIAA Paper 2002-3578, July 2002*, 2002.

[27] Daniel P. Scharf, Fred Y. Hadaegh, and Scott R. Ploen. A survey of spacecraft formation flying guidance and control (part ii): Control. In *Proceedings of the American Control Conference*, pages 2976–2985, 2004.

[28] G.P. Sutton and O. Biblarz. *Rocket Propulsion Elements*. John Wiley & Sons, 2010.

[29] A. Valmorbida, G. Baù, E. Lorenzini, and G. Sechi. Model predictive control strategies for spacecraft formation flying applications. In *3rd CEAS Air and Space Conference - 21st AIDAA Congress, 24 - 28 October 2011, Venice, Italy*, 2011.

[30] A. Valmorbida, E. Lorenzini, and G. Sechi. Guidance and control strategies for the collision-avoidance mode of a satellite pair flying in formation. In *3rd*

CEAS Air and Space Conference - 21st AIDAA Congress, 24 - 28 October 2011, Venice, Italy, 2011.

[31] D. Van Pelt, J. Hopkins, M. Skinner, A. Buchanan, R. Gulman, H. Chan, M. A. Karabeyoglu, and B. Cantwell. Overview of a 4-inch od paraffin-based hybrid sounding rocket program. In *40th AIAA/ASME/SAE/ASEE Joint Propulsion Conference and Exhibit, 11-14 July 2004, Fort Lauderdalee, Florida*, 2004.

[32] W. Waidmann. Thrust modulation in hybrid rocket engines. *Journal of Propulsion*, 4, 1988.

[33] R. Wilkinson, K. Hart, R. Day, and I. Coxhill. Proof-pf.concept testing of a sustained vortex-flow configuration for hybrid rocket motors. In *46th AIAA/ASME/SAE/ASEE Joint Propulsion Conference and Exhibit, 25-28 July 2010, Nashville, TN*, 2010.

[34] S. Yuasa, K. Yamamoto, H. Hachiya, K. Kitagawa, and Y. Oowada. Development of a small sounding hybrid rocket with a swirling-oxidizer-type engine. *37th AIAA / ASME / SAE / ASEE Joint Propulsion Conference & Exhibit 8-11 July 2001 Salt Lake City , Utah*, (July), 2001.

Acknowledgments

Voglio ringraziare per avermi consentito di sviluppare questa tesi tutto lo staff del CISAS, ed in particolare i prof. Giampiero Naletto e Cesare Barbieri per la direzione del dottorato.

Un ringraziamento particolare va ai miei supervisori, senza i quali non sarei arrivato dove sono ora: Daniele Pavarin e Mariolino De Cecco.

Per il loro supporto, fisico e morale, un ringraziamento va a tutti i miei colleghi, sperimentali e non: Albe, Fede, Enrico, Cisque, Frasso, Martina e Marta della parte ibrida, e Manente, Fabris, Fabio, Melazzi, Curreli e Rondini della parte plasmi, e non meno importante Devis per Sponge.

Un ringraziamento anche a tutte le segretarie del CISAS, che ci hanno permesso di ridurre al minimo la produzione di scartoffie e la burocrazia universitaria.

Mi preme ricordare, visto che con questa tesi concludo la mia carriera universitaria, tutti quei professori che per me sono stati culturalmente importanti, insegnandomi un mestiere che non mi stancheró mai di fare: Mirco Zaccariotto, Giovanni Meneghetti, Daniele Pavarin, Marco Manente e Luca Baglivo.

Un saluto va anche ai miei ex-colleghi ed amici patavini che mi hanno fatto dimenticare le fatiche della giornata tra spritz e montagna: Ale e Katrina, Nicole e Cate, Rai, Seba, Caon, e Denis.

Oltre a loro, mi preme ricordare gli amici d'infanzia: Nando, Nappi, Muzze, Luca, Berli, Mauro, Giovanni, Elena e Stefania.

Per tutto il loro sostegno ed appoggio, ci tengo a ringraziare tutta la mia famiglia, ed in particolare mia mamma Lucia.

Last but not least, un caloroso ringraziamento va alla mia ragazza Cecilia, che mi ha sopportato e supportato in questi mesi di tesi (e non solo).